

The Pennsylvania State University

The Graduate School

College of Engineering

**DESIGN, MODELING, AND SIMULATION OF BATTERY PACK SUSPENSIONS  
FOR OFF-ROAD ELECTRIC VEHICLES**

A Thesis in

Mechanical Engineering

by

Daniel L. Aglione

© 2014 Daniel L. Aglione

Submitted in Partial Fulfillment  
of the Requirements  
for the Degree of

Master of Science

May 2014

The thesis of Daniel L. Aglione was reviewed and approved\* by the following:

Christopher D. Rahn  
Professor of Mechanical Engineering  
Thesis Advisor

John S. Lamancusa  
Professor of Mechanical Engineering

Karen A. Thole  
Professor of Mechanical Engineering  
Head of the Department of Mechanical and Nuclear Engineering

\*Signatures are on file in the Graduate School

## **ABSTRACT**

Battery packs on commercial off-road battery electric vehicles (BEVs) are exposed to harsh environments with vibration and shock loading that can lead to battery damage and premature failure. Underground mining, for example, uses BEVs to mitigate both the ventilation costs and safety concerns associated with emissions from internal combustion engines. A BEV must have a large battery pack to allow continuous operation for an entire shift. Ensuring long life of the expensive pack often requires a suspension system to isolate damaging resonant frequencies and attenuate transient shock accelerations.

In this thesis, suspensions comprising wire rope isolators and silicone safety bump stops are designed, modeled, and simulated for an example underground mining vehicle. A six degree-of-freedom dynamic model is developed that predicts battery pack responses given a variety of base acceleration inputs from the BEV. Simulation results indicate that there are many bump stop, isolator, and attachment point designs that successfully isolate battery cell resonances at 35 Hz. Two design parameters, bump stop effective thickness and maximum isolator travel, significantly affect shock attenuation. Bump stop designs can be tuned to optimize shock response without affecting vibration performance.

# TABLE OF CONTENTS

List of Figures .....	vii
List of Tables .....	xiii
Acknowledgements.....	xiv
Chapter 1 Introduction .....	1
1.1 BEVS for Off-Road Applications.....	1
1.2 Effects of Shock and Vibration on Battery Life .....	3
1.3 Review of Shock and Vibration Isolating Suspensions .....	4
1.3.1 Passive Suspension .....	5
1.3.2 Semi-Active Suspension .....	11
1.3.3 Active Suspension.....	13
1.4 Research Objectives.....	14
1.5 Thesis Outline.....	14
Chapter 2 Background and Requirements .....	16
2.1 Battery Installation.....	17
2.2 Design Requirements.....	18
Chapter 3 Suspension System Design.....	19
3.1 Wire Rope Isolators .....	20
3.1.1 Background .....	20
3.1.2 Performance Characteristics.....	22
3.2 Silicone Sheets.....	24
3.2.1 Background .....	24
3.2.2 Performance Characteristics.....	26
3.3 Assembly Configurations .....	28
3.3.1 Stacked Configuration.....	29
3.3.2 Single Battery Configuration .....	29
3.4 Bump Stops.....	30
Chapter 4 Model Formulation.....	32
4.1 Modeling of Battery.....	32
4.2 Modeling of Tray .....	34
4.3 Modeling of Wire Rope Isolators .....	35
4.3.1 Spring Properties.....	36
4.3.2 Damping Properties.....	38

4.4	Modeling of Bump Stops.....	40
4.4.1	Spring Properties.....	41
4.4.2	Damping Properties.....	41
4.4.3	Stacking.....	43
4.5	Static Equilibrium.....	45
4.6	Mathematical Structure.....	47
4.6.1	Inputs.....	48
4.6.2	States.....	49
4.6.3	Outputs.....	51
Chapter 5 Equations of Motion.....		52
5.1	Battery Surface Discretization.....	52
5.2	Battery Surface Displacements.....	57
5.3	Battery Surface Velocities.....	60
5.4	Wire Rope Isolator Forces.....	62
5.5	Bump Stop Forces.....	67
5.6	Equations of Motion.....	70
5.7	Output Battery Accelerations.....	72
Chapter 6 Base Acceleration Inputs.....		73
6.1	Accelerometer Data Collection.....	74
6.2	Vibration Input.....	75
6.3	Typical Shock Input.....	77
6.4	Severe Shock Input.....	78
Chapter 7 Results and Discussion.....		80
7.1	Simulation Procedure.....	80
7.2	Analysis Methods.....	83
7.3	Stacked Battery Configuration.....	84
7.3.1	Isolator Design Generation.....	84
7.3.2	Simulation Results.....	86
7.3.3	Bump Stop Design.....	98
7.4	Single Battery Configuration.....	101
7.4.1	Isolator Design Generation.....	101
7.4.2	Simulation Results.....	102
7.4.3	Bump Stop Design.....	112
7.5	Design Tradeoffs.....	113
7.5.1	Bump Stop Effective Thickness.....	114
7.5.2	Supplementary Damping.....	117
7.5.3	Expanded Clearances.....	120

7.6 Discussion.....	122
Chapter 8 Conclusion.....	126
References.....	128
Appendix A – Model Validation.....	131
A.1 SDOF Analytical Validation.....	131
A.2 SolidWorks Motion Study.....	135
Appendix B – MATLAB File Structure .....	139
Appendix C – Descriptions of MATLAB Files.....	143
C.1 Simulate_6DOF.....	143
C.2 rk4.....	144
C.3 Tray Inputs .....	144
C.3.1 TrayInput_AccData .....	145
C.3.2 TrayInput_None .....	145
C.3.3 TrayInput_Pulse .....	145
C.3.4 TrayInput_Sine .....	145
C.4 Dynamics .....	146
C.5 Bump Stop .....	147
C.5.1 BumpStop_Silicone .....	148
C.5.2 BumpStop_Custom .....	148
C.6 Analysis Tools .....	149
C.6.1 Collision .....	149
C.6.2 FFTEval .....	150
C.6.3 PSDEval .....	151
C.6.4 SRSEval .....	151
C.6.5 PlotResults .....	151
C.7 Wire Rope Isolators .....	152
C.8 BISCO Silicones .....	152
Appendix D – User Instructions .....	153
D.1 Prepare Simulate_6DOF .....	153
D.2 Prepare the Dynamics File .....	157
D.3 Prepare the Bump Stop File .....	159
D.3.1 Prepare “BumpStop_Silicone”.....	160
D.3.2 Prepare “BumpStop_Custom” .....	162
D.4 Run, Analyze, Save.....	165

## LIST OF FIGURES

- Figure 1-1. Battery electric mining vehicles [4, 5]
- Figure 1-2. SAE vibration test specification for electric vehicle batteries [7]
- Figure 1-3. Conventional passive isolator [10]
- Figure 1-4. MacPherson strut [10]
- Figure 1-5. Air springs used in fifth wheel tractor hitch [14]
- Figure 1-6. Pneumatic isolator vehicle suspension systems [15, 16]
- Figure 1-7. SRS maximum acceleration results from rudimentary drop test [18]
- Figure 1-8. Helical wire rope isolator (left) and seismic test stand (right) [31, 21]
- Figure 1-9. Skyhook damping diagram [9]
- Figure 1-10. Schematic diagram of MR semi-active damper [23]
- Figure 1-11. Precision sensor suspension system using semi-active MR isolators [24]
- Figure 2-1. GE Fairchild underground mining scoop [27]
- Figure 2-2. Carrier tray suspended by lifting arms behind the rear tires
- Figure 2-3. Exploded view of tray containing Durathon Battery modules
- Figure 2-4. Side section view of battery-tray system
- Figure 3-1. Suspension system conceptual design
- Figure 3-2. Helical-style wire rope isolator [31]
- Figure 3-3. Deflection modes of wire rope isolator [32]
- Figure 3-4. Geometric properties of M6 isolators sold by IDC [32]
- Figure 3-5. Compression load-deflection curve for M6 isolators [32]
- Figure 3-6. Example damping behavior of an Enidine wire rope isolator
- Figure 3-7. Closed-cell silicone foam [35]
- Figure 3-8. Force-deflection polynomial curve fits for BISCO cellular silicone foams

Figure 3-9. Force-deflection curves for BISCO solid silicone pads [33]

Figure 3-10. Side view of stacked battery configuration

Figure 3-11. Side view of single battery configuration

Figure 3-12. Bump stops constrain the maximum travel of the battery and isolators

Figure 3-13. Bump stops engaging battery in compression (left) and roll (right)

Figure 4-1. Rigid body battery model

Figure 4-2. Location of tray coordinate system at static equilibrium

Figure 4-3. Three-axis spring-damper model of a wire rope isolator

Figure 4-4. Vertical (a) and lateral (b) spring force-deflection curves

Figure 4-5. Piecewise damping ratio approximation

Figure 4-6. Force-velocity curves using the nine possible damping coefficients

Figure 4-7. Spring-damper model of a silicone sheet's compression

Figure 4-8.  $k_{lin}$  estimation for HT-820 silicone foam

Figure 4-9. Stacking of silicone sheets

Figure 4-10. Displacement of silicone sheets within stack

Figure 4-11. Model representation of system packaging

Figure 4-12. System model diagram of stacked battery configuration

Figure 4-13. System model diagram of single battery configuration

Figure 4-14. Translational accelerations of tray coordinate system

Figure 4-15. Six state variables defining relative battery position

Figure 4-16. Output accelerations of the battery

Figure 5-1. Discretization of battery faces with attachment point matrices

Figure 5-2. Left face (a) and right face (b) attachment points

Figure 5-3. Front face (a) and back face (b) attachment points

Figure 5-4. Top face (a) and bottom face (b) attachment points

Figure 5-5. Point  $i$  deflections in tray coordinates

Figure 5-6. Deflection axes of wire rope isolator

Figure 5-7. Alignment of wire rope isolators installed underneath battery stack

Figure 5-8. Alignment of wire rope isolators installed on front face of single battery

Figure 5-9. Top view of system free body diagram

Figure 5-10. Front (a) and back (b) views of system free body diagram

Figure 5-11. Alignment between bump stop discretized areas and battery attachment points

Figure 5-12. Right side view of bump stop compressive forces

Figure 5-13. Front view of bump stop compressive forces

Figure 6-1. Triaxial accelerometer attachment

Figure 6-2. Accelerations of tray coordinate axes corresponding to vibration inputs

Figure 6-3. Fast Fourier transform of vibration inputs

Figure 6-4. Typical shock input profile

Figure 6-5. Severe shock input profile

Figure 7-1. Bump stop optimization flow diagram

Figure 7-2. Maximum travel capabilities of battery stack isolator designs

Figure 7-3. Isolator displacements without using bump stops (Design A)

Figure 7-4. Battery stack collision with side wall of tray

Figure 7-5. Isolator displacements with tuned bump stops (Design A)

Figure 7-6. SRS using severe shock input (Design A)

Figure 7-7. SRS using typical shock input (Design A)

Figure 7-8. Battery stack CG accelerations using typical shock input (Design A)

Figure 7-9. Relative displacements of battery stack using typical shock input (Design A)

Figure 7-10. Power spectral density of vibration response (Design A)

Figure 7-11. SRS of stacked battery designs using severe shock input

Figure 7-12. Maximum acceleration magnitudes of battery stack using severe shock input

Figure 7-13. Maximum acceleration magnitudes of battery stack using typical shock input

Figure 7-14. SRS of stacked battery designs using typical shock input

Figure 7-15. PSD of battery stack vibration response in *X* direction

Figure 7-16. PSD of battery stack vibration response in *Y* direction

Figure 7-17. PSD of battery stack vibration response in *Z* direction

Figure 7-18. Bump stop design for Design E

Figure 7-19. Side view of bump stop design for isolator Design E

Figure 7-20. Front view of bump stop design for isolator Design E

Figure 7-21. Maximum travel capabilities of single battery isolator designs

Figure 7-22. Isolator displacements without using bump stops (Design F)

Figure 7-23. Isolator displacements with tuned bump stops (Design F)

Figure 7-24. Battery CG accelerations using severe shock input (Design F)

Figure 7-25. Relative displacements of battery using severe shock input (Design F)

Figure 7-26. SRS of single battery isolator designs using severe shock input

Figure 7-27. Maximum acceleration magnitudes of single battery using severe shock input

Figure 7-28. Maximum acceleration magnitudes of single battery using typical shock input

Figure 7-29. SRS of single battery isolator designs using typical shock input

Figure 7-30. PSD of single battery vibration response in *X* direction

Figure 7-31. PSD of single battery vibration response in *Y* direction

Figure 7-32. PSD of single battery vibration response in *Z* direction

Figure 7-33. Time response of battery and isolators using vibration input

Figure 7-34. Bump stop design for Design F

Figure 7-35. Variable bump stop effective thickness designs

Figure 7-36. SRS using severe shock input for three bump stop designs

Figure 7-37. SRS using typical shock input for same three bump stop designs

Figure 7-38. Example of a fluidic damper provided by Dorman Long Technology [41]

Figure 7-39. SRS of system response with additional damping

Figure 7-40. Vibration response with additional damping

Figure 7-41. SRS of expanded clearance design using typical shock input

Figure 7-42. SRS of expanded clearance design using severe shock input

Figure 7-43. Vibratory natural frequencies of single battery isolator designs

Figure A-1. Free responses using SDOF analytical equations and simplified 6DOF model

Figure A-2. Battery-tray system modeled in SolidWorks Motion Study

Figure A-3. Half sine acceleration pulse for SolidWorks Motion Study validation

Figure A-4. Pulse response in *Y* direction using SolidWorks and linear 6DOF MATLAB models

Figure A-5. Pulse response in *Z* direction using SolidWorks and linear 6DOF MATLAB models

Figure B-1. MATLAB file structure

Figure B-2. Flow diagram of MATLAB input/output variables

Figure C-1. Battery corner labeling

Figure D-1. Select Input, Dynamics, and Bump Stop functions

Figure D-2. Specify initial conditions and clearances

Figure D-3. Specify which analysis tools are automatically executed after simulation

Figure D-4. Isolator selection and attachment location

Figure D-5. Battery mass and dimensions

Figure D-6. Isolator deflections assigned to *DispIso*, which is used in “PlotResults”

Figure D-7. Silicone bump stop material and attachment positions

Figure D-8. Bump stop individual attachment area

Figure D-9. Number of silicone sheets stacked in series

Figure D-10. Engage distances

Figure D-11. Custom stiffness and damping properties

Figure D-12. Custom bump stop force and moment calculation

Figure D-13. Execute "Simulate\_6DOF"

Figure D-14. Waitbar

Figure D-15. Contents of the structure *Results*

Figure D-16. Contents of *SimDetails*

Figure D-17. Contents of *IsolatorInfo*

Figure D-18. Contents of *BumpStopInfo*

## LIST OF TABLES

Table 3-1. BISCO cellular silicones compression modulus [33]

Table 4-1. Battery parameters

Table 4-2. Linear spring constants of wire rope isolator

Table 5-1. Point  $i$  position in tray and battery coordinate systems

Table 6-1. Categorization of recorded shock events

Table 7-1. Statically-feasible isolator designs for battery stack configuration

Table 7-2. Optimized bump stop design for Design E

Table 7-3. Statically-feasible isolator designs for single battery configuration

Table 7-4. Optimized bump stop design for Design F

Table A-1. Free response system properties for analytical comparison

Table B-1. List of all MATLAB files

## ACKNOWLEDGEMENTS

I would like to express my sincerest thanks to all of the people that have supported me throughout my time as a graduate student at Penn State. First and foremost, I would like to thank my thesis advisor, Dr. Christopher Rahn, for his tremendous guidance over the past year. Dr. Rahn's relaxed nature and work style allowed me to take the reins of my research project by exploring my own approaches and solutions, while still being welcome to call upon his expertise at any moment. I have learned so much from him, not only academically, but more importantly through his demeanor and professionalism when working with others in a team environment. I truly could not have hoped for a better student-advisor relationship.

Secondly, I would like to thank my co-advisor, Dr. Joel Anstrom, and the GE Propulsion team for their invaluable assistance throughout this project. Dr. Anstrom was able to provide much insight from his experiences in industry and always offered design perspectives from a practical standpoint. I am appreciative of the encouragement and cooperation that I received from the GE team, as they were very attentive and willing to provide me with any data or details that I requested for my analyses. GE created such a positive working environment; it was easy being enthusiastic about the project because enthusiasm was always reciprocated by their team.

I would also like share my gratitude with my lab mates in the Mechatronics Research Lab for their help and friendship. They welcomed me into the lab with open arms and it has been a great pleasure working side-by-side with them each and every day.

Finally, my family has always been supportive of my educational pursuits, and their unwavering love has been a huge reason for my success at Penn State. I am so thankful for their sacrifices over the years and now can look forward anxiously to a rewarding career in engineering.

# CHAPTER 1

## INTRODUCTION

This thesis presents a study of passive, two-phase suspension systems for battery packs onboard off-road electric vehicles. The harsh environments in which these vehicles operate expose the battery packs to significant vibration and shock loading that can lead to battery damage and premature failure. Because these battery packs are extremely costly, it is often essential to utilize a suspension system to mitigate vibration and shock effects and ensure long battery life. Most conventional isolation systems are too bulky, delicate, or complex to viably apply to battery pack suspensions. The designs presented in this work combine two commonly-used passive isolators to achieve vibration and shock isolation while bypassing the inherent shortcomings that exist with passive isolation systems consisting of a single material. This chapter discusses the application and motivation for battery pack suspensions and outlines the suspension design process for an exemplary BEV and battery pack system.

### 1.1 BEVs for Off-Road Applications

Society's push to reduce greenhouse gas emissions has sparked tremendous investment into alternative energy technologies. Energy storage using rechargeable batteries proves to be an efficient, green solution for a wide variety of applications. Battery electric vehicles (BEVs), for instance, completely eliminate emissions by replacing conventional internal combustion engines with rechargeable battery packs. With the advancement of battery capabilities in recent years, electric automobiles have made great strides in the passenger vehicle market. The Nissan Leaf

and Tesla Model S, among others, have strongly demonstrated the environmental and cost benefits of BEVs [1].

Battery technology is not only being implemented in passenger vehicles, however. Off-road vehicle manufacturers are switching to battery power as well for a number of reasons. Fully-electric tractors and all-terrain vehicles (ATVs) have increased in the marketplace to cut down on fuel costs, emissions, and engine noise. The US military is following automotive manufacturers by investing considerably in hybrid electric lightweight vehicles such as the Humvee and Shadow RST-V. These vehicles not only reduce fuel economy, but offer improved thermal and noise stealth capabilities from the absence of combustion engines [2]. The mining industry has been one of the biggest commercial participants of fully-electric vehicles. In particular, underground mining has great reason to utilize batteries in vehicle propulsion systems as opposed to standard diesel engines. Not only is the cost of diesel fuel increasing, but there are safety concerns with potential spark ignition of the emissions generated by combustion engines. Furthermore, immense ventilation costs are incurred using these engines since it is necessary to evacuate the toxic emissions from the mine in order to establish safe working conditions [3]. Examples of underground mining BEVs are shown in Figure 1-1. Vehicle (a) uses lithium iron phosphate cells to fully power a haul truck developed by RHD Mining Equipment. Vehicle (b) is a lead-acid battery-powered load haul dump (LHD) vehicle by General Electric.

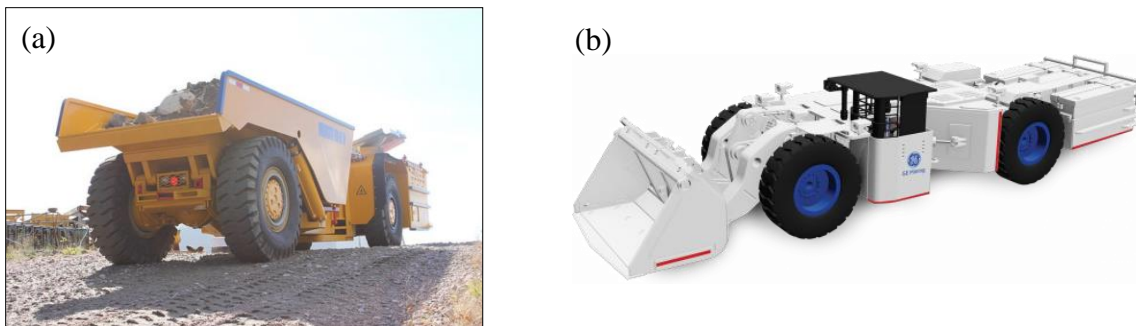


Figure 1-1. Battery electric mining vehicles [4, 5]

## 1.2 Effects of Shock and Vibration on Battery Life

A vital concern with installing batteries on vehicles is their exposure to vibration and shock loading. Shock and vibration can have detrimental effects on battery life through various failure mechanisms. Primarily, excessive loading can cause the internal components of batteries to improperly shift, potentially leading to short-circuiting or loss of connectivity [6]. Short circuiting describes the formation of an unintended, low-resistance current path in an electric circuit. The existence of this path is a primary source of battery failure as it generates excessively high current and heat, risking fire or explosion. Excessive vibration and shock may even cause structural failures of the casing as indicated by cracking. Over an extended period of time, miniature cracks can propagate and eventually result in premature battery failure. Depending on the battery installation, significant mechanical abuse can result from shock loading such as permanent puncture or deformation of the battery casing.

Because vibration and shock can have severe impacts on battery life and safety, many organizations have established testing standards and procedures to qualify vibration and shock durability of batteries. SAE International has developed test procedures to characterize the effect of long-term, road-induced vibration on batteries. One such standard is SAE Standard J2380, titled *Vibration Testing of Electric Vehicle Batteries*. This test utilizes a shaker table to subject a battery module to random vibration in the longitudinal, lateral, and vertical axes. Survivability test specifications are given as power spectral density limits, as shown in Figure 1-2. During the vibration testing, the battery is instrumented to test for electrical isolation, abnormal voltage, temperature, and unexpected resonance conditions. If full functionality is maintained at the conclusion of the experiment, the battery is deemed able to meet the vibration requirements [7].

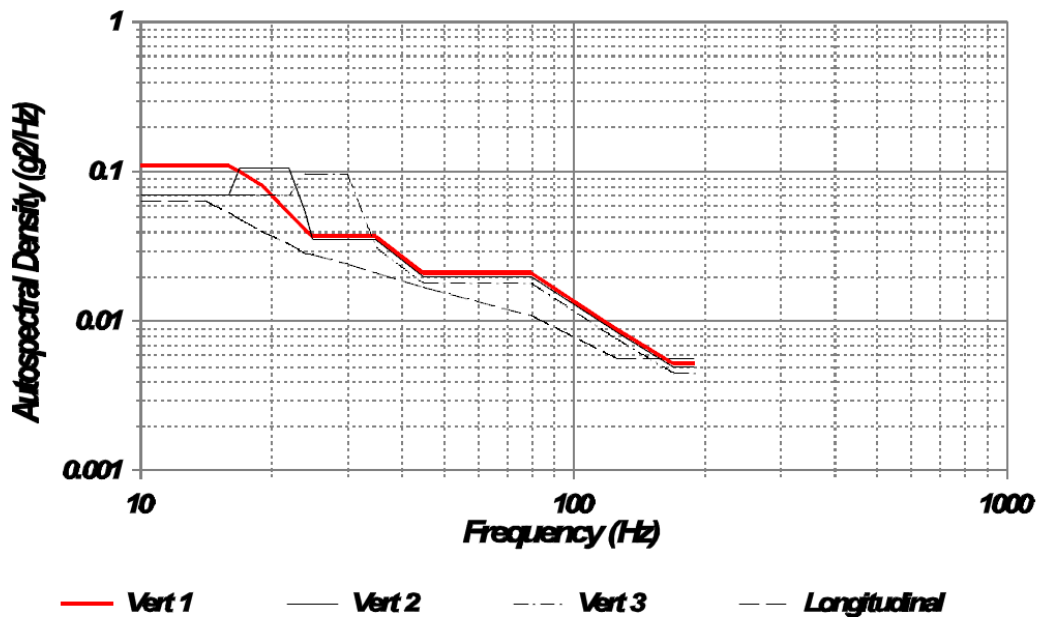


Figure 1-2. SAE vibration test specification for electric vehicle batteries [7]

SAE has also developed drop test and mechanical shock testing procedures for lithium-ion battery packs onboard electric vehicles. As an example, under SAE Standard J2464, a battery pack is subjected to shock loading and subsequently monitored for damage, explosion, or fire for up to 1 hour after the test has concluded [8]. This type of test is performed to analyze the extent to which electric vehicle batteries are affected by significant inertial loads caused by vehicle impacts.

### 1.3 Review of Shock and Vibration Isolating Suspensions

The engineering community has conducted extensive research in its quest to combat the negative effects of vibration and shock. Applications of this work span from the automotive industry to machinery and manufacturing, aircraft and space vehicles, seismic control of

buildings and structures, and beyond. One common approach to isolate an object from a source of vibration and shock is to suspend the object using one or more materials that possess favorable stiffness and damping characteristics. For successful vibration isolation, these suspensions continuously reduce the transmission of energy between the input source and the suspended object. Shock isolation, on the other hand, aims to minimize the acceleration (i.e. attenuation) of the object during a transient shock event. Generally, the characteristics that yield vibration isolation conflict with those that yield shock isolation, so compromises inherently exist in suspension design to effectively combat both vibration and shock excitations.

There are three fundamental classes of suspension design [9]. The most widespread class is passive suspension, which is typically the simplest, most reliable, and least expensive. Active suspension can provide the best isolation performance as it has the ability to bypass the inherent shortcomings of passive techniques with the use of sensing, actuation, and control. Finally, there are semi-active suspensions which can regulate energy dissipation to achieve better performance than standard passive systems. As with any design, there are tradeoffs in performance, complexity, and cost associated with these techniques. A literature review of suspensions utilizing these three classes of isolation methods is presented here.

### **1.3.1 Passive Suspension**

Passive suspension is the most widely-used approach to mitigate the negative impacts that vibratory and shock environments have on people, equipment, and structures. Passive suspensions use springs and/or dampers to cause energy isolation and absorption in the absence of any actuation or control. The classical single degree-of-freedom (SDOF) passive isolation

model is shown in Figure 1.3. This model contains a rigid mass suspended by a spring and damper that is acted upon by a base excitation.

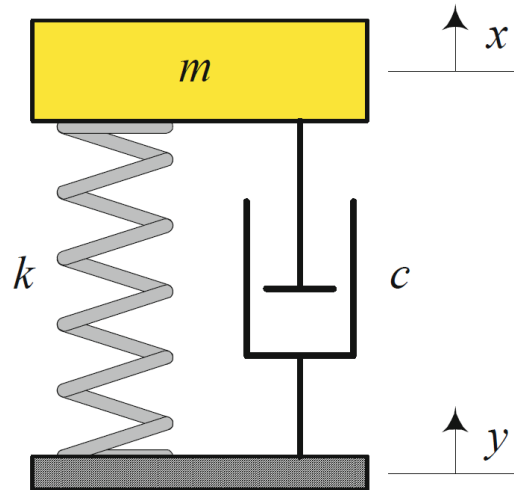


Figure 1-3. Conventional passive isolator [10]

There is an extensive catalog of materials that can provide the spring and damper characteristics shown in Figure 1-3. Different applications call for different suspension behaviors. This section presents some of the passive suspension materials that have been used for vibration and shock isolation.

One of the most prevalent applications of passive vibration and shock isolation systems is automotive suspensions. The MacPherson strut, for example, uses a coil spring and a fluidic damper to provide stiffness and damping to the vehicle chassis. The spring statically supports the vehicle's weight while the damper dissipates energy to minimize oscillations of the body. This simplistic design makes the MacPherson strut one of the most common independent suspension designs [10].

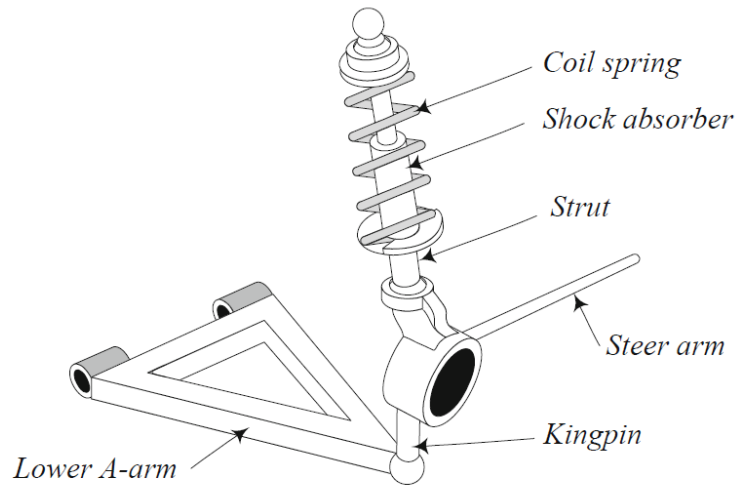


Figure 1-4. MacPherson strut [10]

Pneumatic isolators (i.e. air springs) have been extensively studied for vehicle suspensions among other vibration applications [11, 12]. Pneumatic isolators are rubber bladders filled with pressurized air. These systems have low natural frequencies and can statically support heavy loads by increasing their internal pressure. Esmailzadeh [13] looked into optimizing the damping characteristics of an air spring suspension by varying the resistance within air lines connecting the isolators to a surge tank. It was shown that very good vibration isolation can be achieved for a broad input frequency range [13]. Example air spring systems are shown in Figures 1-5 and 1-6.



Figure 1-5. Air springs used in fifth wheel tractor hitch [14]



Figure 1-6. Pneumatic isolator vehicle suspension systems [15, 16]

Engine mounts are another passive suspension application that must exhibit both vibration and shock characteristics. The roles of engine mounts are to 1) support the weight of the engine, 2) isolate the vehicle from engine vibration, and 3) prevent engine bounce from shock excitation [17]. Elastomers are one of the most common materials used in engine mounts. They can be tuned to meet multi-directional elastic stiffness rates for vibration isolation [17]. However, there is much room for improvement with these passive elastomeric mounts because tradeoffs exist between engine isolation, engine bounce, and static deflection. Incorporating nonlinear characteristics in the form of amplitude dependent stiffness and damping can help improve performance [17]. Alternatively, hydraulic engine mounts can achieve large damping by using fluidic orifices, inertia tracks, or inertia tracks and decouplers. As a result, shock attenuation is much improved when compared to elastomer engine mounts [17]. The use of a decoupler (an amplitude limited floating piston) allows for vibration isolation at higher frequencies without sacrificing the damping required for shock attenuation [17].

Mosher [18] conducted drop test experiments using elastomer and hydraulic mounts to analyze their capability of shock isolation. The three mounts utilized were a ½” thick neoprene pad, a 2.7” diameter tubular urethane mounting, and a hydraulic shock absorber. A rigid steel

bar was used as the baseline test. After dropping a 9 lb weight on each of these surfaces from a height of 51.75", Mosher concluded that all components achieved shock attenuation compared to the baseline test [18]. The drop test results are shown in Figure 1-7, where the y-axis represents the maximum acceleration (g's) calculated in a shock response spectrum (SRS) analysis.

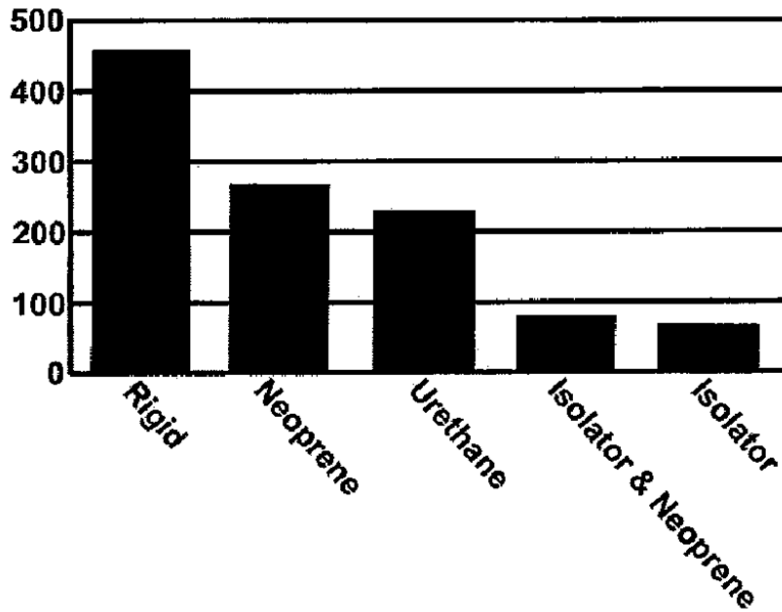


Figure 1-7. SRS maximum acceleration results from rudimentary drop test [18]

Silicone foam is another material that has been used for vibration and shock isolation. In the space industry, for example, silicone foam has been used for packaging of electronic Orbital Replacement Units (ORUs) that service the Hubble Space Telescope [19]. Isolation of ORUs is critical to ensure that no damage is sustained during transportation to space. In this application, silicone foam is distributed symmetrically about the ORU to avoid cross-coupling effects between axes [19]. The softness of open cell silicone foam attenuates the high frequency random vibration environment experienced during lift-off. Furthermore, the inherent damping of silicone foam helps attenuate transient shock loading [19].

The final passive isolator presented in this review is the wire rope isolator. Wire rope isolators have been extensively utilized for shock and vibration isolation in military and industrial applications [20]. Demetriades et al. [21] used wire rope isolators to protect equipment from seismic excitation. A setup of the test stand is shown in Figure 1-8. Four isolators are installed underneath a cabinet weighing 1784 N which is placed on top of a shaker table. Seismic excitation was applied in both the vertical and transverse directions to subject the isolators to combined vertical and roll motions. The experimental results concluded that wire rope isolators exhibited small displacements, large energy dissipation, and prevented the occurrences of vibratory resonances. In comparison to a fixed system, the cabinet's acceleration responses were substantially reduced [21].

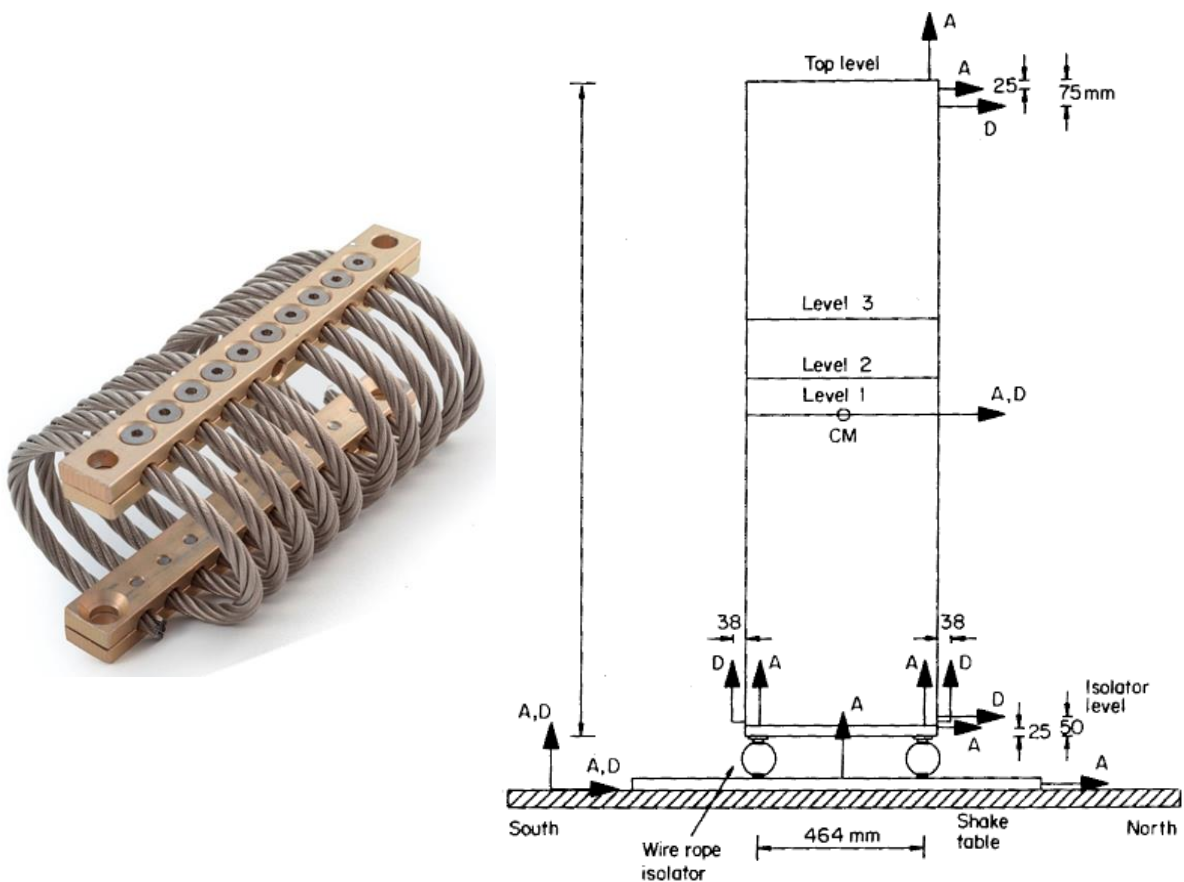


Figure 1-8. Helical wire rope isolator (left) and seismic test stand (right) [31, 21]

### 1.3.2 Semi-Active Suspension

Semi-active suspensions characterize isolation techniques that actively manipulate performance properties of passive elements. A similarity with passive suspension is that semi-active suspension does not utilize any actuation force to counteract vibratory motion. However, with the use of sensors and control algorithms, the dissipation of energy can be continuously regulated to yield vibration and shock isolation over a broad range of frequencies.

Semi-active dampers were first introduced in the early 1970s [9]. Their functionality was designed to generate optimal isolation transfer functions between a mass and a moving base used in skyhook damping systems [9]. The skyhook damping concept, shown in Figure 1-9, produces damping force that is proportional to the absolute velocity of the moving mass, as opposed to the mass' relative velocity as in traditional passive systems. The term skyhook represents a theoretical approach of connecting a damper to a stationary object outside of the moving frame, when in practice this may not be the case. Karnopp et al. [22] proved that control laws applied to semi-active suspensions can significantly reduce resonant peaks without compromising vibration isolation at higher frequencies.

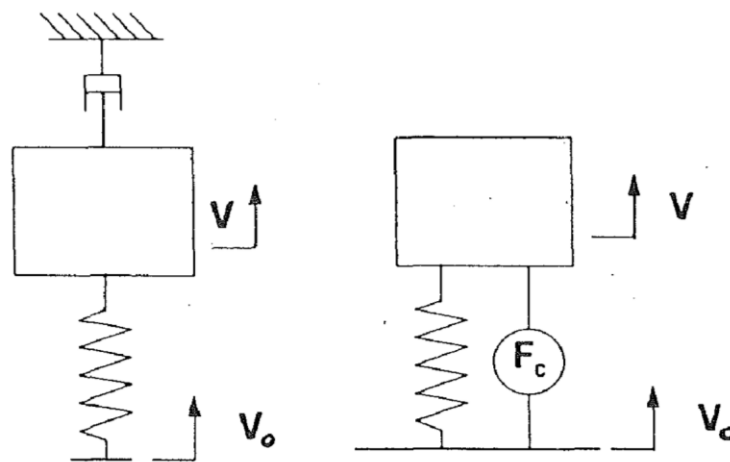


Figure 1-9. Skyhook damping diagram [9]

Within the last two decades, electrorheological (ER) and magnetorheological (MR) fluids has been studied for semi-active vibration control. These materials have the unique ability to change their viscosity in the presence of electric or magnetic fields. Choi et al. [23] performed experiments using a single degree-of-freedom (SDOF) suspension system with a MR semi-active damper. Figure 1-10 shows a schematic diagram of the MR damper. The damping force produced by the MR damper varied in response to magnetic field strength which is proportional to applied current. With the use of a simple skyhook controller, the semi-active system yielded improved vibration isolation across many frequencies as compared to the passive system when applied current was constant [23].

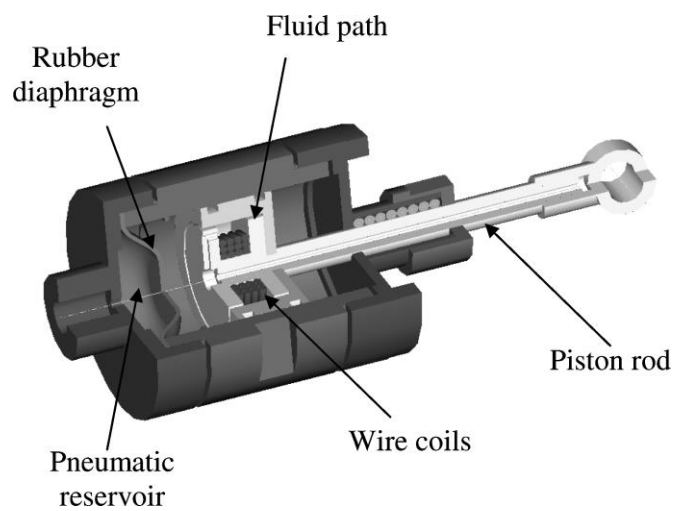


Figure 1-10. Schematic diagram of MR semi-active damper [23]

Furthermore, Choi and his colleagues [24] performed vibratory control simulations using MR semi-active dampers for a six degree-of-freedom (6DOF) precision sensor for aerial vehicles. The test diagram is shown in Figure 1-11. Three MR dampers suspend the sensor from underneath at equiangular positions. A linear quadratic Gaussian (LQG) control algorithm was

designed to control the applied current to each of the dampers. Given shock loading, it was observed that the semi-active MR isolation system had substantially improved shock attenuation as well as achieved more rapid regulation of the sensor assembly's displacement [24].

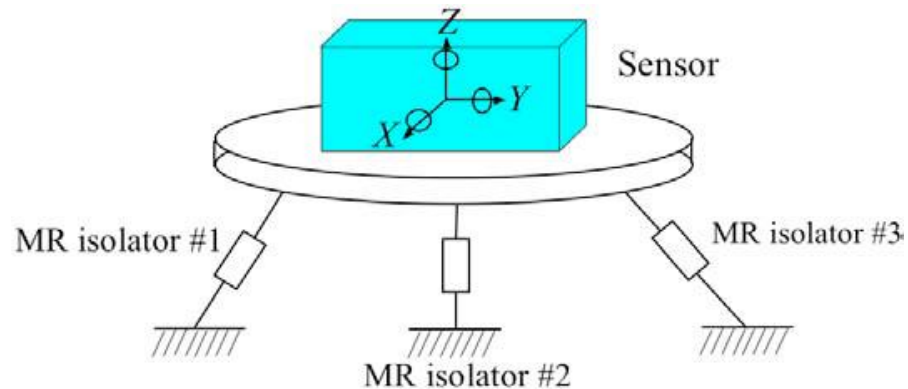


Figure 1-11. Precision sensor suspension system using semi-active MR isolators [24]

### 1.3.3 Active Suspension

Active suspension systems can provide the best shock and vibration isolation by using controlled actuators to effectively supply external energy to a system. This technique requires sensing, control, and actuation, which make active suspensions the most expensive and complex isolation systems. The method is for actuators to apply force to the moving body at the perfect time and magnitude to cancel out unwanted motion. Common types of actuators are hydraulic and electromagnetic.

Commercially available active suspensions became available for passenger vehicles by the 1990s [9]. Although such systems have clear advantages over passive suspensions, there are many downsides as well [9]. Hydraulic actuation requires much more packaging room as there needs to be an accumulator and pump onboard the vehicle. Electromagnetic suspensions use many permanent magnets and current coils that add considerable weight and power demands to

the vehicle. While active suspensions have been proven to be effective, often times their complexity and cost make them far less desirable than their passive and semi-active counterparts [10].

## **1.4 Research Objectives**

The fundamental objective of this work is to study the effectiveness of battery pack suspensions comprising wire rope isolators and silicone bump stops used on commercial off-road BEVs. This research is motivated by the fact that the harsh conditions sustained by these battery packs make them extremely prone to damage and premature failure. Many of the vibration and shock isolation techniques currently found in literature cannot be applied to battery pack suspensions as the packs are often too heavy and too confined in tight enclosures.

The combined use of wire rope isolators and silicone bump stops may present reliable, two-phase passive suspensions that can tackle vibration and shock loading seen by off-road BEVs. The feasibility and effectiveness of such designs is analyzed through dynamic modeling and simulation. The simulation results will highlight the designs' ability to meet static and dynamic requirements of an exemplary mining vehicle battery pack and will ultimately provide insight as to their benefits for battery pack survivability.

## **1.5 Thesis Outline**

The remainder of this document is organized as follows: Chapter 2 discusses the background and design requirements for an exemplary battery pack system onboard a General

Electric underground mining vehicle. The generic suspension design for the battery pack is presented in Chapter 3. The suspension is composed of two passive materials, wire rope isolators and silicone sheets, which are characterized in further detail. Chapter 4 details the formulation of a six degree-of-freedom dynamic model, representing the battery suspension system as a compilation of spring and damping forces acting on a rigid body. The equations of motion of the battery pack are derived in Chapter 5. Next, Chapter 6 presents three data profiles that characterize vibration and shock base accelerations. Simulation results for statically-feasible suspension designs are shown in Chapter 7. Finally, conclusions of this battery pack suspension study are drawn in Chapter 8. The Appendix contains the file structure of the model's implementation in MATLAB as well as step-by-step user instructions.

## CHAPTER 2

### BACKGROUND AND REQUIREMENTS

This work details the design and modeling of battery pack suspensions for a General Electric (GE) underground coal mining vehicle (see Figure 2.1). GE is developing a new propulsion system for this vehicle that replaces currently-used lead-acid batteries with GE's own Durathon Battery technology [26]. The underground scoop is exposed to a variety of harsh conditions during mining operations caused by driving along bumpy terrain, colliding with mine walls, and running over obstacles. This environment generates extreme vibration and shock loading for the onboard Durathon Batteries that may result in damage and premature failure. Consequently, a suspension system for the batteries is required to ensure that they operate safely and reliably over their desired lifetimes.



Figure 2-1. GE Fairchild underground mining scoop [27]

## 2.1 Battery Installation

The Durathon Battery is GE's energy-storing technology utilizing sodium-nickel-chloride chemistry [28]. Rechargeable cells, which operate at temperatures above 300°C, are strung together in a thermally-insulated battery module, maintaining external surface temperatures within 10-15°C of the ambient environment [28]. The battery modules will be enclosed within a master carrier tray that is suspended at the rear of the vehicle by hydraulically-actuated lifting arms. Figure 2-2 illustrates the location of the carrier tray with respect to the vehicle. Eight modules inside the tray will be arranged in two stacked rows of four, as shown in Figure 2-3.

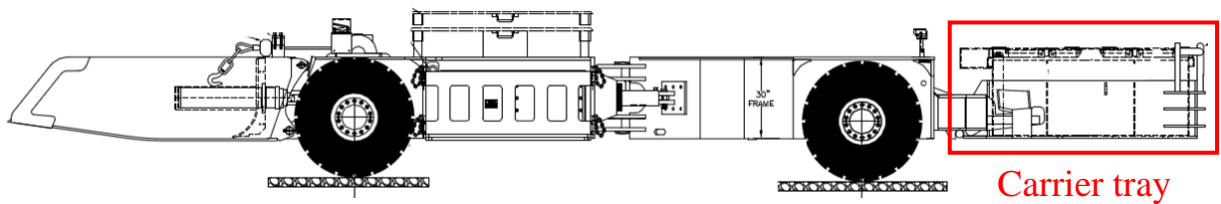


Figure 2-2. Carrier tray suspended by lifting arms behind the rear tires

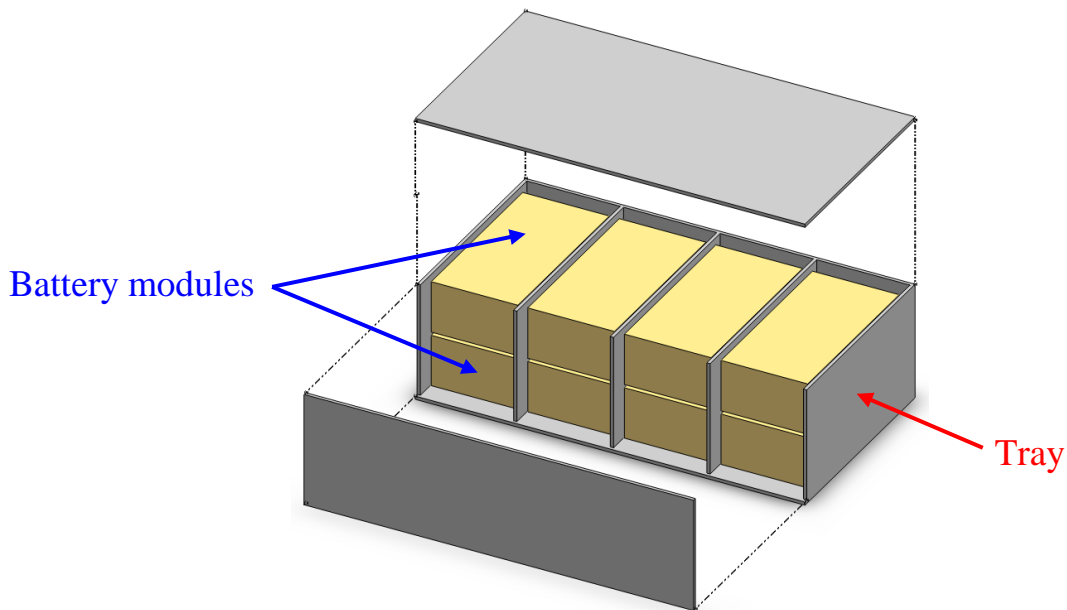


Figure 2-3. Exploded view of tray containing Durathon Battery modules

The external dimensions of the tray are highly constrained for a multitude of reasons. The vertical height is minimized in order to 1) maintain adequate ground clearance and 2) avoid interfering with the driver's visibility. The lateral dimensions are restricted as well to assist with vehicle maneuverability through tight mining passages. Consequently, tight clearances will exist between the battery modules and the inner walls of the tray.

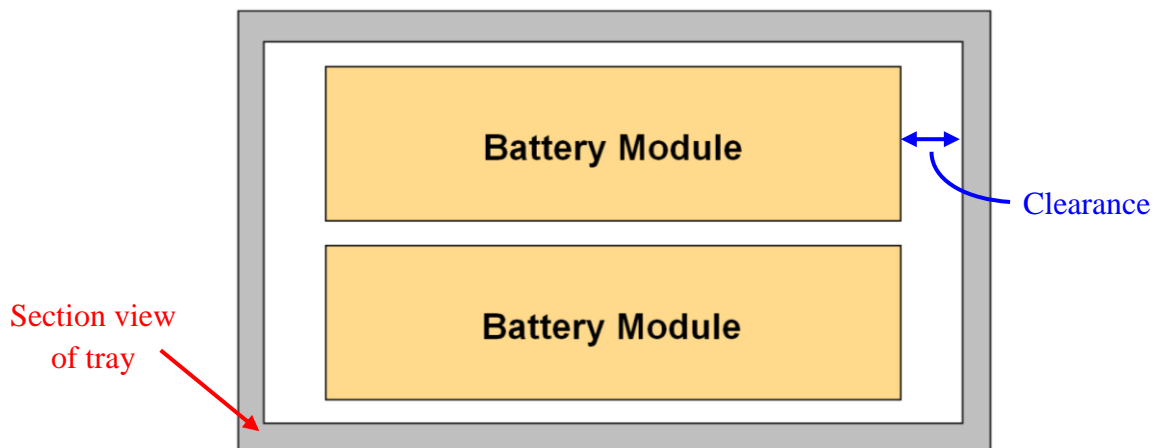


Figure 2-4. Side section view of battery-tray system

## 2.2 Design Requirements

The battery suspension system must achieve many performance requirements to protect the battery modules from rigorous base accelerations sustained by the carrier tray. Specifically, the batteries must exhibit vibration isolation at frequencies of 35 Hz to filter out damaging resonances of the inner cells. The suspension also aims to attenuate all shock impacts encountered by the tray. All materials must comply with the given clearances surrounding each battery, which are approximately 0.75" on the top, bottom, and lateral faces, and 3" on the front and rear faces. Furthermore, the suspension design should be cost-effective, reliable, and maintenance-free for a desired lifetime of 10+ years.

## CHAPTER 3

### SUSPENSION SYSTEM DESIGN

After a review of suspension design literature, a conceptual suspension design for battery packs is proposed in Figure 3-1. This suspension system comprises wire rope isolators that will statically support each battery and will be responsible for successfully meeting the specified vibration requirements. Because of the extent to which shock impacts are prevalent in underground mining, a secondary suspension material is needed as a safety bumper. This “bump stop” material will be made from silicone foam or rubber sheets. Together, the wire rope isolators and bump stops create a passive, two-phase suspension system that can be tuned to meet both vibration and shock loading criteria while contained within the tight clearances available. All materials are maintenance-free, readily-available in industry, and can withstand the mechanical and temperature conditions of mining environments.

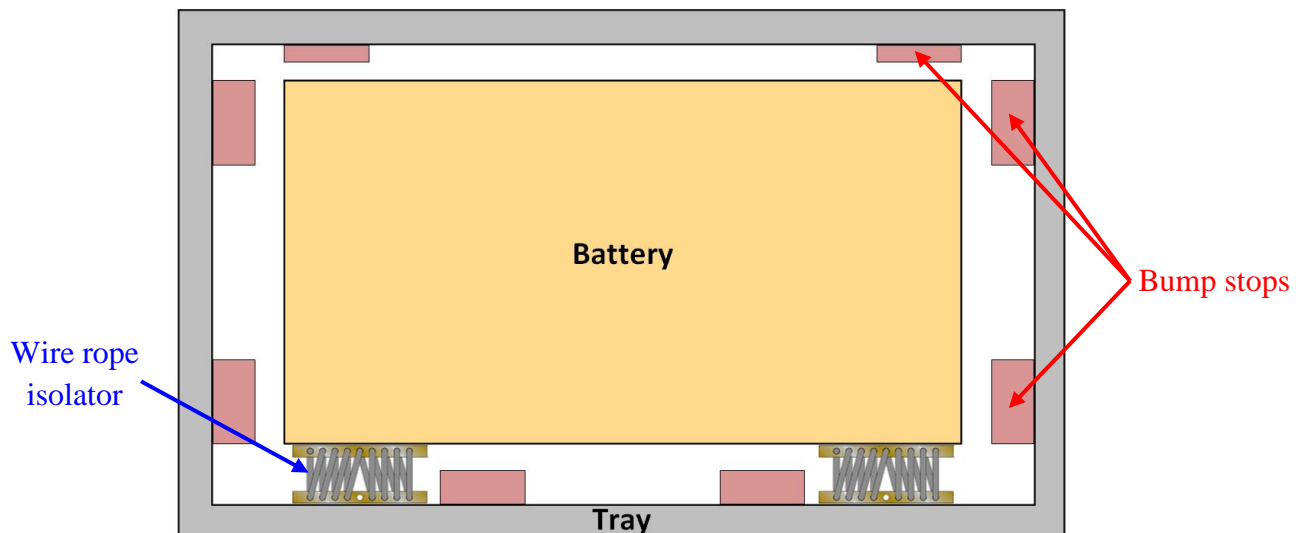


Figure 3-1. Suspension system conceptual design

This chapter elaborates on each component of the conceptual design. First, the two suspension system materials, wire rope isolators and silicone sheets, are presented. Background information pertaining to each of these classes of materials, as well as their performance characteristics, are described in Sections 3.1 and 3.2. Next, two assembly configurations using wire rope isolators are illustrated. One configuration supports the battery from underneath, while the other uses a side-supporting installation. Finally, the utility of the bump stops is detailed in Section 3.4.

## 3.1 Wire Rope Isolators

### 3.1.1 Background

Wire rope isolators are effective products for shock absorption and vibration isolation [29, 30]. They are composed of stainless steel cable that is threaded through two aluminum alloy mounting bars [30]. Figure 3-2 shows a typical wire rope isolator containing 10 loops.



Figure 3-2. Helical-style wire rope isolator [31]

A spring-like quality is imparted to the wire rope coils by displacing the mounting bars relative to one another [30]. The resulting spring forces can be multi-axial, as there are many modes of deflection [32]. Specifically, wire rope isolators exhibit four independent displacement modes: compression, tension, shear, and roll. The modes can even be combined to result in compression-roll and tension-roll deflections. Figure 3-3 shows the deflection patterns corresponding to these modes. Isolators are also able to dissipate energy via frictional damping because the individual strands of wire rope rub against one another during deflection.

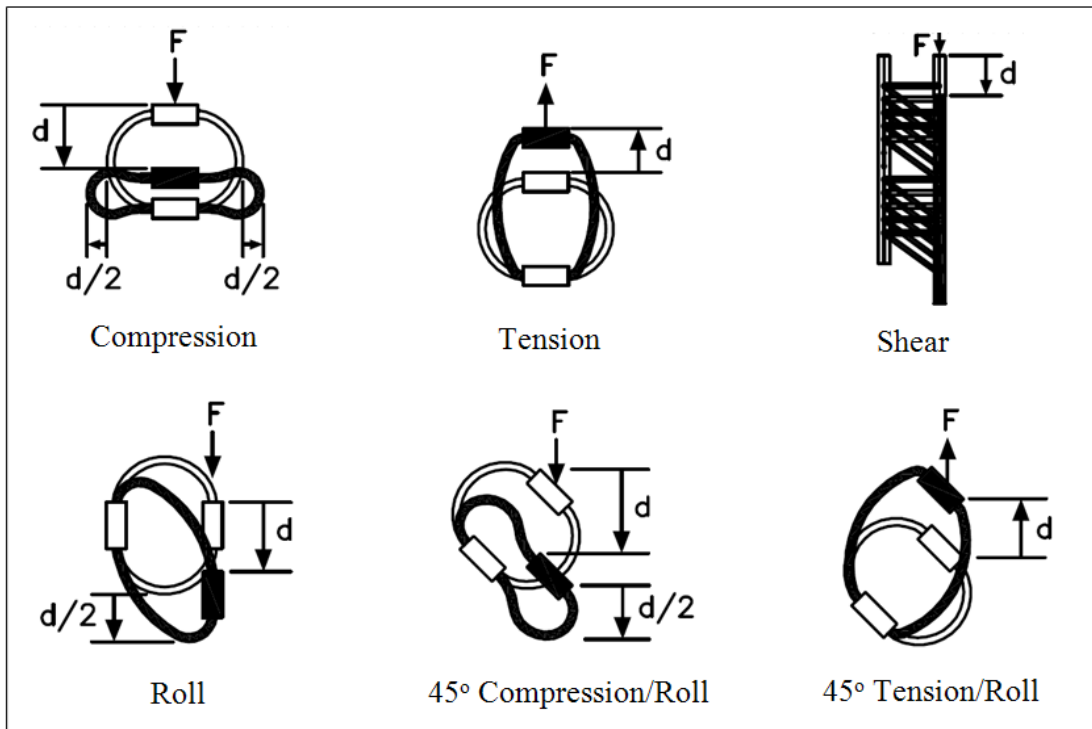


Figure 3-3. Deflection modes of wire rope isolator [32]

Wire rope isolators can accommodate a wide scope of vibration applications since they are manufactured in many different sizes [29, 32]. Their performance, for instance, can be readily tuned by identifying the number of cable loops, the diameter of the loops, and the diameter of the cable that comprise a particular isolator. This fact, combined with the isolators'

ability to dissipate energy and deflect in multiple modes, make them one of the most versatile vibration products on the market [32].

### 3.1.2 Performance Characteristics

There are some performance criteria to consider when selecting a wire rope isolator for a particular application. In terms of static considerations, an isolator has a static length, width, and height. The height and width relate to both the cable and loop diameters. As an example, Figure 3-4 illustrates the geometric properties of the M6 series of isolators provided by Isolation Dynamics Corp (IDC). The M6 series encompasses isolators with a cable diameter of 3/16". There is also a recommended range of loads that an isolator can statically support. Applying static loads outside of this range leads to instability. The recommended static load range for the M6 isolators in compression is labeled between ① and ② on the load-deflection curve, as shown in Figure 3-5.

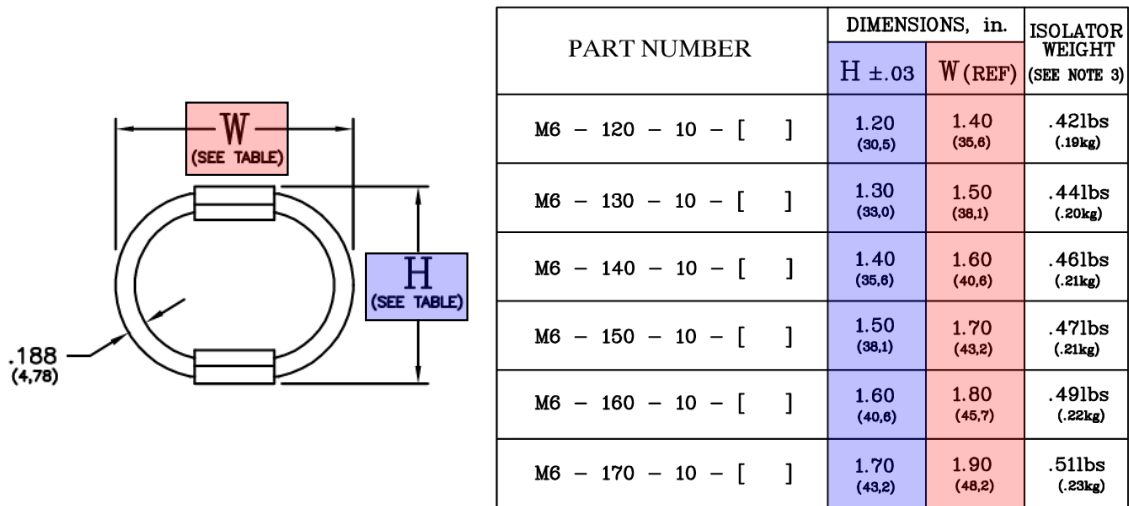
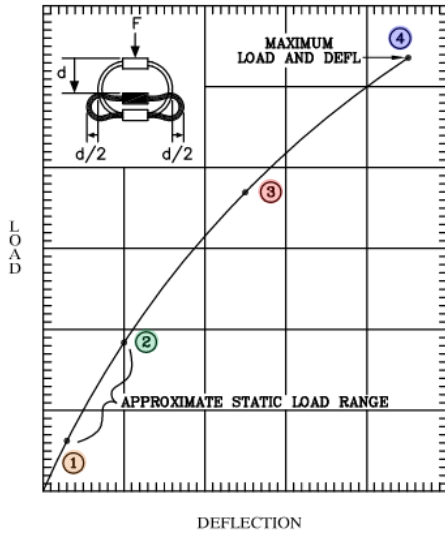


Figure 3-4. Geometric properties of M6 isolators sold by IDC [32]

**COMPRESSION**



PART NO.	①		②		③		④		$K_v$ (VIBE) (lbs/in)	$K_s$ (SHOCK) (lbs/in)
	LOAD (lbs)	DEFL (in)	LOAD (lbs)	DEFL (in)	LOAD (lbs)	DEFL (in)	LOAD (lbs)	DEFL (in)		
M6-120-10	210	.05	370	.10	580	.18	750	.35	4200	3200
M6-130-10	160	.05	280	.10	470	.22	610	.45	3200	2150
M6-140-10	125	.05	215	.10	440	.28	580	.55	2500	1575
M6-150-10	95	.05	160	.10	360	.35	490	.70	1900	1025
M6-160-10	70	.05	120	.10	350	.40	460	.80	1400	875
M6-170-10	55	.05	100	.10	300	.45	420	.90	1100	875

Figure 3-5. Compression load-deflection curve for M6 isolators [32]

In terms of dynamic characteristics, IDC provides two linear spring constants ( $k_v$  and  $k_s$ ) for each mode of deflection. These linear stiffness values approximate the nonlinear load-deflection curves in different regions.  $k_v$  is the spring constant for vibration applications, where the deflections remain close to the origin.  $k_s$  is the shock spring constant that approximates the entire deflection range for that particular mode. Finally, an isolator exhibits a maximum dynamic deflection and load, as depicted as ④ in Figure 3-5. This maximum represents the upper limit of the operable range of an isolator. Exceeding this limit may damage the isolator by inducing high tensile stresses in the coils or even colliding the mounting bars together. Thus, it is imperative that an isolator is never placed in an environment where it displaces outside of that operable deflection range [32].

Characterizing the damping properties of wire rope isolators is very challenging since dissipation is a function of both the size of the isolator as well as the input to the system [29]. ITT Enidine provided a reference damping curve for their WR3-800-10 isolator, as shown in Figure 3-6. The curve was developed experimentally, exciting the wire rope system with a sinusoidal input. As can be seen, the damping changes nonlinearly with input level. However, since energy dissipation is both isolator and application specific, vendors tend to provide very general damping information, such as an average damping ratio. Some vendors estimate the damping ratio to be approximately 20% [32].

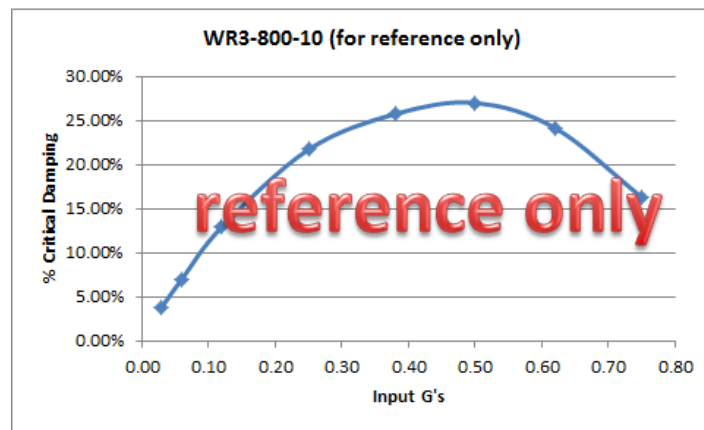


Figure 3-6. Example damping behavior of an Enidine wire rope isolator

## 3.2 Silicone Sheets

### 3.2.1 Background

Silicone foam is an exceptionally versatile elastomer commonly used for cushioning, vibration isolation, sealing, and insulation [33]. Some of its properties include being flame resistant, having low compression-set and creep, and being resistant to mechanical fatigue. In

addition, silicone has the unique ability to maintain its mechanical and thermal properties at very high temperatures [33].

BISCO Silicones by Rogers Corporation is an industry leader in manufacturing both cellular silicone foams, as well as solid silicone rubber pads [33]. Both are sold in roll-form and are available in a wide range of thicknesses and densities/durometers (densities differentiate cellular foams and durometers are a measure of hardness of the rubber pads). A picture of closed-cell silicone foam is shown in Figure 3-7. Unlike wire rope isolators, silicone sheets only sustain one primary mode of deflection: compression. In these battery pack suspension systems, the sheets will only physically attach to one surface, so they will never go into tension. Energy dissipation of silicone is generally poor and does not produce substantial damping [34].



Figure 3-7. Closed-cell silicone foam [35]

Silicone foam/rubber is chosen as part of the preliminary suspension design for a few reasons. First, its dynamic properties are well documented in literature, allowing for accurate modeling and simulation. Secondly, its performance is very tunable by changing the area,

thickness, and density/durometer of a sheet. Finally, the thermal insulation properties of silicone are beneficial for the molten cells of the Durathon Batteries. Although the battery thermal requirements are not discussed in this thesis, silicone is known to be a reliable product in battery pad separators in hybrid electric vehicle design [33].

### **3.2.2 Performance Characteristics**

The vibration performance of silicone sheets is dependent on a few physical properties. The density of cellular silicone foams affects the slope of the load-compression curve. Denser foams typically have steeper load-compression curves, keeping all other parameters the same. Similarly, the durometer of silicone rubber pads indicates the slope of the curve. These parameters can be thought of as the intrinsic stiffness of the material. In general, silicone pads are stiffer than silicone foams [33].

Compressive force is not only dependent on the intrinsic material properties, but is also directly proportional to the area that is acted upon. This means that for a given deflection, doubling the area of a silicone sheet will double its compressive force. Equivalently, given a compressive force, doubling the area will reduce the silicone's deflection by half.

Furthermore, the deflection of silicone sheets is directly proportional to the material's thickness. A given load compresses a sheet twice as much if its thickness is doubled. As with wire rope isolators, there is a maximum rated deflection for these silicones. Exceeding this maximum deflection may plastically deform the material and compromise its performance.

BISCO Silicones provides force-deflection data for their cellular foam and solid pad products. Table 3-1 contains this data for six cellular foams, which is also curve-fit using polynomials and displayed in Figure 3-8. Force-deflection curves for BISCO solid pads are shown in Figure 3-9.

Table 3-1. BISCO cellular silicones compression modulus [33]

% Compressed	FORCE (psi)					
	BF-2000	BF-1000	HT-870	HT-800	HT-820	HT-840
10	0.23	1.2	2.8	3.6	6.2	10.5
25	0.34	2.5	4.4	8.3	16.7	21.8
40	0.81	3.6	6.2	13.7	30.2	37.7
55	2.30	6.2	10.2	24.9	56.5	75.5
70	6.30	15.7	25.0	60.9	150.5	---

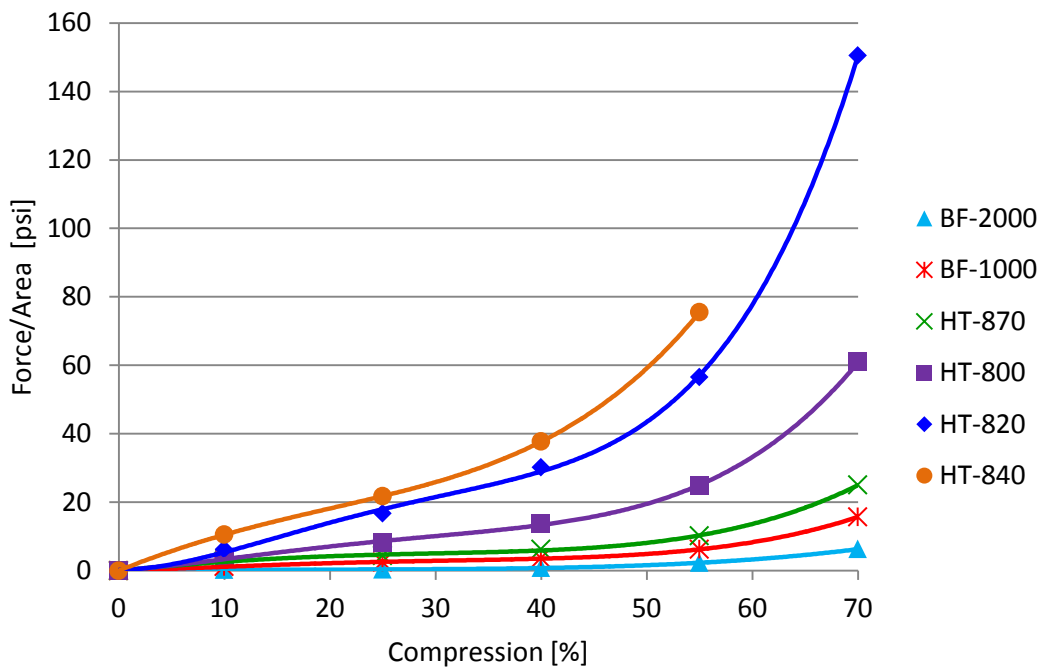


Figure 3-8. Force-deflection polynomial curve fits for BISCO cellular silicone foams

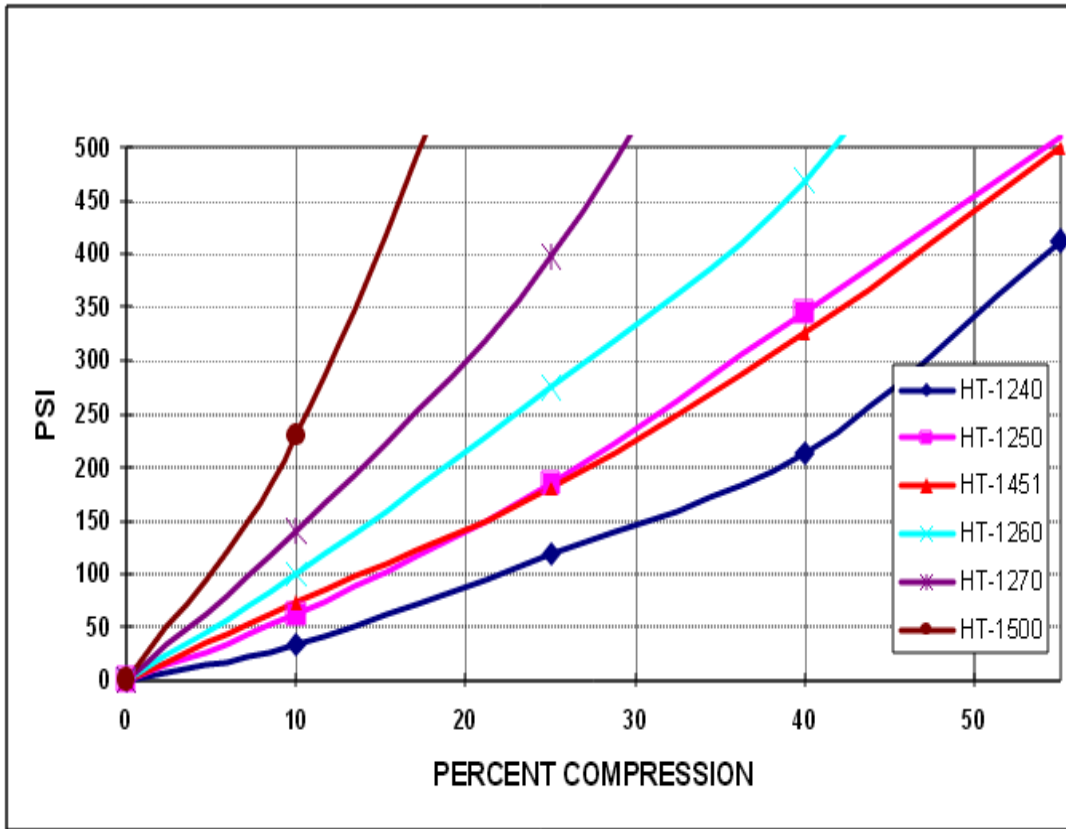


Figure 3-9. Force-deflection curves for BISCO solid silicone pads [33]

### 3.3 Assembly Configurations

Two assembly configurations are investigated to suspend the batteries from the carrier tray. The first is a stacked approach, where two batteries are connected together and supported from underneath by wire rope isolators. The second configuration supports each battery independently by wire rope isolators installed on the front and back battery faces. Further descriptions of these configurations are provided in Sections 3.3.1 and 3.3.2.

### 3.3.1 Stacked Configuration

One proposed method of assembling the batteries inside the tray is to vertically stack two batteries on top of one another. The top and bottom batteries are secured together such that they move as one rigid body. Wire rope isolators are installed in compression underneath the bottom battery, connecting the stack to the floor of the tray. Figure 3-10 shows the stacked configuration. Design considerations such as the size, location, and number of isolators are investigated in Chapter 7.

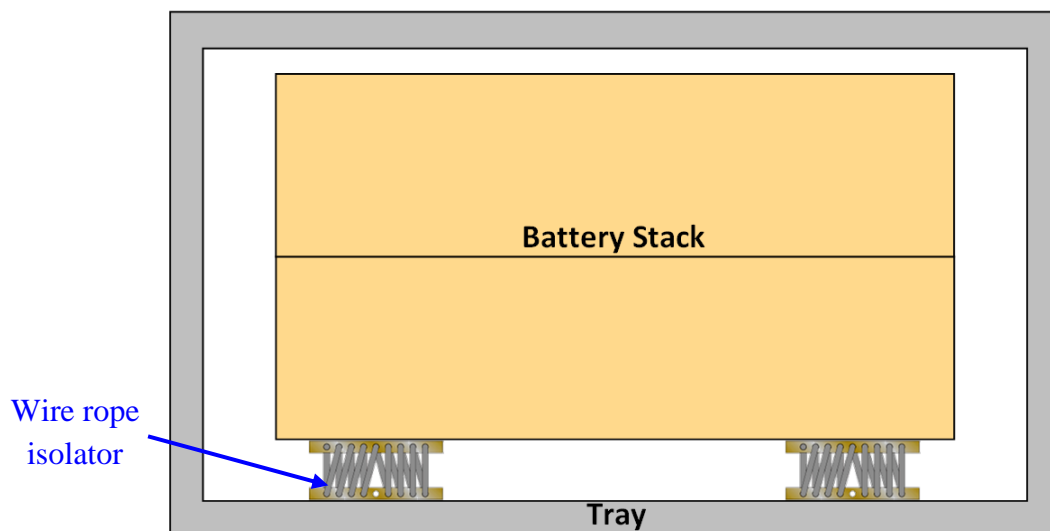


Figure 3-10. Side view of stacked battery configuration

### 3.3.2 Single Battery Configuration

The second assembly configuration supports each battery individually with wire rope isolators. The isolators are installed on the front and back faces of the battery, connecting the battery to the front and back inner walls of the tray. Horizontal protruding brackets allow the isolators to be placed in compression, as shown in Figure 3-11. Again, design considerations such as the size, location, and number of isolators are investigated in Chapter 7.

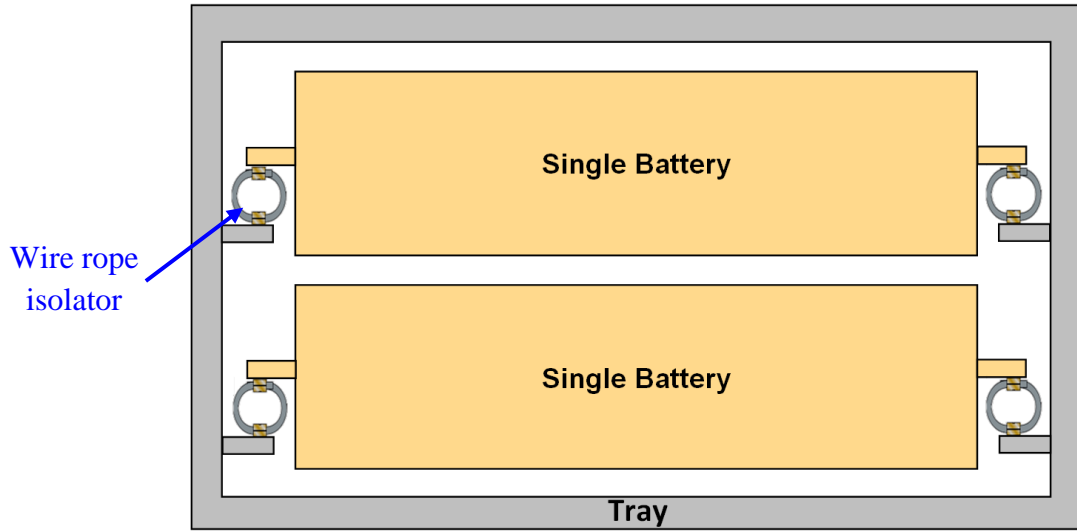


Figure 3-11. Side view of single battery configuration

### 3.4 Bump Stops

It is absolutely critical to design the suspension system such that the battery and tray never collide with one another. Moreover, the wire rope isolators must always operate within their rated operating range. In order to guarantee these requirements, safety bump stops are incorporated in the design. The bump stops engage the battery after a certain amount of displacement to prevent “bottoming” of the wire rope isolators, or collisions between battery and tray. Bottoming is defined in this work as the situation when a wire rope isolator’s travel exceeds the maximum rated displacement specified by the vendor.

Silicone sheets are the preliminary material choice for the bump stops. These sheets are attached to the inner walls of the tray. The addition of the bump stops creates a passive, two-phase suspension design, where the battery attaches to wire rope isolators at all times, but only engages with the bump stops at larger displacements. Figures 3-12 and 3-13 exemplifies how the battery engages with the bump stops for multiple deflection modes.

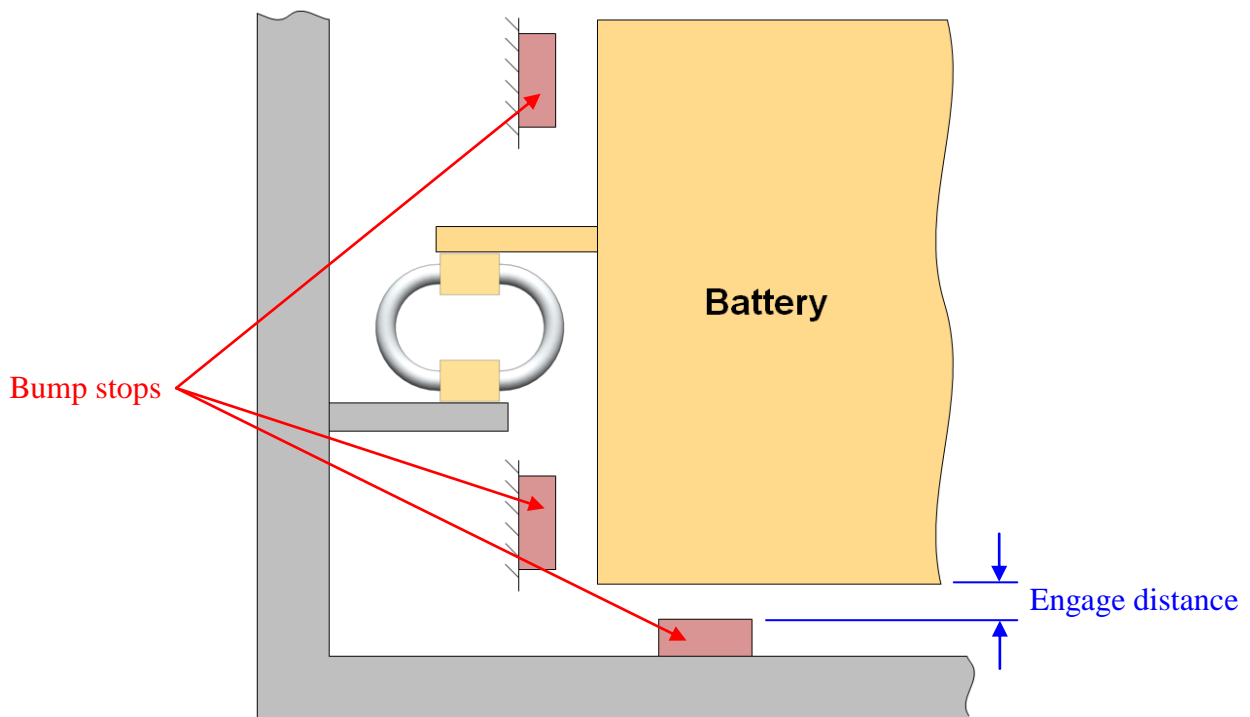


Figure 3-12. Bump stops constrain the maximum travel of the battery and isolators

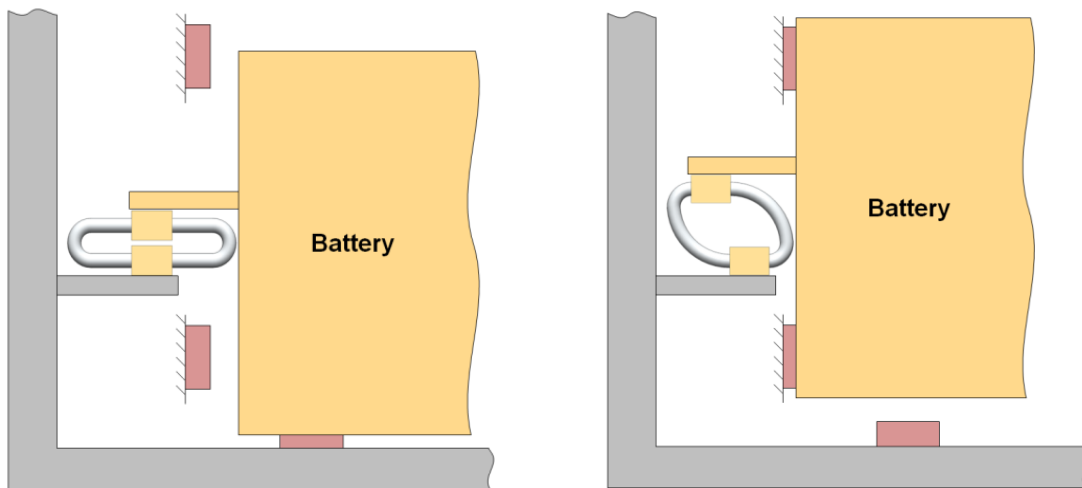


Figure 3-13. Bump stops engaging battery in compression (left) and roll (right)

Besides tuning the properties and sizes of the silicone materials, the amount of distance that the battery travels before engaging the bump stops is an additional tunable parameter. The effect of this “engage distance” is explored in Chapter 7.

## CHAPTER 4

### MODEL FORMULATION

A six degree-of-freedom (6DOF) dynamic model is developed to predict the behavior of a battery module when incorporating different suspension system designs. Modeling is a very cost-effective and timely approach to simulate the system's expected performance before investing time and funds into ample experimental testing. The modeling procedure is as follows: first, the battery and tray are modeled as rigid bodies and are described with local coordinate systems. The interface between the battery and tray is modeled as a collection of springs and dampers, which replicate the performance characteristics of the wire rope isolators and bump stops. The battery dynamics are then mathematically represented by differential equations of motion, organized using inputs, states, and outputs. Next, multiple suspension system designs are derived by changing material sizes and attachment locations. The batteries' responses to various base acceleration inputs are then simulated using numerical integration of the governing equations. This chapter illustrates the formulation of the dynamic model.

#### 4.1 Modeling of Battery

The battery is modeled as a rigid body, having mass  $m$ , mass moments of inertia  $J_x, J_y, J_z$ , and dimensions  $L_x, L_y, L_z$ . The battery's mass is assumed to be uniformly distributed throughout its volume, resulting in the center of gravity (CG) being located at its geometric center. A body-fixed coordinate system, referred to as the battery coordinate system, is attached to the battery's CG, as shown in Figure 4-1.

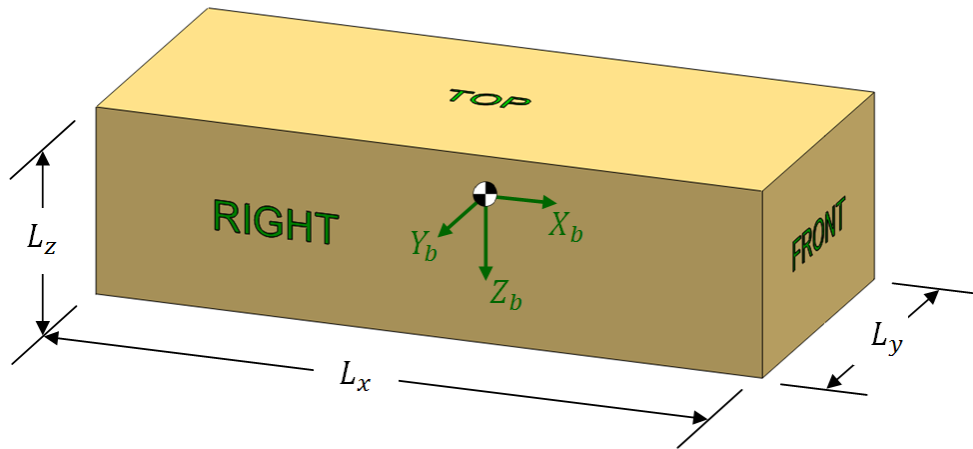


Figure 4-1. Rigid body battery model

Table 4-1. Battery parameters

Parameter	Single Battery	Battery Stack	Unit
$m$	412	724	kg
$L_x$	1.162	0.989	m
$L_y$	0.498	0.456	m
$L_z$	0.313	0.536	m

The parameters of the battery/battery stack are listed above in Table 4-1. Using these values, the mass moments of inertia about the principal  $x$ ,  $y$ ,  $z$  axes are calculated as

$$J_x = \frac{1}{12} m(L_y^2 + L_z^2) \quad (4-1)$$

$$J_y = \frac{1}{12} m(L_x^2 + L_z^2) \quad (4-2)$$

$$J_z = \frac{1}{12} m(L_x^2 + L_y^2) \quad (4-3)$$

## 4.2 Modeling of Tray

The carrier tray is also modeled as a rigid body. For simplicity, only one battery module or stack of battery modules within the tray is analyzed at a time. A second body-fixed coordinate system, called the tray coordinate system, is fixed to a point in the tray's reference frame such that both the tray and battery coordinate systems are coincident and aligned at static equilibrium. That is, the CG of the battery in its equilibrium state has zero relative displacement with respect to the origin of the tray coordinate system. Static equilibrium is discussed further in Section 4.5. Figure 4-2 illustrates three section views of the system at equilibrium, showing the tray coordinate system and its coincident location with the battery's CG.

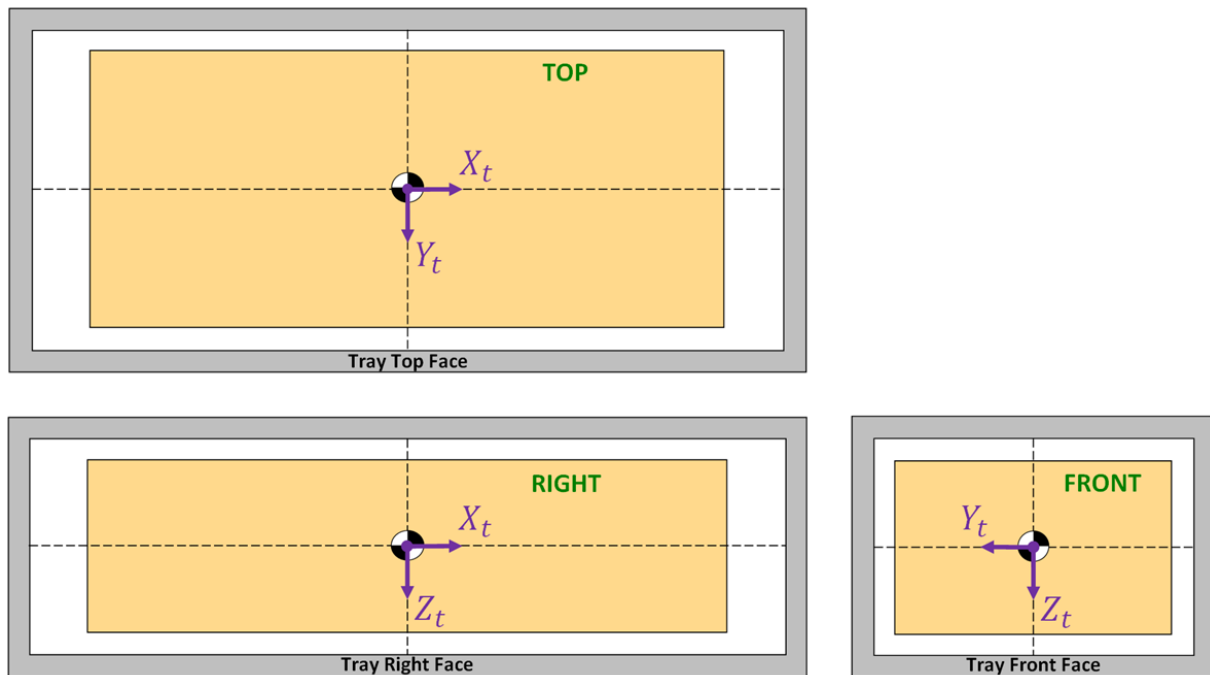


Figure 4-2. Location of tray coordinate system at static equilibrium

### 4.3 Modeling of Wire Rope Isolators

Wire rope isolators have been mathematically modeled by past researchers with aims of accurately simulating their dynamic behavior [21, 36, 37]. Many different methods have been developed of varying complexities; most are partially based on empirical data required to calculate and tune model parameters [36, 37]. However, Demetriades et al. [21] discusses a simplified analytical model that yields accurate peak acceleration responses without the need of experimentally-obtained hysteretic data. This procedure only required an effective linear stiffness and equivalent viscous damping ratio to characterize the peak dynamics of a wire rope isolator used for equipment seismic protection [21]. The objective of modeling wire rope isolators in this work is to use simplistic vibration modeling principles in the absence of experimental testing. All of the dynamic characteristics are taken from vendor catalogs and website information.

In this thesis, the wire rope isolators are modeled as a collection of springs and dampers. As explained in Section 3.1, wire rope isolators exhibit multiple deflection modes. Some assumptions are made to simplify the behavior of these deflections. First, it is assumed that any interaction between deflection modes is negligible, and that an isolator is represented as three orthogonal axes containing one spring and one damper element connected in parallel. The properties of these springs and dampers are discussed in Sections 4.3.1 and 4.3.2. It is also assumed that maximum rated deflections of each mode (as specified by the vendor) can occur simultaneously. Lastly, the spring and damper forces all act at a single point, which is chosen to be the centroid of the isolator mounting bar surface that attaches to the battery. A diagram of a wire rope isolator model is illustrated in Figure 4-3.

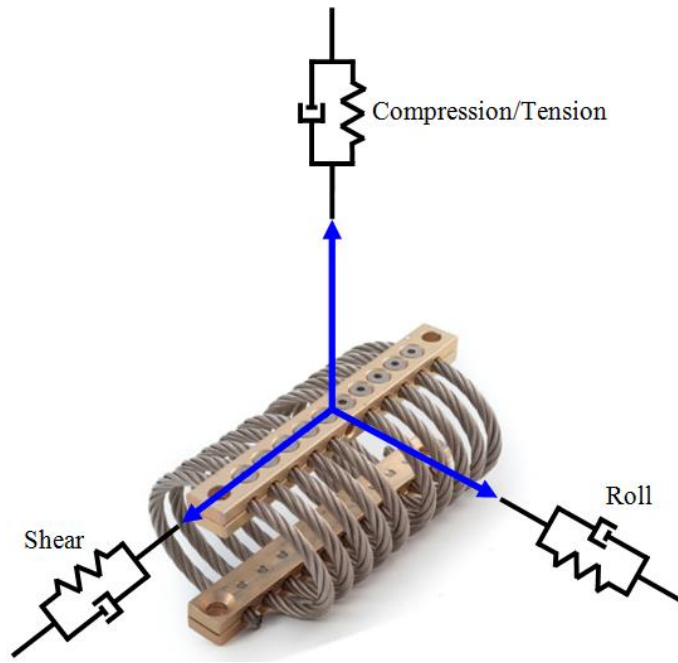


Figure 4-3. Three-axis spring-damper model of a wire rope isolator

### 4.3.1 Spring Properties

The springs shown in Figure 4-3 are modeled as ideal linear springs. They do not contain mass or inertia, do not dissipate any energy, and apply force that is directly proportional to deflection. All stiffness information for these springs presented in this thesis is obtained from IDC. As discussed in Section 3.1.2, there are two linear spring constants included in the IDC's catalog for each deflection mode corresponding to vibration,  $k_v$ , and shock,  $k_s$ , applications. Either  $k_v$  or  $k_s$  is initially selected and used throughout the duration of a simulation; this is determined on which base excitation is applied (Chapter 6 details base acceleration inputs). Furthermore, it is published that the stiffness values for the shear and roll modes are identical [32]. Hence, both lateral deflection modes use the same vibration and shock spring constants, labeled  $k_{v, shear}$  and  $k_{s, shear}$ , respectively. Lastly, the vertical deflection mode utilizes two different

spring constants corresponding to compression and tension. The combination of these spring behaviors yields six independent spring constants for a given wire rope isolator. Table 4-2 summarizes these stiffness values.

Table 4-2. Linear spring constants of wire rope isolator

		Type of Tray Input	
		Vibration	Shock
Deflection Mode	Compression	$k_{v,comp}$	$k_{s,comp}$
	Tension	$k_{v,tension}$	$k_{s,tension}$
	Shear	$k_{v,shear}$	$k_{s,shear}$
	Roll		

The force exerted by a spring is a linear relationship with deflection  $D$ , scaled by constant stiffness  $k$  as shown in Equation 4-4. Figure 4-4 shows the relationship between applied force and deflection for each spring constant in Table 4-2.

$$F_{spring} = -kD \quad (4-4)$$

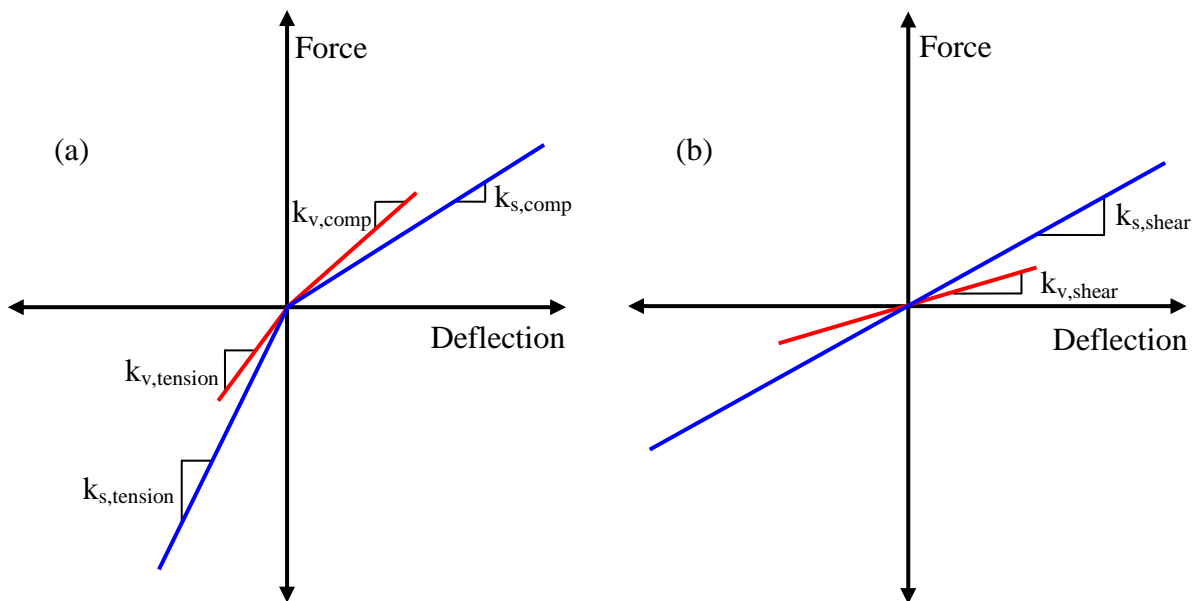


Figure 4-4. Vertical (a) and lateral (b) spring force-deflection curves

### 4.3.2 Damping Properties

The dampers shown in Figure 4-3 exhibit viscous energy dissipation. Damping force varies linearly with velocity. To approximate the nonlinear damping behavior plotted in Figure 3-6, two different damping ratios are incorporated, corresponding to different deflection ranges of an isolator. A conservative damping ratio of 5% is applied to the first half of the deflection range of an isolator (0-50% of its maximum deflection), because smaller deflections induce minor amounts of cable rubbing, i.e. frictional losses. The latter half of deflection uses 15% damping since the contact areas exhibiting cable rubbing are greater with larger deflections. These two damping ratios are used for all deflection modes and all isolator sizes. Figure 4-5 shows the damping ratio as a piecewise function of isolator deflection.

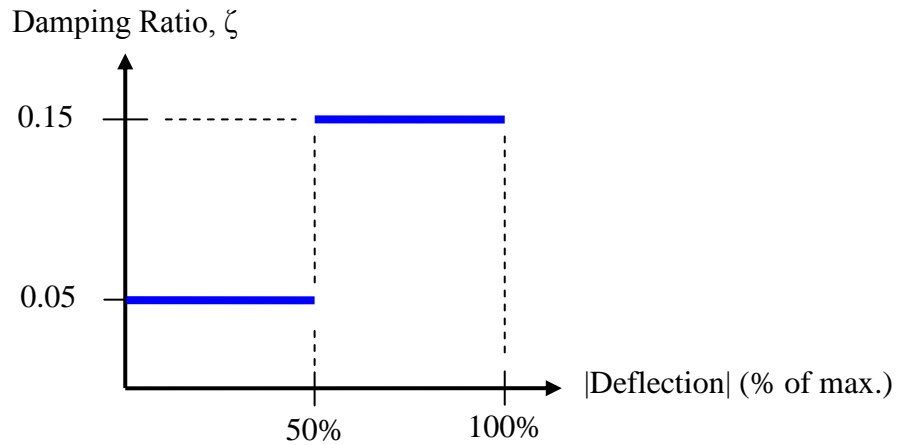


Figure 4-5. Piecewise damping ratio approximation

The force exerted by a viscous damper is directly proportional to velocity  $V$ , scaled by a constant damping coefficient  $c$ , as shown in Equation 4-5.

$$F_{damper} = -cV \quad (4-5)$$

The damping coefficient is calculated using Equation 4-6

$$c_{r,mode} = 2\zeta\sqrt{m_{iso}k_{r,mode}} \quad (4-6)$$

where  $r = v$  (vibration) or  $s$  (shock) and  $mode = comp, tension, \text{ or } shear$ . Mass  $m_{iso}$  is the normal load statically supported by an isolator,  $k_{r,mode}$  is one of the six spring constants listed in Table 4-2, and damping ratio  $\zeta$  is obtained from Figure 4-5.

This relationship indicates that damping force depends on both the magnitude and mode of deflection of an isolator. Therefore, for vibration analysis, there are three possible damping coefficients ( $c_{v,comp}$ ,  $c_{v,tension}$ , and  $c_{v,shear}$  corresponding to  $\zeta=0.05$ ), and for shock analysis, there are six possible damping coefficients ( $c_{s,comp}$ ,  $c_{s,tension}$ , and  $c_{s,shear}$  corresponding to both  $\zeta=0.05$  and  $\zeta=0.15$ ). Here it is noted that an isolator does not deflect more than 50% for vibration analysis. The linear force-velocity curves for different damping coefficients are illustrated in Figure 4-6.

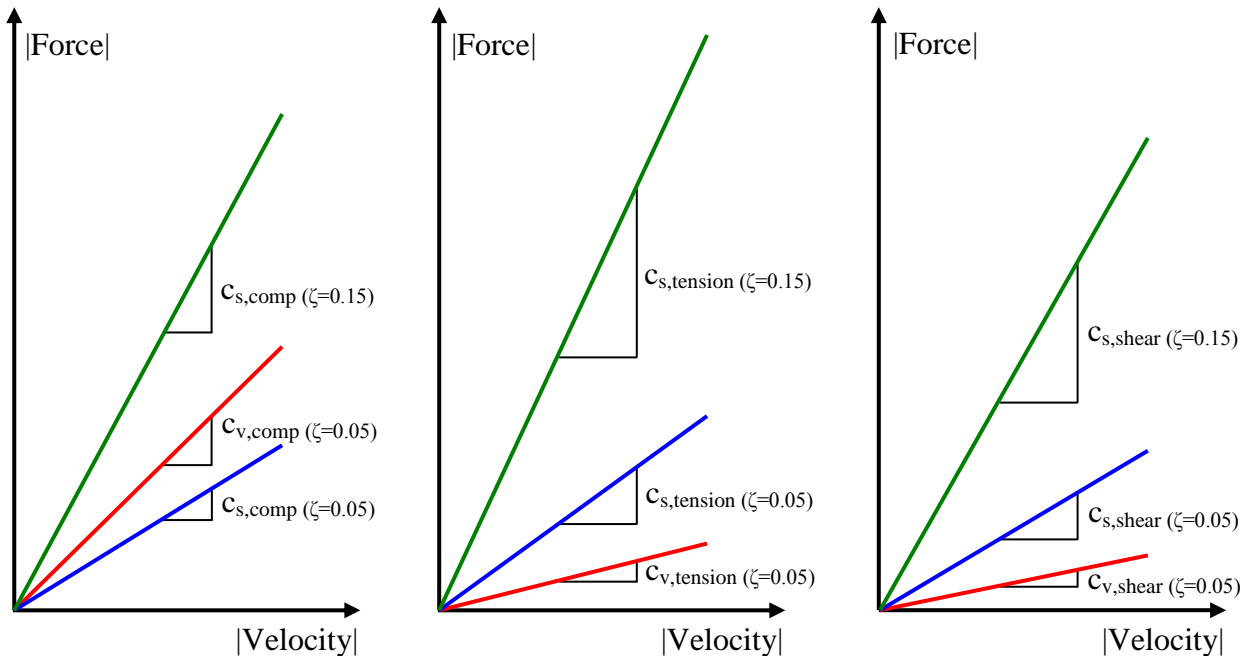


Figure 4-6. Force-velocity curves using the nine possible damping coefficients

## 4.4 Modeling of Bump Stops

The bump stops comprise one or more silicone sheets and can be installed on each of the six inner tray walls. The compressive forces exerted by a real sheet of silicone are distributed over the entirety of the area acted upon. Simplifying these distributed loads as a single resultant force is not an accurate modeling method because it neglects effects from battery rotation. Rather, a more sophisticated approach is to subdivide a sheet's total area into smaller, uniform area elements. One point load is subsequently assigned to each of these discretized areas. Sections 5.1 and 5.5 detail this discretization procedure which better elaborates on the locations of the assigned bump stop forces.

The point loads are modeled as parallel connections of a spring and damper replicating the compressive stiffness and damping characteristics of the material. It is assumed that a sheet has no mass or inertia, and that all shear effects are negligible. Figure 4-7 shows the model representation of a silicone sheet discretized into four elements.

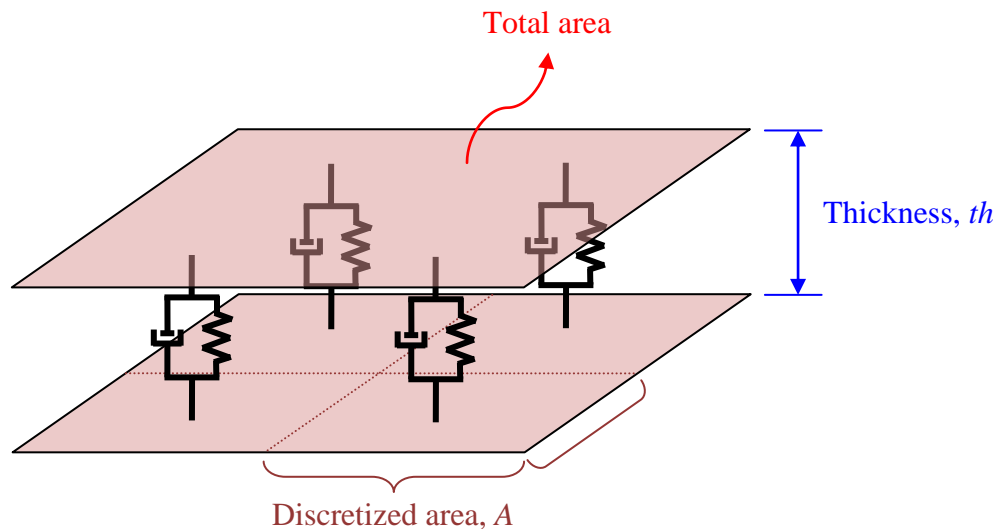


Figure 4-7. Spring-damper model of a silicone sheet's compression

#### 4.4.1 Spring Properties

All silicone stiffness properties used in this work are obtained from BISCO online catalogs. Since the force-deflection curves for silicone materials, particularly silicone foams, are highly nonlinear, the silicone springs are not modeled as having constant spring constants. Instead, the force-deflection relationships are directly obtained from Figure 3-8 and Figure 3-9. Polynomial curve fits (with coefficients  $C_1$ ,  $C_2$ ,  $C_3$ ) are performed to calculate force (over area) as a function of compression percentage  $\% comp$ . The total spring force is then calculated using Equation 4-7.

$$F_{spring} = A * [C_1(\% comp) + C_2(\% comp)^2 + C_3(\% comp)^3] \quad (4-7)$$

#### 4.4.2 Damping Properties

The dampers, on the other hand, are modeled as linear viscous dampers. Damping ratios of some BISCO silicone foam samples have previously been estimated using ball drop tests (as calculated using logarithmic decay equations detailed in [38]). The resulting damping ratios ranged from 0.04 to 0.12. In this work, a damping ratio of 0.05 is applied to all silicone foams and solids. Equations 4-8 through 4-11 are used to calculate the viscous damping force.

Mass  $m_{bump}$  represents the proportion of the battery's mass  $m$  that acts on a single spring/damper element of silicone. This relates to the number of elements that a bump stop for a particular battery face is discretized into.

$$m_{bump} = \frac{m}{\# elements} \quad (4-8)$$

As illustrated in Figure 4-8, a linear spring constant  $k_{lin}$  is gathered by estimating the slope of the force-deflection curve in the semi-linear region. This region applies from approximately 0% to 40% compression.

$$k_{lin} = \frac{f(40\%) - f(0\%) A}{0.40 - 0} \frac{A}{th} \quad (4-9)$$

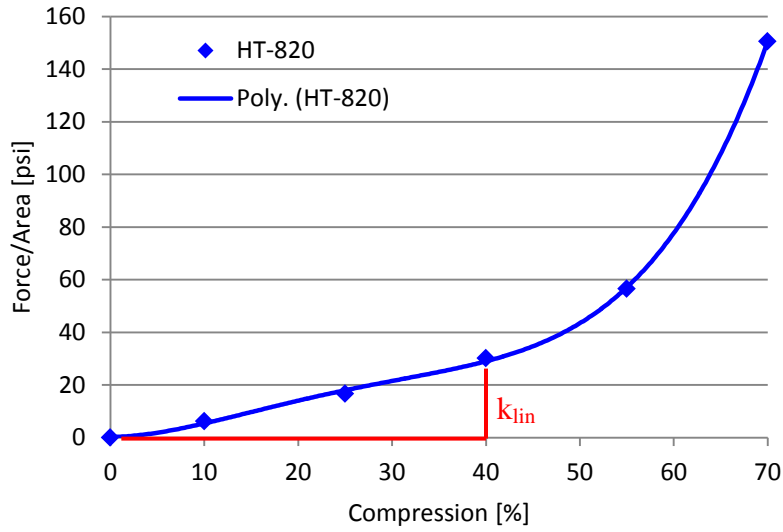


Figure 4-8.  $k_{lin}$  estimation for HT-820 silicone foam

The damping coefficient is calculated as

$$c = 2\zeta \sqrt{m_{bump} k_{lin}} \quad (4-10)$$

using  $\zeta = 0.05$ .

The force exerted by a bump stop damper is directly proportional to velocity  $V$ , scaled by the damping coefficient  $c$ .

$$F_{damper} = -cV \quad (4-11)$$

### 4.4.3 Stacking

The silicone sheets sold by BISCO are only available in specific thicknesses. Most of the solid rubber pads have a maximum thickness of 0.25". If the performance of a thicker sheet is desired, multiple silicone sheets can be stacked together, as shown in Figures 4-9 and 4-10. Assuming the stack contains a uniform material and area, the effective thickness and compression of the stack is  $n$  times greater than that of each individual sheet, where  $n$  equals the total number of sheets. This relationship is exhibited in Equations 4-12 and 4-13.

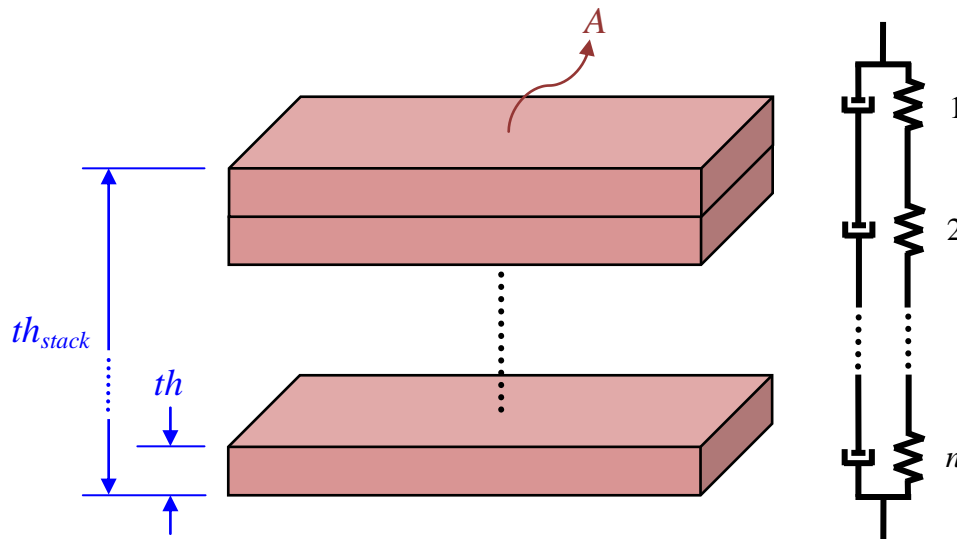


Figure 4-9. Stacking of silicone sheets

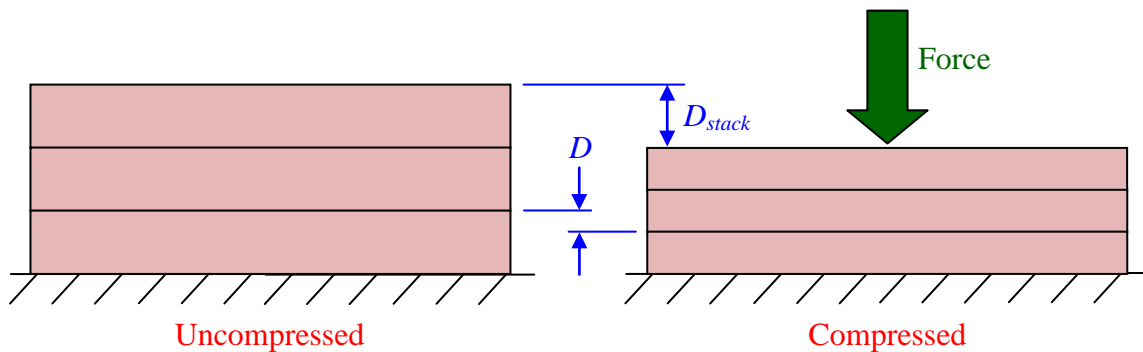


Figure 4-10. Displacement of silicone sheets within stack

The relationship between stack thickness/deflection and individual sheet thickness/deflection is given by

$$th_{stack} = n * th \quad (4-12)$$

$$D_{stack} = n * D \quad (4-13)$$

where for  $n = 1, 2, 3 \dots$

The compression percentage of a single sheet given deflection is calculated by

$$\% \text{ compression} = \frac{D}{th} * 100 = \frac{D_{stack}}{th_{stack}} * 100 \quad (4-14)$$

The same total force is exerted by each sheet in a stack the springs and dampers are connected in series. Spring force is calculated using the polynomial fittings using the force-deflection data, and substituting the compression percentage of either a single sheet or the stack as a whole (they are equal from Equation 4-14). The damping coefficient  $c_{stack}$  decreases by a factor  $n$  as compared to an individual sheet. Equations 4-15 through 4-17 show the effective spring and damper forces of a silicone stack.

$$F_{spring,stack} = A * f(\% \text{ compression}_{stack}) = A * f(\% \text{ compression}) \quad (4-15)$$

$$c_{stack} = \frac{c}{n} \quad (4-16)$$

$$F_{damper,stack} = -c_{stack}V \quad (4-17)$$

## 4.5 Static Equilibrium

Now that the modeling procedure for each component has been presented, the entire system model can be constructed. The wire rope isolators/bump stops placed in the clearance between the battery and tray are substituted with their corresponding spring and damper models, as shown in Figure 4-11. The springs and dampers representing isolators act in three orthogonal axes (shear, roll, and compression/tension) while the bump stop springs and dampers are unidirectional.

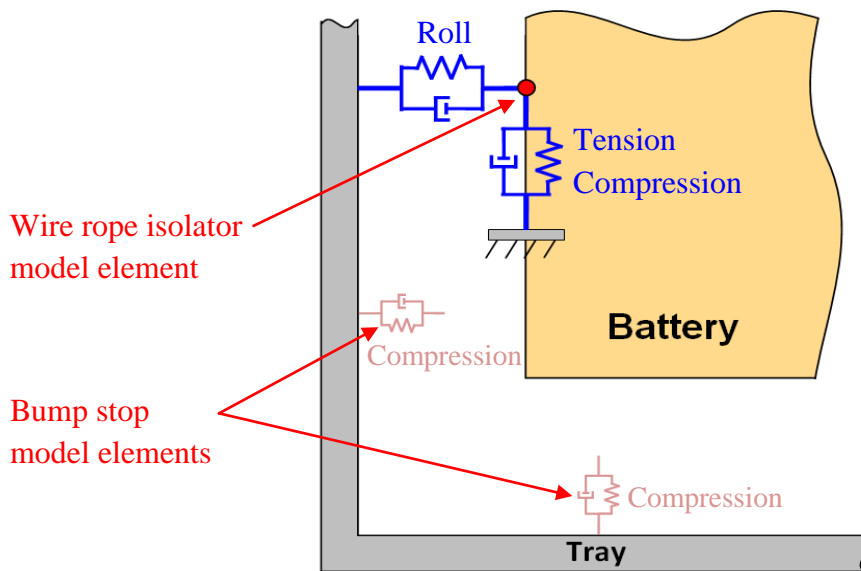


Figure 4-11. Model representation of system packaging

Static equilibrium of this system describes the state when the battery experiences no acceleration with respect to the tray. This indicates that the net sums of all external forces acting on the battery are zero. At equilibrium, the battery and tray coordinate systems are both coincident and aligned. The displacements of the wire rope and bump stops model elements are defined as perturbations from their equilibrium deflections; thus, the suspension does not impose any force on the battery whatsoever at equilibrium.

It is important to note that static equilibrium does NOT indicate that the actual wire rope isolators are not deflecting. In fact, the isolators do exhibit some static deflection, where the small amount of compression produces a combined upwards force equaling the weight of the battery. The system model calculates battery responses about the static equilibrium position, so the battery's weight is not included in the governing equations.

Figures 4-12 and 4-13 show the static equilibrium positions for the stacked and single battery configurations, respectively. The dampers shown in Figure 4-11 are not included here to avoid clutter, but each spring does have an associated damper acting in parallel.

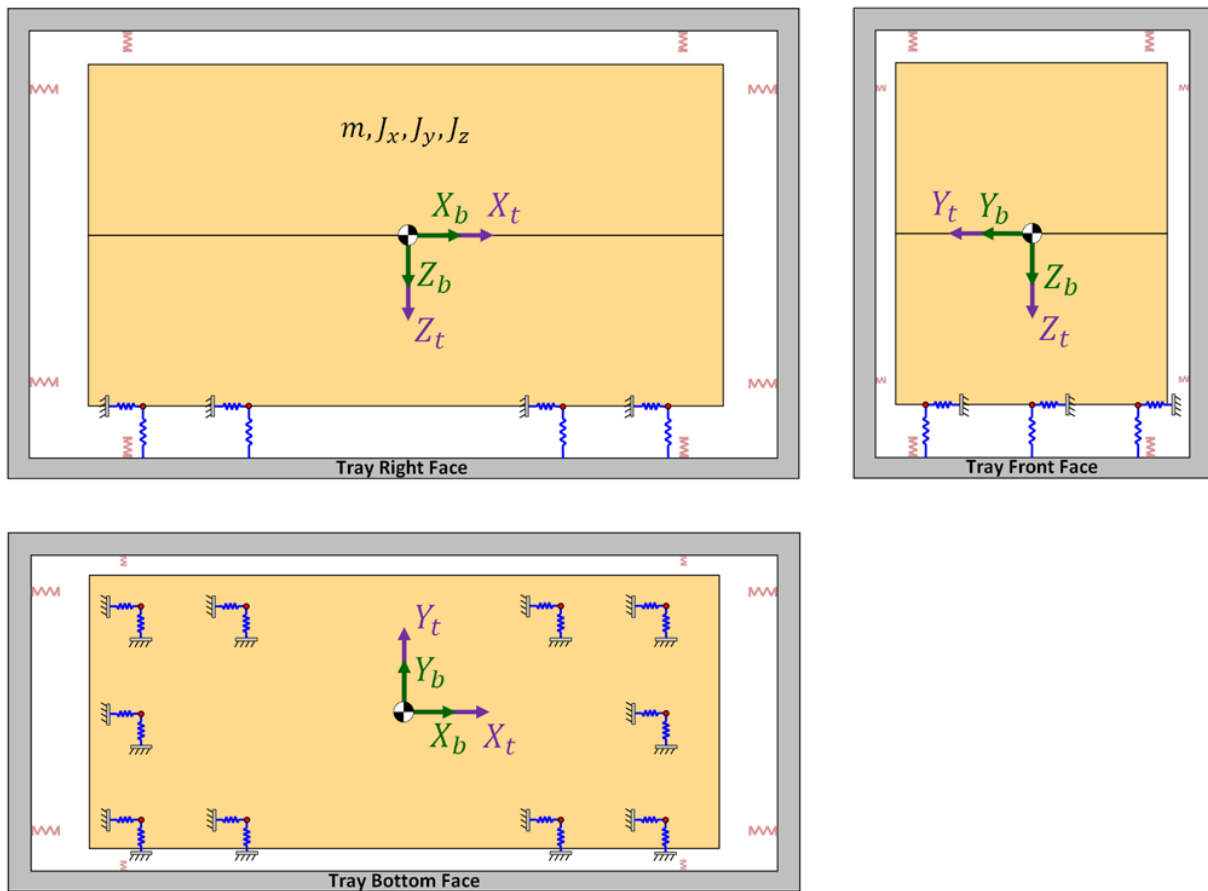


Figure 4-12. System model diagram of stacked battery configuration

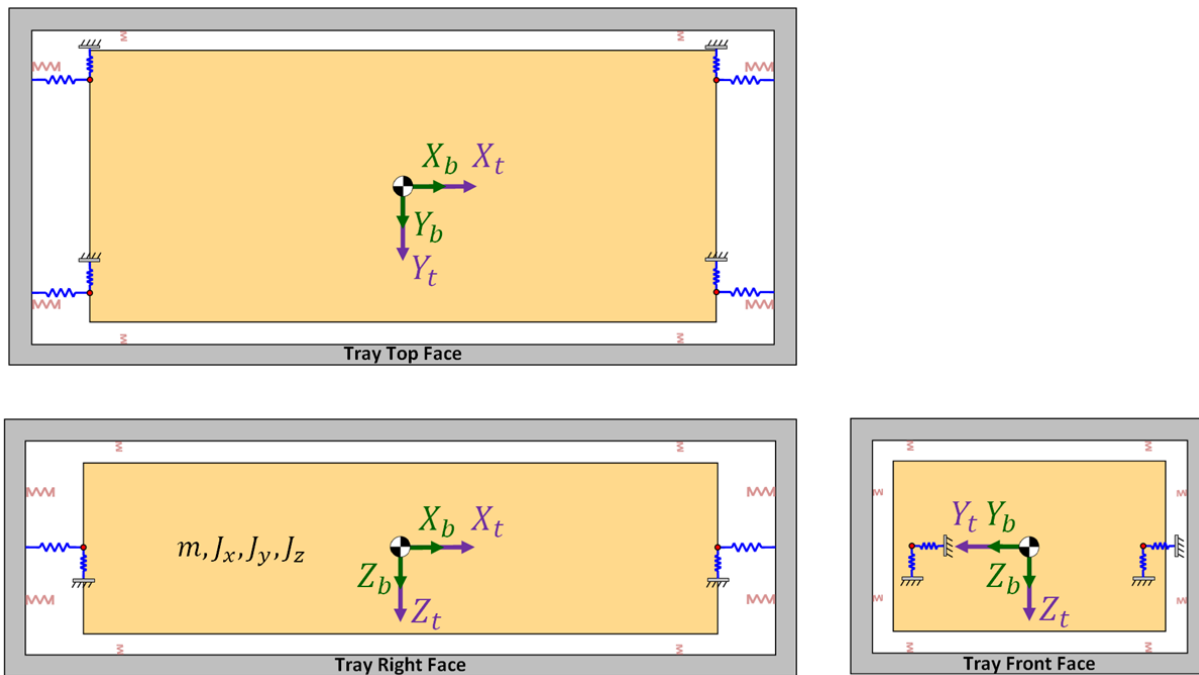


Figure 4-13. System model diagram of single battery configuration

## 4.6 Mathematical Structure

The dynamics of these systems are characterized by differential equations using inputs, states, and outputs. Inputs are the external sources of mechanical energy that drive the system's motion, which in this case are the translational accelerations of the tray. The states of the battery are the set of information that fully describe the battery's condition at a given instant in time. The state variables are the battery's relative positions and velocities with respect to the tray. Lastly, the outputs of this system are chosen to be the accelerations of the battery's CG. For the remainder of this thesis, the term *absolute* refers to motion with respect to a global or inertial reference frame, and *relative* refers to motion with respect to the carrier tray.

### 4.6.1 Inputs

The inputs to the system are the translational accelerations of the tray coordinate system, measured in the inertial reference frame. These accelerations are denoted in Equation 4-18. Because the tray is rigidly connected to the vehicle by the lifting arms, and the fact that the tray has a tremendous amount of rotational inertia, it is assumed that any rotational acceleration of the tray is negligible. These assumptions effectively model the tray inputs as base accelerations for the battery.

$$u = \begin{bmatrix} \ddot{X}_t \\ \ddot{Y}_t \\ \ddot{Z}_t \end{bmatrix} \quad (4-18)$$

Figure 4-14 shows the input accelerations applied to the origin of the tray coordinate system. These inertial accelerations are obtained using accelerometers from vehicle testing. Chapter 6 defines three distinct data sets used as inputs for the simulations.

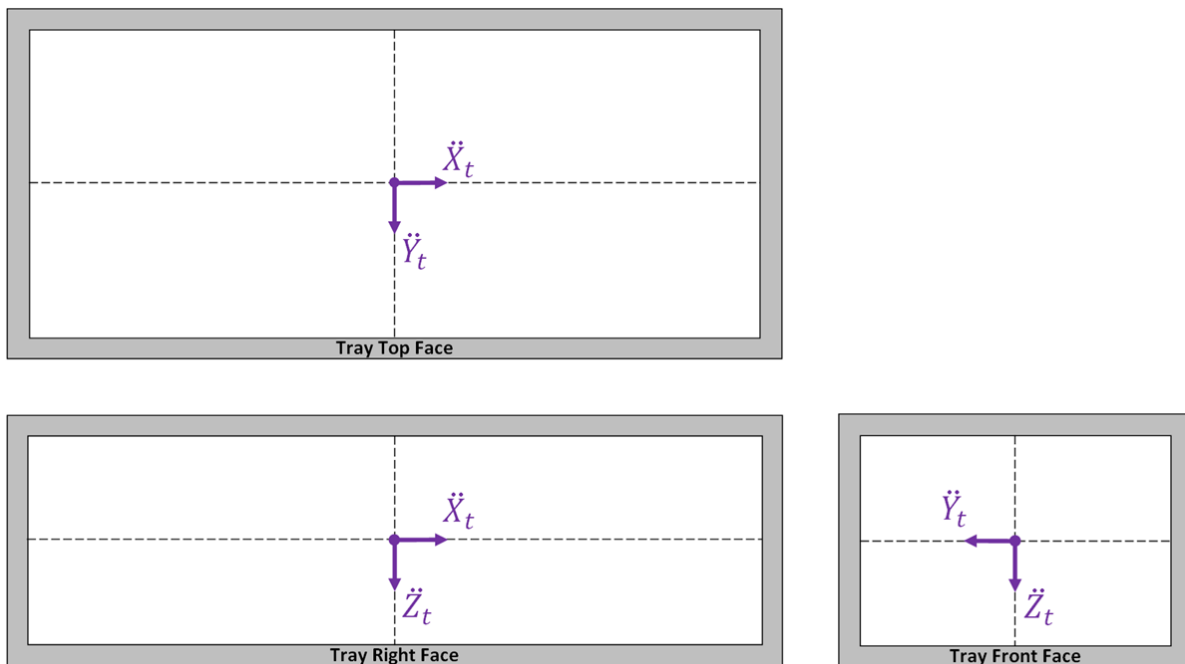


Figure 4-14. Translational accelerations of tray coordinate system

## 4.6.2 States

The dynamics of the battery are fully characterized by the state variables. The state variables describe the battery's relative positions and velocities with respect to the tray. Since the battery's motion is not constrained by the tray in any direction, it has six DOF: three translational and three rotational. The translational displacements  $D_X$ ,  $D_Y$ , and  $D_Z$  are defined with respect to the origin of the tray coordinate system. The relative rotational displacements of the battery are designated by three Euler angles,  $\phi$ ,  $\theta$ , and  $\psi$ . These Euler angles prescribe a 3-2-1 coordinate transformation about the  $Z$ ,  $Y$ , and  $X$  axes, respectively, to align the battery and tray coordinate systems. Figure 4-15 shows the six displacement state variables.

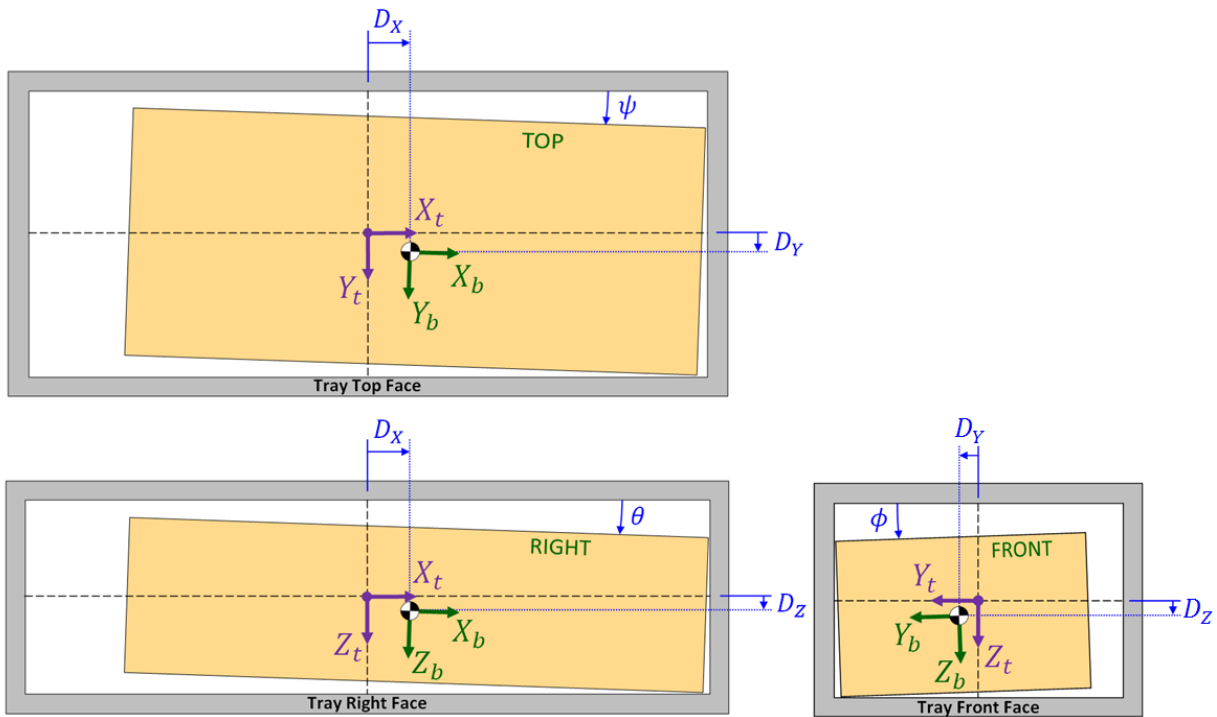


Figure 4-15. Six state variables defining relative battery position

Six state variables are also needed to define the battery's relative velocity with respect to the tray. The three translational velocities are calculated by taking the first derivative with respect to time of the displacement variables  $D_X$ ,  $D_Y$ , and  $D_Z$ . The rotational velocities of the battery are defined as  $p$ ,  $q$ , and  $r$ , where they represent the body-fixed angular rates about the  $X_b$ ,  $Y_b$ , and  $Z_b$  axes, respectively.

Compiling all twelve state variables yields the state vector  $x$ , given as

$$x = \begin{bmatrix} D_X \\ D_Y \\ D_Z \\ \phi \\ \theta \\ \psi \\ \dot{D}_X \\ \dot{D}_Y \\ \dot{D}_Z \\ p \\ q \\ r \end{bmatrix} \quad (4-19)$$

The rate of change of the state vector is given in Equation 4-20 by taking the time derivative of Equation 4-19.

$$\dot{x} = \begin{bmatrix} \dot{D}_X \\ \dot{D}_Y \\ \dot{D}_Z \\ \dot{\phi} \\ \dot{\theta} \\ \dot{\psi} \\ \ddot{D}_X \\ \ddot{D}_Y \\ \ddot{D}_Z \\ \dot{p} \\ \dot{q} \\ \dot{r} \end{bmatrix} \quad (4-20)$$

Using Equations 4-18, 4-19, and 4-20, the battery's response can be simulated by numerically integrating forward in time. Chapter 5 discusses how to derive the equations of motion needed to populate Equation 4-20.

### 4.6.3 Outputs

The outputs of the system are chosen to be the absolute accelerations of the battery. These are expressed as the column vector  $y$  in Equation 4-21.

$$y = \begin{bmatrix} \ddot{X}_b \\ \ddot{Y}_b \\ \ddot{Z}_b \end{bmatrix} \quad (4-21)$$

The absolute accelerations are aligned with the axes of the battery coordinate system, as shown in Figure 4-16. Using this coordinate system, the simulated accelerations can be validated by fixing accelerometers to the battery, which record the inertial accelerations in battery coordinates. Deriving these accelerations from the inputs and states is discussed at the end of Chapter 5.

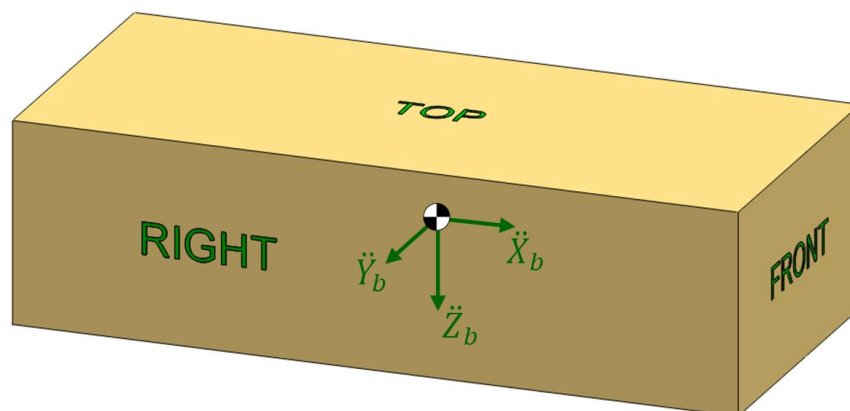


Figure 4-16. Output accelerations of the battery

## **CHAPTER 5**

### **EQUATIONS OF MOTION**

This chapter derives the ordinary differential equations that govern the rate of change of the state vector presented in Chapter 4. These are calculated via Newtonian dynamic equilibrium, which incorporates the magnitudes and locations of all forces acting on the battery that are induced by wire rope isolators and bump stops. The variables associated with linear acceleration are obtained by summing the forces in the three axes of the tray coordinate system. The rotational acceleration state variables are determined by summing the moments about the battery using body-fixed coordinates. This chapter details how the locations of the forces are designated, how the magnitudes of the wire rope isolator and bump stop forces are calculated, and finally, how these forces are combined together to generate the equations of motion needed for simulation.

#### **5.1 Battery Surface Discretization**

The first step in deriving equations of motion is to define locations on the battery surfaces where wire rope isolators and bump stop materials are attached. It is only at these attachment locations where forces can be applied to the battery. In reality, there are an infinite number of points where a material's force can act on a battery surface; however, to expedite any changes between designs, it is beneficial to have predefined locations where materials can be installed, i.e. where wire rope and bump stop forces can act on the battery.

The process of defining these “attachment point locations” is referred to as discretization. Each of the six battery surfaces are discretized into a “matrix” of points. Figure 5-1 shows a three-dimensional view of the battery and the attachment points on the front, right, and top faces.

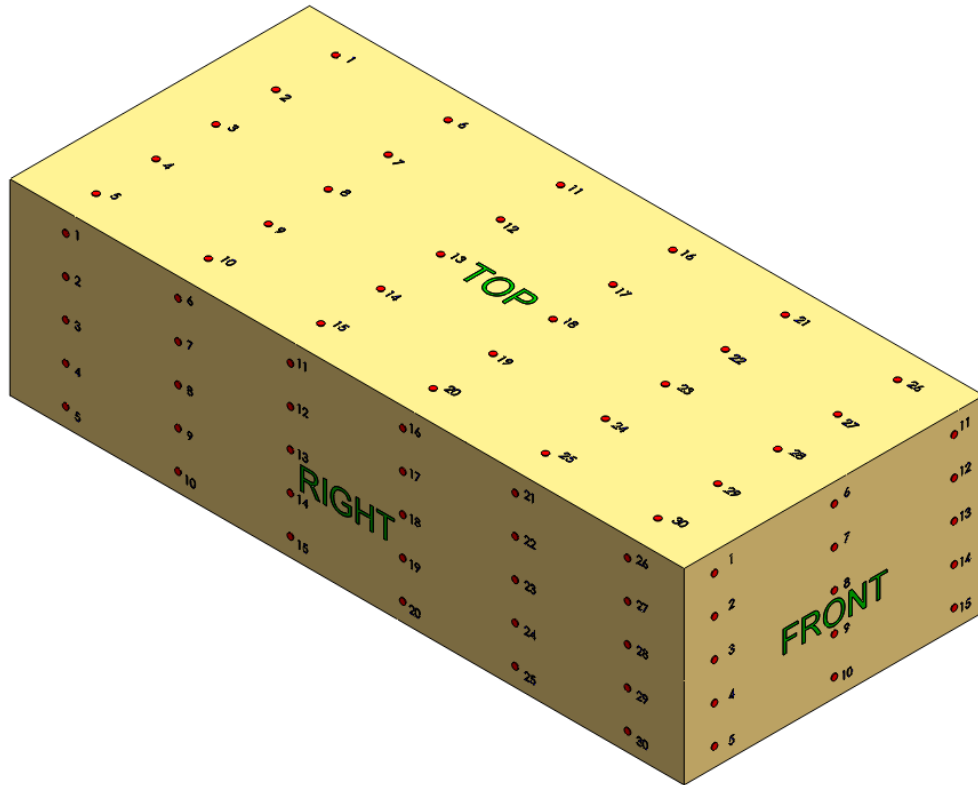


Figure 5-1. Discretization of battery faces with attachment point matrices

Figures 5-2 through 5-4 show the attachment points for all six faces of the battery. The top, bottom, left and right faces have thirty points each, arranged in matrices containing five rows and six columns. The front and back battery faces are each discretized into matrices containing five rows and three columns, equating to fifteen attachment points. Three dimensions,  $a$ ,  $d$ , and  $f$ , fully define the locations of all of the attachment points. These dimensions are related to the overall dimensions of the battery by Equations 5-1, 5-2, and 5-3.

$$a = \frac{5}{12} L_x \quad (5-1)$$

$$d = \frac{2}{5} L_z \quad (5-2)$$

$$f = \frac{2}{5} L_y \quad (5-3)$$

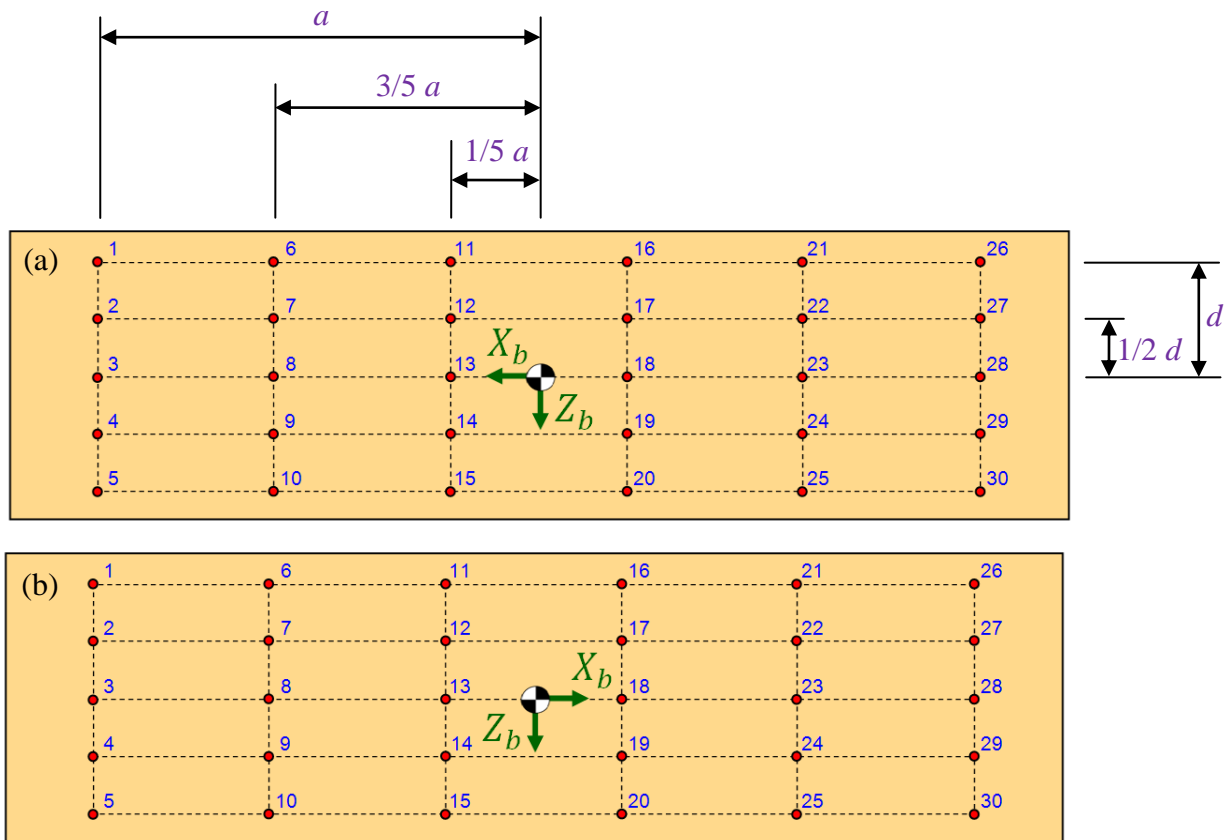


Figure 5-2. Left face (a) and right face (b) attachment points

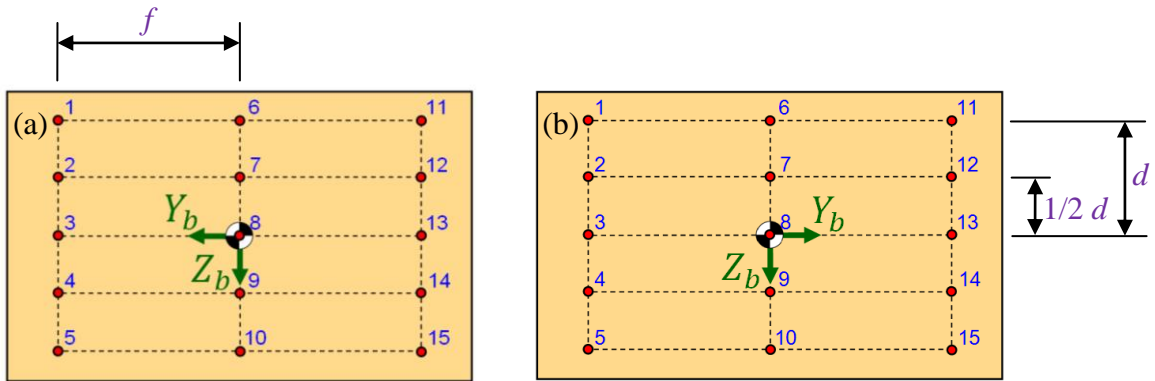


Figure 5-3. Front face (a) and back face (b) attachment points

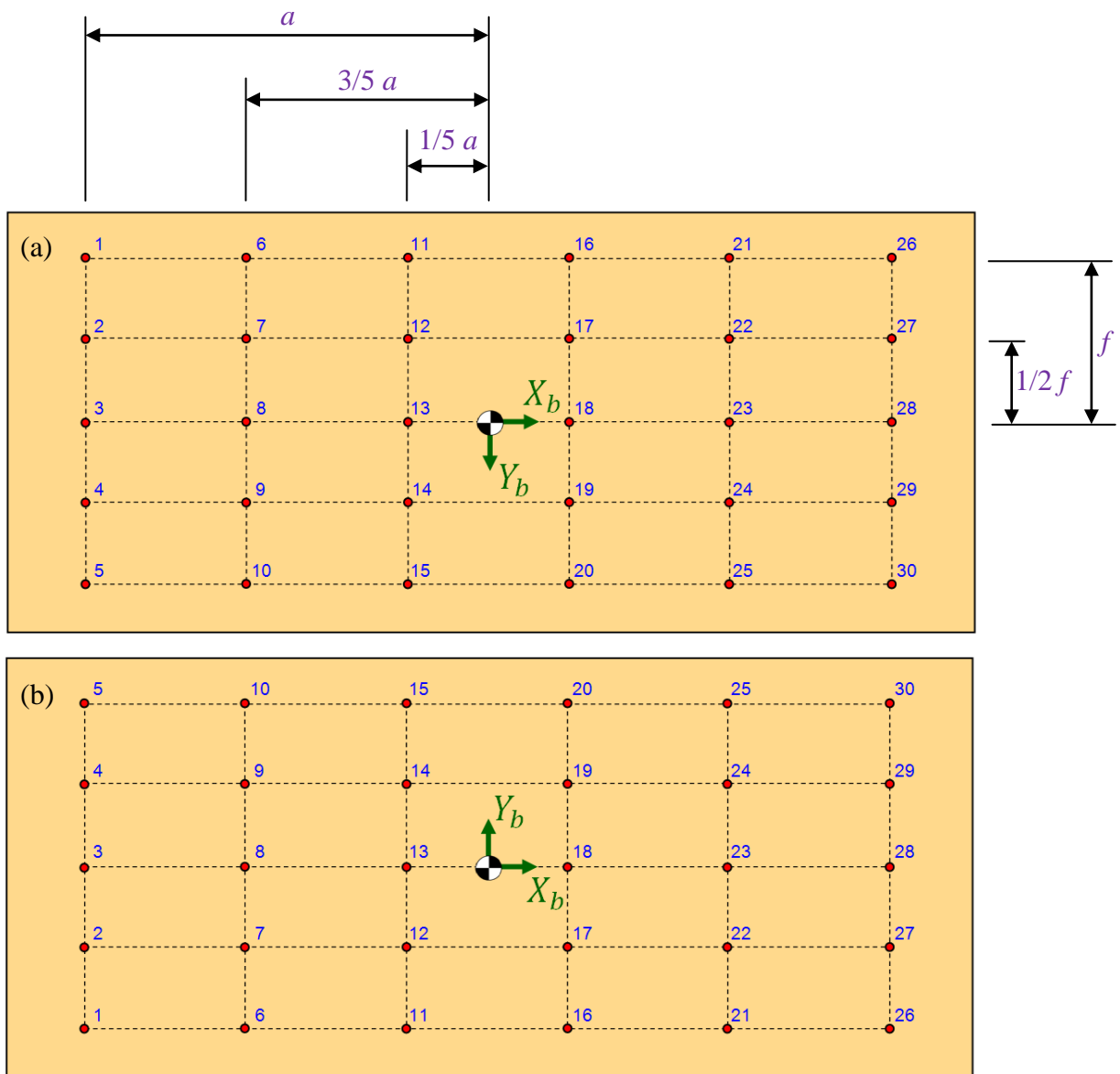


Figure 5-4. Top face (a) and bottom face (b) attachment points

Using these diagrams, the location of every attachment point on all six faces of the battery can be defined in battery coordinates in terms of  $a, d, f, L_x, L_y,$  and  $L_z$ . For example, the fifteen attachment points on the front face (arranged in a five row by three column matrix) have battery-fixed coordinates of

$$x_{Front} = \frac{L_x}{2} \begin{bmatrix} 1 & 1 & 1 \\ 1 & 1 & 1 \\ 1 & 1 & 1 \\ 1 & 1 & 1 \\ 1 & 1 & 1 \end{bmatrix}_b \quad (5-4)$$

$$y_{Front} = \begin{bmatrix} f & 0 & -f \\ f & 0 & -f \end{bmatrix}_b \quad (5-5)$$

$$z_{Front} = \begin{bmatrix} -d & -d & -d \\ d & d & d \\ -\frac{d}{2} & -\frac{d}{2} & -\frac{d}{2} \\ 0 & 0 & 0 \\ \frac{d}{2} & \frac{d}{2} & \frac{d}{2} \\ d & d & d \end{bmatrix}_b \quad (5-6)$$

where the subscript  $b$  denotes the battery coordinate system.

As a second example, the location of attachment point ‘9’ on the right battery face has the following battery coordinates

$$\begin{bmatrix} x_{Right,9} \\ y_{Right,9} \\ z_{Right,9} \end{bmatrix}_b = \begin{bmatrix} -\frac{3}{5}a \\ \frac{1}{2}L_y \\ \frac{1}{2}d \end{bmatrix}_b \quad (5-7)$$

Specifying the battery coordinates of these attachment points is essential for calculating the displacements of the points in tray coordinates, which are needed in order to determine isolator/bump stop forces.

## 5.2 Battery Surface Displacements

As detailed in Chapter 4, wire rope isolator and bump stop forces are dependent on the displacements and velocities of the modeled springs and dampers. The displacements of the springs are equal to the displacements (in tray coordinates) of the points that they attach to. Since the locations of the attachment points are defined in battery coordinates, it is first necessary to present a coordinate transformation matrix to convert between the two coordinate systems. Using the Euler angles  $\phi$ ,  $\theta$ , and  $\psi$ , two-dimensional rotation matrices about the Z-Y-X axes are shown in Equations 5-8 through 5-10.

$$R_Z = \begin{bmatrix} \cos \psi & -\sin \psi & 0 \\ \sin \psi & \cos \psi & 0 \\ 0 & 0 & 1 \end{bmatrix} \quad (5-8)$$

$$R_Y = \begin{bmatrix} \cos \theta & 0 & \sin \theta \\ 0 & 1 & 0 \\ -\sin \theta & 0 & \cos \theta \end{bmatrix} \quad (5-9)$$

$$R_X = \begin{bmatrix} 1 & 0 & 0 \\ 0 & \cos \phi & -\sin \phi \\ 0 & \sin \phi & \cos \phi \end{bmatrix} \quad (5-10)$$

The complete three-dimensional transformation matrix is calculated by sequential matrix multiplication of the two-dimensional coordinate transformations

$$R_Z R_Y R_X = \begin{bmatrix} c_\theta c_\psi & s_\phi s_\theta c_\psi - c_\phi s_\psi & c_\phi s_\theta c_\psi + s_\phi s_\psi \\ c_\theta s_\psi & s_\phi s_\theta s_\psi + c_\phi c_\psi & c_\phi s_\theta s_\psi - c_\phi s_\psi \\ -s_\theta & s_\phi c_\theta & c_\phi c_\theta \end{bmatrix} \quad (5-11)$$

where the shorthand  $c_\beta = \cos \beta$  and  $s_\beta = \sin \beta$  is used.

Because the battery is enclosed inside the tray on all six sides with tight clearance gaps, the rotation angles of the battery with respect to the tray are physically constrained. The maximum rotation about any axis is quite small, so it is acceptable to apply small angle approximations for all three Euler angles. This assumption indicates  $\cos \beta = 1$  and  $\sin \beta = \beta$ .

The complete rotation matrix using small angle approximations is given by

$$(R_Z R_Y R_X)_{small} = \begin{bmatrix} 1 & \phi\theta - \psi & \theta + \phi\psi \\ \psi & \phi\theta\psi + 1 & \theta\psi - \phi \\ -\theta & \phi & 1 \end{bmatrix} \quad (5-12)$$

Small angle approximations are used throughout the remainder of this work. The subscript *small* is dropped for convenience.

Using this coordinate transformation matrix and the displacements between the battery and tray coordinate system origins, any point defined in the battery coordinates can be described in tray coordinates. The location of a point  $i$  defined in tray coordinates at any instant in time is given by

$$\begin{bmatrix} X_i \\ Y_i \\ Z_i \end{bmatrix}_t = \begin{bmatrix} D_x \\ D_y \\ D_z \end{bmatrix}_t + R_Z R_Y R_X \begin{bmatrix} x_i \\ y_i \\ z_i \end{bmatrix}_b \quad (5-13)$$

where the subscripts  $t$  and  $b$  denote tray and battery coordinates, respectively.

At equilibrium, the battery and tray coordinate systems are coincident and aligned, thus the position of point  $i$  is identical in both coordinates, as shown in Equation 5-14.

$$\begin{bmatrix} x_i \\ y_i \\ z_i \end{bmatrix}_b = \begin{bmatrix} X_i \\ Y_i \\ Z_i \end{bmatrix}_{t,eq} \quad (5-14)$$

The deflection of point  $i$  in tray coordinates, relative to its equilibrium position, is calculated as

$$\begin{bmatrix} D_{X,i} \\ D_{Y,i} \\ D_{Z,i} \end{bmatrix}_t = \begin{bmatrix} X_i \\ Y_i \\ Z_i \end{bmatrix}_t - \begin{bmatrix} X_i \\ Y_i \\ Z_i \end{bmatrix}_{t,eq} \quad (5-15)$$

Figure 5-5 graphically shows the deflection of point  $i$ . The red point is point  $i$  fixed to the battery when the battery is in static equilibrium (denoted by the dashed red outline). After the battery CG undergoes translations  $D_Y$  and  $D_Z$  and rotation  $\phi$ , the new positions of the battery and point  $i$  are shown in cyan. The battery-fixed coordinates of  $i$  are identical for both cases, however, the tray coordinates do indeed change. The displacements of point  $i$  in tray coordinates are given by  $D_{Y,i}$  and  $D_{Z,i}$ . Table 5-1 summarizes the coordinate and deflection relationships.

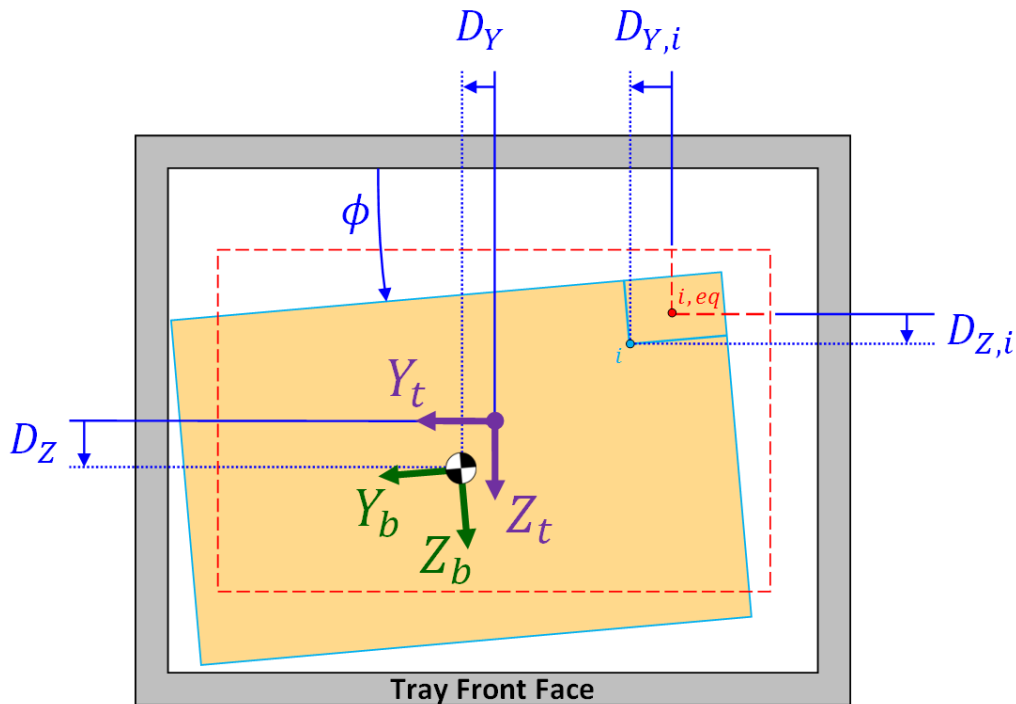


Figure 5-5. Point  $i$  displacements in tray coordinates

Table 5-1. Point  $i$  position in tray and battery coordinate systems

Point	Battery Coordinates	Tray Coordinates	Deflections $(D_{X,i}, D_{Y,i}, D_{Z,i})_t$
Red ●	$(x_i, y_i, z_i)_b$	$(X_i, Y_i, Z_i)_{t,eq} = (x_i, y_i, z_i)_b$	(0,0,0)
Cyan ●		$(X_i, Y_i, Z_i)_t$	$(X_i, Y_i, Z_i)_t - (X_i, Y_i, Z_i)_{t,eq}$

Using this procedure, the displacements of every attachment point on all six battery faces can be determined in the  $X_t$ ,  $Y_t$ , and  $Z_t$  directions. It is these deflections that are used to calculate isolator and bump stop spring forces, as discussed in Sections 5.5 and 5.6.

### 5.3 Battery Surface Velocities

The velocities at each attachment point need to be calculated as well in order to determine the wire rope and bump stop damping forces. This is done by differentiating Equation 5-15 with respect to time.

$$\frac{d}{dt} \begin{bmatrix} D_{X,i} \\ D_{Y,i} \\ D_{Z,i} \end{bmatrix}_t = \frac{d}{dt} \left\{ \begin{bmatrix} D_X \\ D_Y \\ D_Z \end{bmatrix}_t + R_Z R_Y R_X \begin{bmatrix} x_i \\ y_i \\ z_i \end{bmatrix}_b - \begin{bmatrix} X_i \\ Y_i \\ Z_i \end{bmatrix}_{t,eq} \right\} \quad (5-16)$$

The time derivatives of the relative displacements of the battery CG are given in Equation 5-17. These relative velocities are included in the state vector, and do not need to be directly calculated.

$$\frac{d}{dt} \begin{bmatrix} D_X \\ D_Y \\ D_Z \end{bmatrix}_t = \begin{bmatrix} \dot{D}_X \\ \dot{D}_Y \\ \dot{D}_Z \end{bmatrix}_t \quad (5-17)$$

The time rate of change of the rotation matrix is given by

$$\frac{d}{dt}(R_Z R_Y R_X) = \begin{bmatrix} 0 & \phi\dot{\theta} + \theta\dot{\phi} - \dot{\psi} & \dot{\theta} + \phi\dot{\psi} + \psi\dot{\phi} \\ \dot{\psi} & \phi\psi\dot{\theta} + \phi\theta\dot{\psi} + \theta\psi\dot{\phi} & \theta\dot{\psi} + \psi\dot{\theta} - \dot{\phi} \\ -\dot{\theta} & \dot{\phi} & 0 \end{bmatrix} \quad (5-18)$$

Lastly, the time derivative of the position of point  $i$  in battery coordinates is zero. By definition, the battery coordinates of any point fixed to the battery always remain constant.

$$\frac{d}{dt} \begin{bmatrix} X_i \\ Y_i \\ Z_i \end{bmatrix}_{t,eq} = \frac{d}{dt} \begin{bmatrix} x_i \\ y_i \\ z_i \end{bmatrix}_b = 0 \quad (5-19)$$

Therefore, the velocity of point  $i$  in the tray coordinate system can be determined by substituting Equations 5-17 through 5-19 into Equation 5-16, as displayed in Equation 5-20.

$$\begin{bmatrix} \dot{D}_{i,x} \\ \dot{D}_{i,y} \\ \dot{D}_{i,z} \end{bmatrix}_t = \begin{bmatrix} \dot{D}_X \\ \dot{D}_Y \\ \dot{D}_Z \end{bmatrix}_t + \begin{bmatrix} 0 & \phi\dot{\theta} + \theta\dot{\phi} - \dot{\psi} & \dot{\theta} + \phi\dot{\psi} + \psi\dot{\phi} \\ \dot{\psi} & \phi\psi\dot{\theta} + \phi\theta\dot{\psi} + \theta\psi\dot{\phi} & \theta\dot{\psi} + \psi\dot{\theta} - \dot{\phi} \\ -\dot{\theta} & \dot{\phi} & 0 \end{bmatrix} \begin{bmatrix} x_i \\ y_i \\ z_i \end{bmatrix}_b \quad (5-20)$$

The time derivatives of the Euler angles are dependent on both the Euler angles and angular rates in the battery coordinate system, as shown in Equations 5-21 through 5-23. These incorporate small angle approximations into the aircraft attitude equations derived in *Aircraft Control and Simulation* by Stevens [39]. Note that due to inertial coupling, the time derivatives of the Euler angles are not simply equal to the battery's angular rates.

$$\dot{\phi} = p + q\phi\theta + r\theta \quad (5-21)$$

$$\dot{\theta} = q - r\phi \quad (5-22)$$

$$\dot{\psi} = q\phi + r \quad (5-23)$$

Using the state vector and Equations 5-21 through 5-23, the velocities of any attachment point in tray coordinates can be solved for via Equation 5-20.

## 5.4 Wire Rope Isolator Forces

This section illustrates how forces produced by wire rope isolators are characterized. As stated in Section 4.3, wire rope isolators are modeled as springs and dampers connected in parallel, acting in three orthogonal axes. The magnitudes of the forces exerted by these elements are dependent on both the displacement and velocity of the attachment point that defines where on the battery surface an isolator is attached. Not only is the location of an isolator important, but also its orientation with respect to the battery since the spring constants are different for the various deflection modes. Therefore, it is important to first identify the alignment of the isolators that connect to the battery surfaces.

In the stacked battery configuration, wire rope isolators are installed underneath the bottom battery face. The centroid of each isolator's mounting bar is coincident with an attachment point. There are a total of thirty attachment points on the bottom face and thus thirty possible locations to install wire rope isolators. Each isolator is aligned such that and the shear axis is parallel with the  $X_b$  battery axis, the roll axis is parallel with  $Y_b$ , and the compression axis is aligned with the  $+Z_b$  axis. The deflection axes are labeled in Figure 5-6 and Figure 5-7 illustrates how isolators are attached to the bottom face of the battery stack.

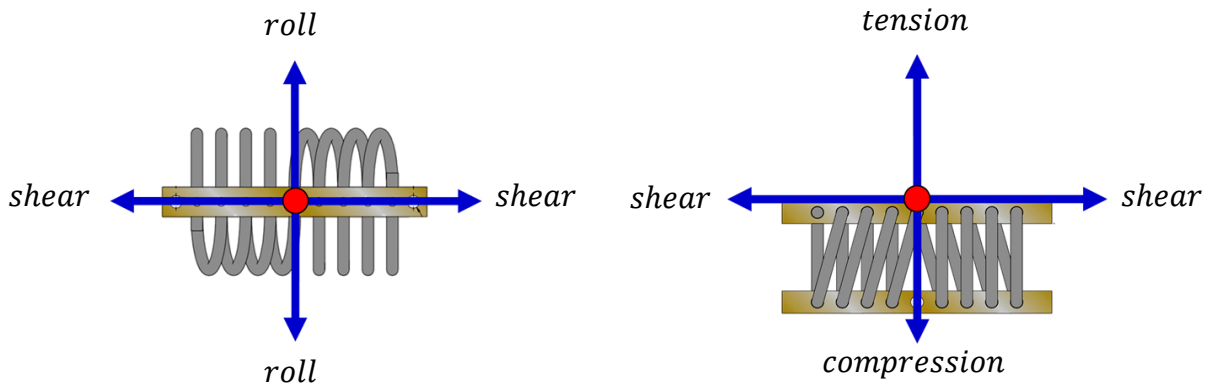


Figure 5-6. Deflection axes of wire rope isolator

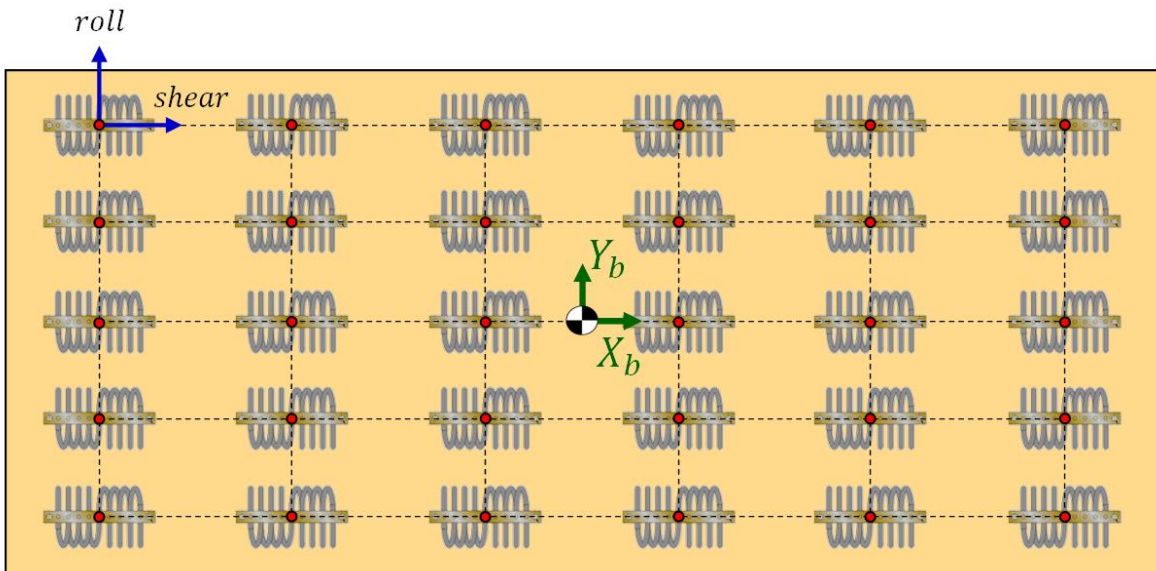


Figure 5-7. Alignment of wire rope isolators installed underneath battery stack

In the single battery configuration, wire rope isolators are installed on the front and back battery faces. The centroid of each isolator's mounting bar is coincident with an attachment point. There are a total of fifteen attachment points on the front face and thus fifteen possible locations to install wire rope isolators. Each isolator is aligned such that the roll axis is parallel with the  $X_b$  battery axis, the shear axis is parallel with  $Y_b$ , and the compression axis is parallel with the  $+Z_b$  axis. Figure 5-8 illustrates how isolators are attached to the front face of a single

battery. The exact same alignment is used for the back face as well. It is important to note that due to the variety of isolator sizes, attaching all fifteen isolators simultaneously may not be able to dimensionally feasible.

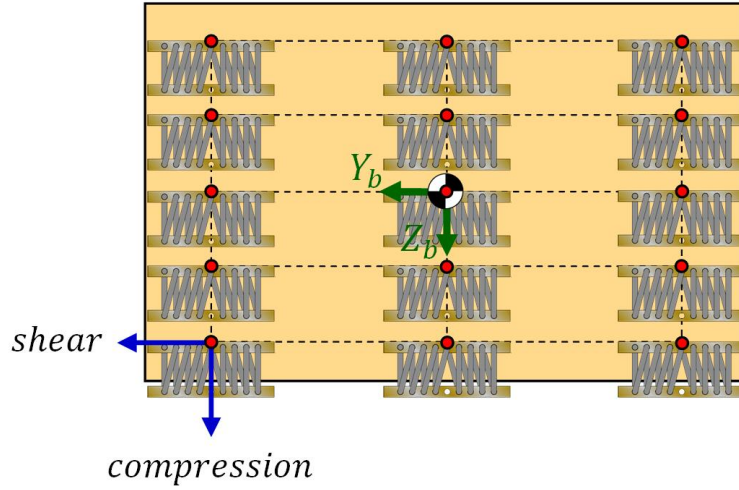


Figure 5-8. Alignment of wire rope isolators installed on front face of single battery

Because the shear and roll spring constants are equal, the force equations for both assembly configurations are in fact identical. The spring forces for the three axes of an isolator are linear functions of the deflection of the isolator's attachment point  $i$ . These forces at point  $i$  are calculated as

$$F_{spring,X}^{(i)} = -k_{r,shear}D_{X,i} \quad (5-24)$$

$$F_{spring,Y}^{(i)} = -k_{r,shear}D_{Y,i} \quad (5-25)$$

$$F_{spring,Z}^{(i)} = \begin{cases} -k_{r,comp}D_{Z,i} & \text{if } D_{Z,i} \geq -D_{static} \\ -k_{r,tension}D_{Z,i} & \text{if } D_{Z,i} < -D_{static} \end{cases} \quad (5-26)$$

where  $i$  identifies the attachment point and  $r = v$  (vibration) or  $s$  (shock).  $D_{static}$  is the static displacement of the battery caused from its gravitational force. This force imposes an initial compression of every isolator that statically supports the battery. The amount of compression is calculated by

$$D_{static} = \frac{mg}{(\# \text{ isolators})(k_{v,comp})} \quad (5-27)$$

where  $g$  is the gravitational acceleration constant.

Similarly, the damper forces for the three axes of an isolator are linear functions of the velocity of the isolator's attachment point  $i$ . These damping forces at point  $i$  are given as

$$F_{damper,X}^{(i)} = -c_{r, \text{shear}} \dot{D}_{X,i} \quad (5-28)$$

$$F_{damper,Y}^{(i)} = -c_{r, \text{shear}} \dot{D}_{Y,i} \quad (5-29)$$

$$F_{damper,Z}^{(i)} = \begin{cases} -c_{r, \text{comp}} \dot{D}_{Z,i} & \text{if } D_{Z,i} \geq -D_{static} \\ -c_{r, \text{tension}} \dot{D}_{Z,i} & \text{if } D_{Z,i} < -D_{static} \end{cases} \quad (5-30)$$

The total force exerted on the battery surface at point  $i$  by an isolator is equal to the summation of the individual spring and damper forces in each axis, as shown in Equations 5-31 through 5-33.

$$F_{iso,X}^{(i)} = F_{spring,X}^{(i)} + F_{damper,X}^{(i)} \quad (5-31)$$

$$F_{iso,Y}^{(i)} = F_{spring,Y}^{(i)} + F_{damper,Y}^{(i)} \quad (5-32)$$

$$F_{iso,Z}^{(i)} = F_{spring,Z}^{(i)} + F_{damper,Z}^{(i)} \quad (5-33)$$

Based on the sign convention for the displacements and velocities of the attachment points, positive isolator forces act in the same directions as the axes of the tray coordinate system. Note that forces do not necessarily act parallel/perpendicular with the surfaces of the battery. As an example, assume that four isolators are attached to a single battery at attachment points '3' and '13' on the front and back battery faces. The free-body diagram (FBD) of this system is shown in Figure 5-9 and Figure 5-10.

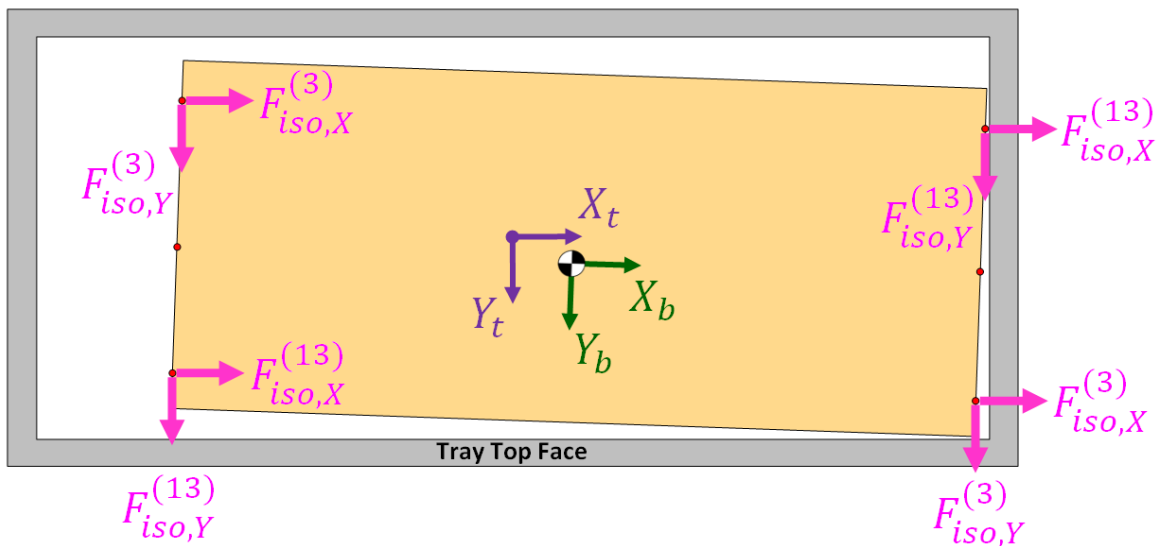


Figure 5-9. Top view of system free body diagram

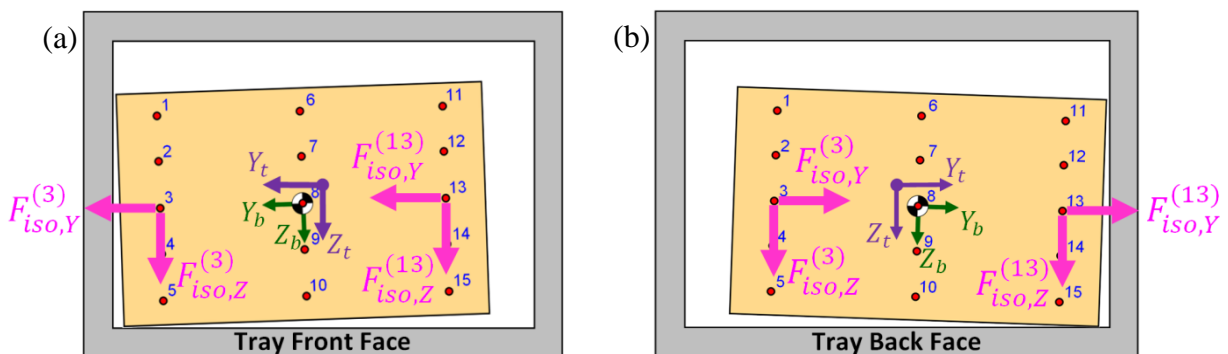


Figure 5-10. Front (a) and back (b) views of system free body diagram

## 5.5 Bump Stop Forces

Bump stop forces are calculated in an identical manner for both battery assembly configurations. A bump stop force, just like an isolator force, acts on the battery at an attachment point on the battery's surface. As discussed in Section 4.4, the total area of the bump stop silicone material may need to be discretized into smaller areas to better account for the distribution of compressive force. Each discretized area  $A$  contains a single spring and damper pair acting in parallel. The point at which the spring and damper forces act is aligned with a corresponding attachment point on the battery surface. Figure 5-11 shows the discretization of a silicone sheet for the top face of the battery, and the alignment of the point forces with attachment points on the top battery surface. To avoid clutter, the dampers are omitted from the diagram.

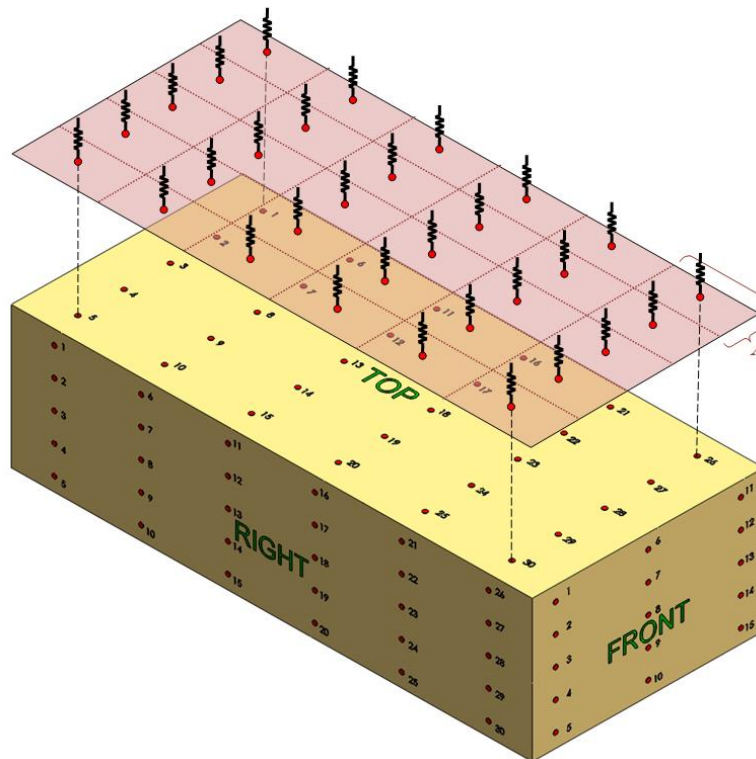


Figure 5-11. Alignment between bump stop discretized areas and battery attachment points

Consequently, the maximum area acting at a single attachment point is

$$A_{max} = \frac{A_{surface}}{\sum i} \quad (5-34)$$

where  $A_{surface}$  is the surface area of the battery face, and  $\sum i$  is the total number of attachment points on that face (either fifteen or thirty). Using the discretized area, the bump stop spring force at attachment point  $i$  on a particular battery face is

$$F_{spring,face}^{(i)} = \begin{cases} 0 & \text{if } D_{dir,i} \leq engage \\ A * f(\% compression_i) & \text{if } D_{dir,i} > engage \end{cases} \quad (5-35)$$

where  $D_{dir,i}$  is the displacement of point  $i$  along the tray axis that is perpendicular to the bump stop area, and  $engage$  is the amount of clearance between the battery and bump stop in static equilibrium (refer to Section 3.4). Compression percentage is calculated as

$$\% compression_i = \frac{D_{dir,i} - engage}{n * th} * 100 \quad (5-36)$$

where  $n$  is the number of silicone sheets stacked together and  $th$  is the individual sheet thickness. Similarly, damping force at attachment point  $i$  on a particular battery face is given by

$$F_{damper,face}^{(i)} = \begin{cases} 0 & \text{if } D_{dir,i} \leq engage \\ \frac{c * \dot{D}_{dir,i}}{n} & \text{if } D_{dir,i} > engage \end{cases} \quad (5-37)$$

where the damping coefficient  $c$  is calculated in Section 4.4.2.

The total force exerted on the battery by the bump stop at attachment point  $i$  is the summation of the corresponding spring and damper forces. The forces acting on the back, left, and top battery faces are given as

$$F_{bump,face}^{(i)} = F_{spring,face}^{(i)} - F_{damper,face}^{(i)} \quad (5-38)$$

The forces on the front, right, and bottom battery faces are

$$F_{bump,face}^{(i)} = -F_{spring,face}^{(i)} + F_{damper,face}^{(i)} \quad (5-39)$$

Unlike the wire rope isolator forces, bump stop forces always act in toward the battery, and can never have negative values. This is because the silicone material cannot pull the battery away from its equilibrium position. Figures 5-12 and 5-13 illustrate the directions of the bump stop forces on all six faces of the battery.

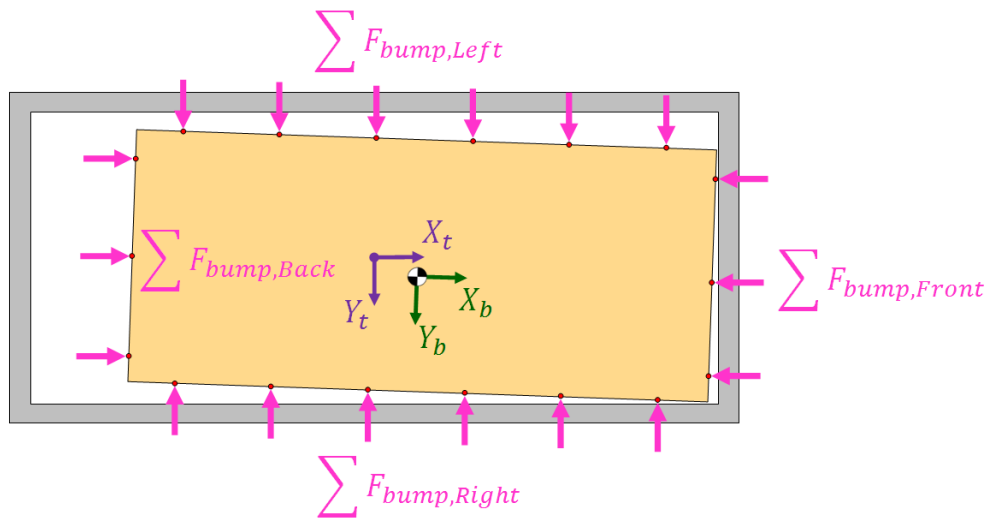


Figure 5-12. Right side view of bump stop compressive forces

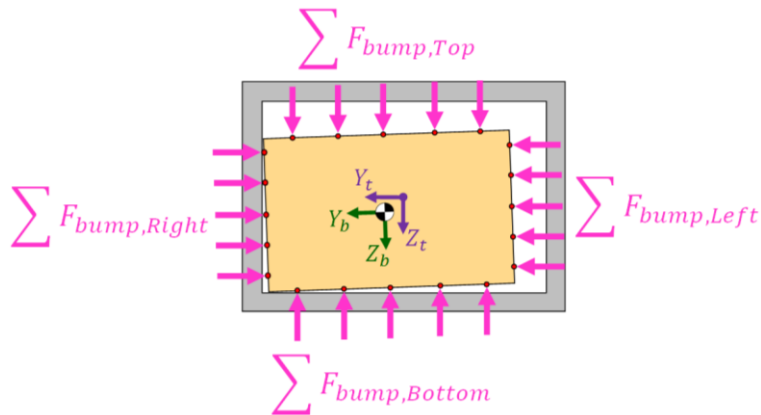


Figure 5-13. Front view of bump stop compressive forces

## 5.6 Equations of Motion

Using the wire rope isolator and bump stop forces previously quantified, the rate of change of the state vector can now be fully defined. The six remaining entities are  $\ddot{D}_X, \ddot{D}_Y, \ddot{D}_Z, \dot{p}, \dot{q},$  and  $\dot{r}$ . To quantize these variables, six equations of motion are derived using Newtonian methods.

The total forces acting on the battery in the  $X_t, Y_t,$  and  $Z_t$  directions are determined by summing wire rope isolator and bump stop forces, given as

$$F_{X,total} = \sum \left( F_{iso,X}^{(i)} - F_{bump,Front}^{(i)} + F_{bump,Back}^{(i)} \right) \quad (5-40)$$

$$F_{Y,total} = \sum \left( F_{iso,Y}^{(i)} + F_{bump,Left}^{(i)} - F_{bump,Right}^{(i)} \right) \quad (5-41)$$

$$F_{Z,total} = \sum \left( F_{iso,Z}^{(i)} + F_{bump,Top}^{(i)} - F_{bump,Bottom}^{(i)} \right) \quad (5-42)$$

The linear accelerations of the battery in the tray coordinate system,  $\ddot{D}_X, \ddot{D}_Y, \ddot{D}_Z,$  are calculated from dynamic equilibrium as

$$\begin{bmatrix} \ddot{D}_X \\ \ddot{D}_Y \\ \ddot{D}_Z \end{bmatrix} = \frac{1}{m} \begin{bmatrix} F_{X,total} \\ F_{Y,total} \\ F_{Z,total} \end{bmatrix} - m \begin{bmatrix} \ddot{X}_t \\ \ddot{Y}_t \\ \ddot{Z}_t \end{bmatrix} \quad (5-43)$$

The time derivative of the roll, pitch, and yaw rates are taken from [39], shown in Equations 5-44 through 5-46. These angular accelerations are functions of the mass moments of inertia, angular rates, and body-fixed moments of the battery,  $\tau_x, \tau_y,$  and  $\tau_z$ .

$$\dot{p} = \frac{J_y - J_z}{J_x} qr + \frac{\tau_x}{J_x} \quad (5-44)$$

$$\dot{q} = \frac{J_z - J_x}{J_y} pr + \frac{\tau_y}{J_y} \quad (5-45)$$

$$\dot{r} = \frac{J_x - J_y}{J_z} pq + \frac{\tau_z}{J_z} \quad (5-46)$$

The body-fixed moments are calculated using magnitudes and locations of isolator and bump stop forces acting on the battery. These forces must first be transformed from tray coordinates to battery coordinates, done via the inverse of the transformation matrix  $R_{ZYX}$ . The moment about the battery caused by the forces acting at attachment point  $i$  is calculated using the cross product between the position vector of  $i$ , in battery coordinates, and the forces (transformed into battery coordinates).

$$\begin{bmatrix} \tau_{x,i} \\ \tau_{y,i} \\ \tau_{z,i} \end{bmatrix}_b = \begin{bmatrix} x_i \\ y_i \\ z_i \end{bmatrix}_b \times \left\{ (R_{ZYX})^{-1} \begin{bmatrix} F_{iso,X}^{(i)} - F_{bump,Front}^{(i)} + F_{bump,Back}^{(i)} \\ F_{iso,Y}^{(i)} + F_{bump,Left}^{(i)} - F_{bump,Right}^{(i)} \\ F_{iso,Z}^{(i)} + F_{bump,Top}^{(i)} - F_{bump,Bottom}^{(i)} \end{bmatrix} \right\} \quad (5-47)$$

It is important to note that since the rotation matrix is orthogonal,  $R_{ZYX}^{-1} = R_{ZYX}^T$ . The body-axis moments calculated in Equation 5-47 can be substituted back into Equations 5-44 through 5-46 to solve for the roll, pitch, and yaw accelerations. All of the equations have now been presented to solve for Equation 4-20 needed for numerical integration.

## 5.7 Output Battery Accelerations

To determine the output accelerations in the  $y$  vector, the relative accelerations of the battery in the tray reference frame  $\ddot{D}_X, \ddot{D}_Y, \ddot{D}_Z$  are first calculated in Equation 5-43. Then, these are added to the base acceleration inputs, shown in Equation 4-17. The resultant yields the inertial accelerations of the battery in tray coordinates, as shown in Equation 5-48. To convert these accelerations from the tray to the battery-fixed coordinate system, a rotation matrix  $R_{ZYX}$  is pre-multiplied. Equation 5-49 gives the final form of the output accelerations of the battery.

$$\begin{bmatrix} \ddot{D}_X \\ \ddot{D}_Y \\ \ddot{D}_Z \end{bmatrix}_t + \begin{bmatrix} \ddot{X}_t \\ \ddot{Y}_t \\ \ddot{Z}_t \end{bmatrix}_t = \begin{bmatrix} \ddot{X}_{batt} \\ \ddot{Y}_{batt} \\ \ddot{Z}_{batt} \end{bmatrix}_t \quad (5-48)$$

$$y = R_{ZYX} \begin{bmatrix} \ddot{X}_{batt} \\ \ddot{Y}_{batt} \\ \ddot{Z}_{batt} \end{bmatrix}_t = \begin{bmatrix} \ddot{X}_b \\ \ddot{Y}_b \\ \ddot{Z}_b \end{bmatrix}_b \quad (5-49)$$

## **CHAPTER 6**

### **BASE ACCELERATION INPUTS**

As mentioned in Chapter 4, the inputs to the system model are base accelerations generated by tray motion. Under the assumption that the tray does not experience any rotation, these accelerations can be characterized via accelerometer data collected during experimental vehicle testing. Selecting what portions of data to use as system inputs is extremely critical because the inputs must represent proper tray behaviors in order for simulation to yield valid results. For example, using inputs that capture accelerations that are too mild or too severe may influence the suspension to be under or overdesigned. Intelligently characterizing the inputs is as paramount as the model dynamics itself.

Three separate sets of sensor data are used for the system inputs. The first, referred to as the vibration input, represents general tray vibration caused when the vehicle drives along bumpy terrain in the underground mines. This data set does not include any shock events, which are defined as accelerations greater than 5 g in magnitude in one or more of the accelerometer axes. Two different data sets are used to characterize base accelerations when the tray is exposed to shock events. One of these shock inputs, called the typical shock input, represents the majority of shock events which occur from modest collisions and bumps. Lastly, a severe shock input profile is used which represents the most substantial shocks that the tray may experience. These three inputs are simulated to produce results needed to design the wire rope isolator and bump stop assemblies, as well as illustrate design tradeoffs. This chapter discusses the accelerometer data collection and then a more in depth description of the three inputs.

## 6.1 Accelerometer Data Collection

A piezoelectric, triaxial accelerometer collected the tray's acceleration during testing. The accelerometer was placed on the left side wall of the tray, as shown in Figure 6-1. The orientations of the accelerometer's axes are inconsistent with the orientation of the tray coordinate system. Thus, a simple transformation is needed to align the corresponding X, Y, and Z axes. This is done using Equation 6-1.

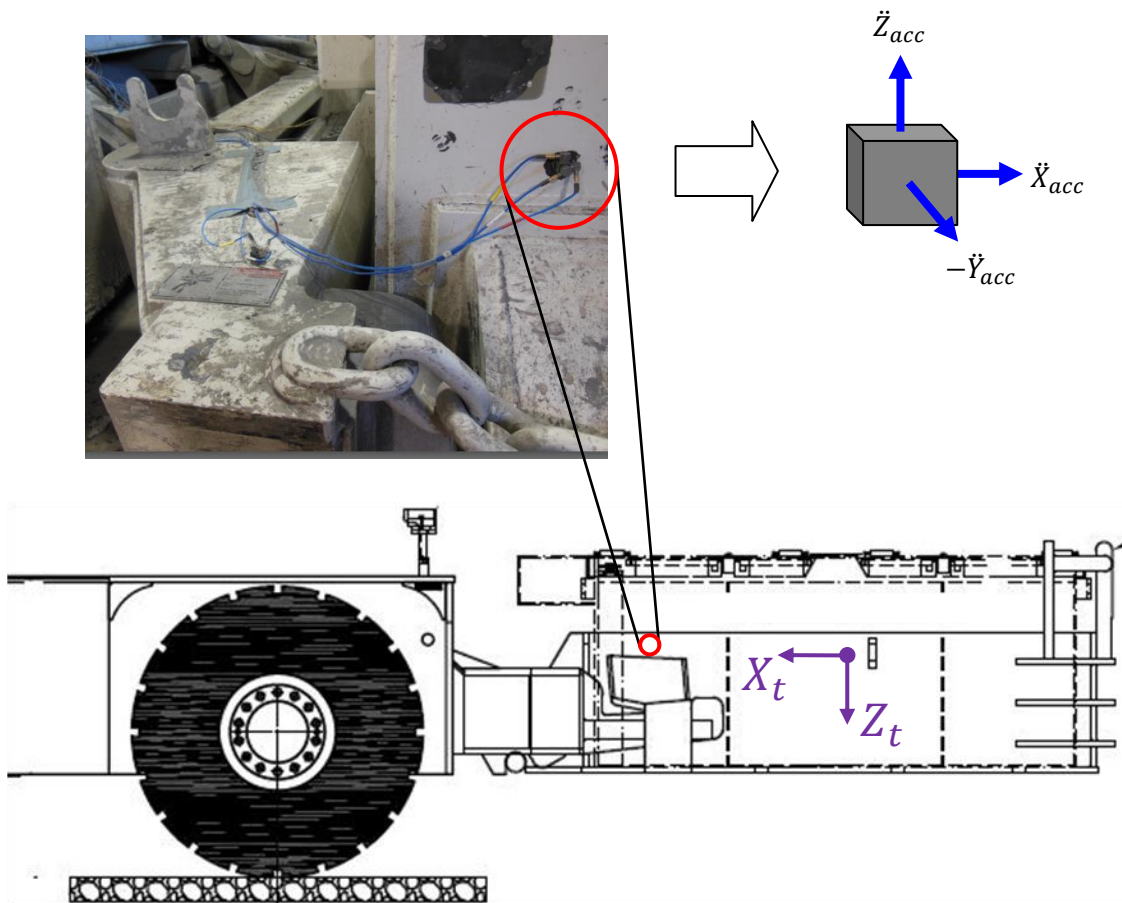


Figure 6-1. Triaxial accelerometer attachment

$$\begin{bmatrix} \ddot{X}_t \\ \ddot{Y}_t \\ \ddot{Z}_t \end{bmatrix} = \begin{bmatrix} -\ddot{X}_{acc} \\ \ddot{Y}_{acc} \\ -\ddot{Z}_{acc} \end{bmatrix} \quad (6-1)$$

GE Mining performed extensive vehicle testing spanning many days. The resulting data was analyzed for shock event occurrences. Shocks in the  $X_{acc}$  and  $Z_{acc}$  directions were sorted by amplitude, as shown in Table 6-1. This table is the premise for classifying typical and severe shock inputs.

Table 6-1. Categorization of recorded shock events

	<b>Run</b>	<b>Acceleration (X &amp; Z)</b>		
	Time (hrs)	> 5g	> 15g	> 30g
Day 13	4.5	9	3	1
Day 14	4.5	14	1	1
Day 15	8.5	12	5	1
Total	17.5	35	9 (26 %)	3 (9%)

## 6.2 Vibration Input

The vibration input corresponds to driving behavior of the mining vehicle in the absence of shock events. Bumpy terrain causes the tray to steadily vibrate on the lifting arms with low acceleration amplitudes. A 60-sec segment of data is selected to represent this tray behavior. Figure 6-2 shows the accelerations in the time domain of all three tray coordinate axes for the vibration input. Figure 6-3 illustrates a fast Fourier transform (FFT) of the acceleration data, which better indicates the signals' prevalent frequencies.

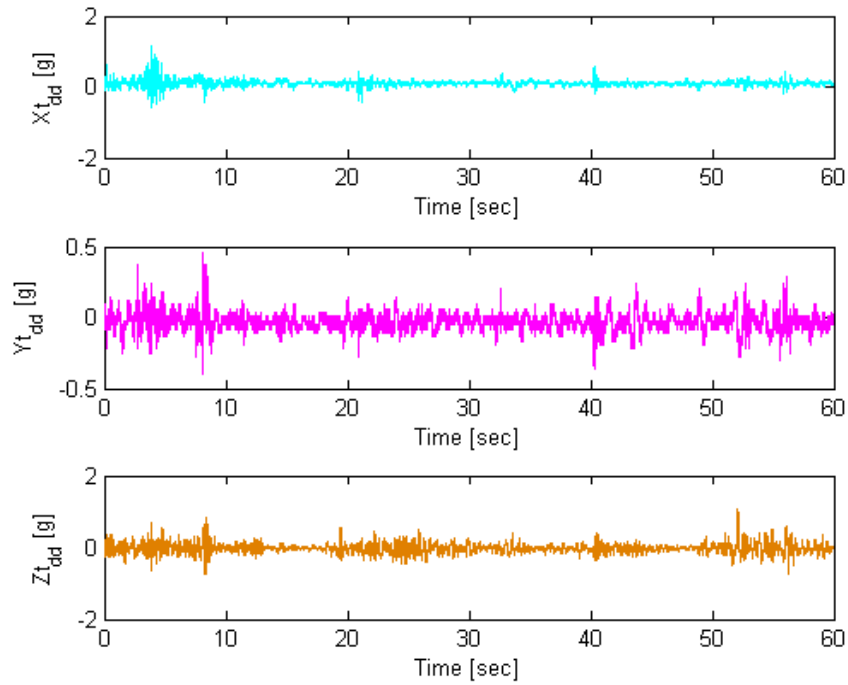


Figure 6-2. Accelerations of tray coordinate axes corresponding to vibration inputs

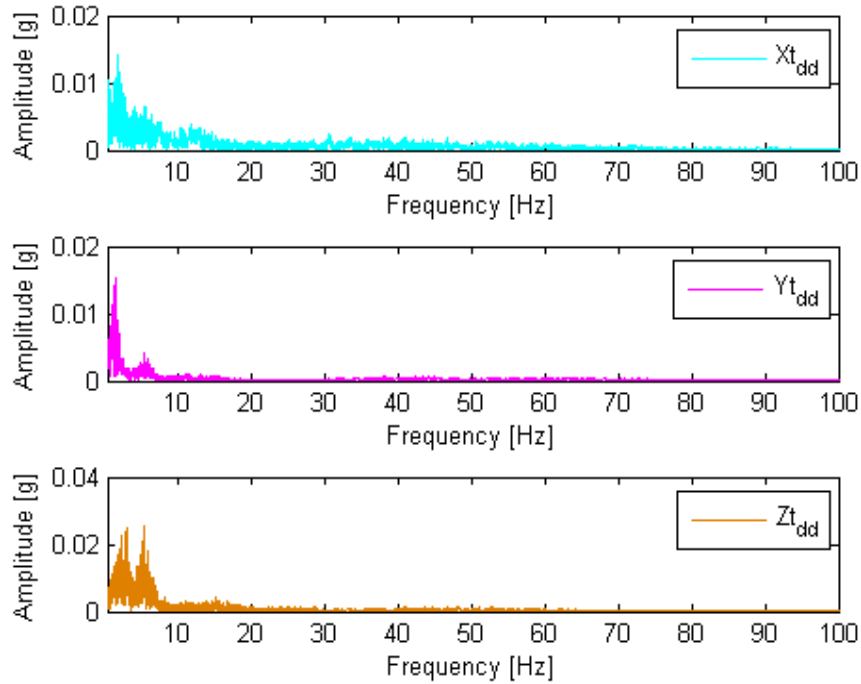


Figure 6-3. Fast Fourier transform of vibration inputs

As is seen in Figure 6-2, the vibration data is very low in amplitude. There are minor spikes in amplitude of approximately 1 g, but in general the magnitudes of the accelerations in all axes are prevalently less than 0.5 g. From Figure 6-3, the vibration input contains prevalent frequencies below 10 Hz. The  $X_t$  and  $Y_t$  axes have peaks at ~1.5 Hz, while the  $Z_t$  axis has two prominent peaks at 2.5 and 5 Hz.

### **6.3 Typical Shock Input**

Typical shock inputs represent accelerometer data that has shock events of commonplace amplitudes. From Table 6-1, 91% of all recorded shocks in the  $X$  and  $Z$  directions have amplitudes below 30 g. Therefore, a typical shock is deemed as having amplitude between 5 and 30 g in either the  $X$  or  $Z$  directions.

To form the typical shock input data sequence, two distinct shock events are compiled together. The first event is a 2-sec data segment that encompasses amplitudes on the lower portion of the 5 to 30 g range. The second event is also 2 sec in duration and has amplitudes at the upper limit of the typical shock range. Sufficient time is allotted in the middle of the data sequence to avoid any coupling between the two events. Figure 6-4 shows the 4-sec typical shock input profile.

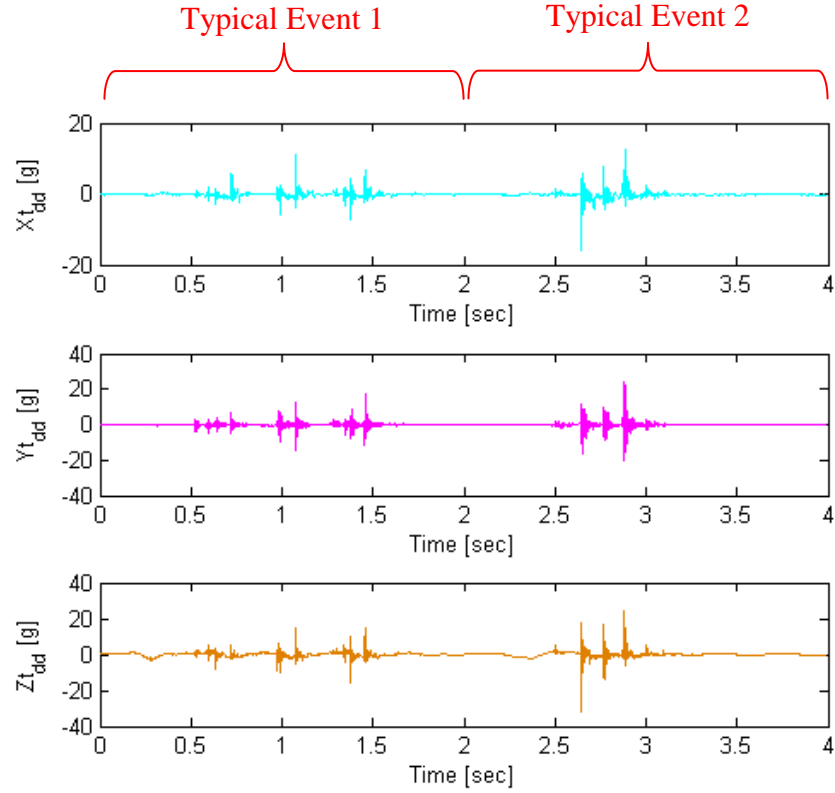


Figure 6-4. Typical shock input profile

## 6.4 Severe Shock Input

The severe shock input is used to simulate extreme, infrequent mining occurrences that yield substantial accelerations of the tray. This input is intended to ensure that the suspension design can sustain a severe event without damaging the battery or the suspension itself. The severe shock input profile contains two independent shock events where the  $Z_t$  axis has acceleration magnitudes greater than 50 g. To prevent coupling between the two, 0.5 sec of null acceleration is incorporated after the first event. The total duration of the data segment is 2.5 sec, as shown in Figure 6-5.

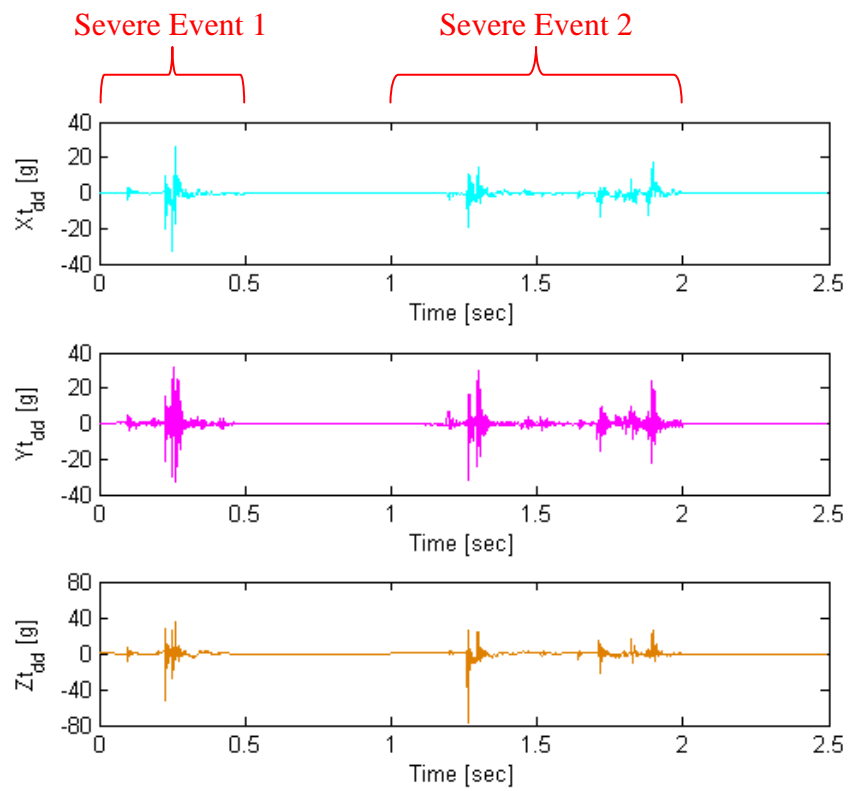


Figure 6-5. Severe shock input profile

## **CHAPTER 7**

### **RESULTS AND DISCUSSION**

This chapter details the design generation, simulation results, and discussion for both the stacked battery and single battery suspensions. The analytical model is the primary tool used to study the effectiveness of these suspension system designs. Statically-feasible designs are first generated by changing the sizes, locations, and quantities of the wire rope isolators. These isolators alone may not constitute dynamically-feasible designs. If this is the case, bump stops are incorporated and subsequently tuned for each of the isolator designs to utilize the full dynamic ranges of the battery and isolators. These two-phase designs are then simulated using the three base acceleration inputs from Chapter 6 and the results are analyzed in both the time and frequency domains. Once a leading isolator design is established, a bump stop design comprising silicone materials is optimized. Lastly, tradeoffs imbedded within the design space are presented to illustrate how tuning the system's dynamics can alter the suspension system's ability to meet certain requirements.

#### **7.1 Simulation Procedure**

The initial step in the suspension design process is to determine which wire rope isolator sizes offer statically-feasible solutions to use inside the tray. This is done by looking at two static properties of the isolators: geometric dimensions and maximum static load. The dimensions of the isolators must be small enough to physically fit within the tight clearance gaps within the tray. Additionally, the maximum static load of each isolator size designates the number of isolators needed to support the weight of the battery/battery stack. These two

properties yield the isolator designs that achieve the static requirements and can be used for dynamic simulation.

Next, the statically-feasible designs are simulated in order to differentiate their dynamic performances. Since wire rope isolators make up the primary component of the battery's suspension system, they must be designed before the bump stop designs are finalized. The isolator and bump stop designs cannot be completely decoupled from one another, however, because the isolators alone do not produce dynamically-feasible suspension solutions. In other words, the isolators exceed their maximum travel capabilities and/or the battery collides with the tray when simulating shock inputs without bump stops. These occurrences represent a physical failure of the suspension and the simulation is immediately deemed invalid.

In order to proceed with the isolator design, bump stops with linear stiffness and damping characteristics are incorporated and iteratively tuned such that the isolators utilize the entirety of their rated deflections during the severe shock simulations. By utilizing all of the allowable travel of each isolator design, the effect that the isolators' dynamic range has on battery performance can be analyzed consistently between designs. The bump stops are tuned independently for the longitudinal, lateral, top, and bottom battery faces and engage the battery after its displacement equals 50% of the isolators' maximum travel (this 50% is the baseline engage displacement which is later analyzed in Section 7.5). Using this approach, the bump stop designs do not differentiate the performances of suspension designs, but rather yield dynamically-feasible isolator designs that allow for consistent and unbiased comparison of the isolator designs themselves.

The final step is to design and optimize the bump stop using BISCO silicones. This optimization follows the flow chart procedure shown in Figure 7-1. First, the displacements at

which the bump stops engage the battery needs to be defined. The effect that this parameter has on performance is explored in Section 7.5. For cost considerations, the total area of the silicone sheets is minimized, which correlates to applying the bump stop to as few a number of attachment points as possible. The minimum number of sheets of silicone needed is calculated using the engage distances and individual sheet thickness. Next, an initial bump stop/isolator design is simulated with the severe shock input using the minimal area of the softest silicone foam (BF-1000). If the simulation results are not dynamically-feasible, meaning that the battery collides with the tray and/or isolators exceed their maximum deflections, then BF-1000 is substituted with a stiffer silicone. This process is repeated until 1) a successful simulation is achieved or 2) the hardest silicone rubber pad (HT-1250) is applied. If dynamically-feasible results are still not obtained with Ht-1250, then the area of the silicone is increased since bump stop compressive force increases proportionally with area. This process yields an optimal design given the specified isolator design and bump stop engage distances.

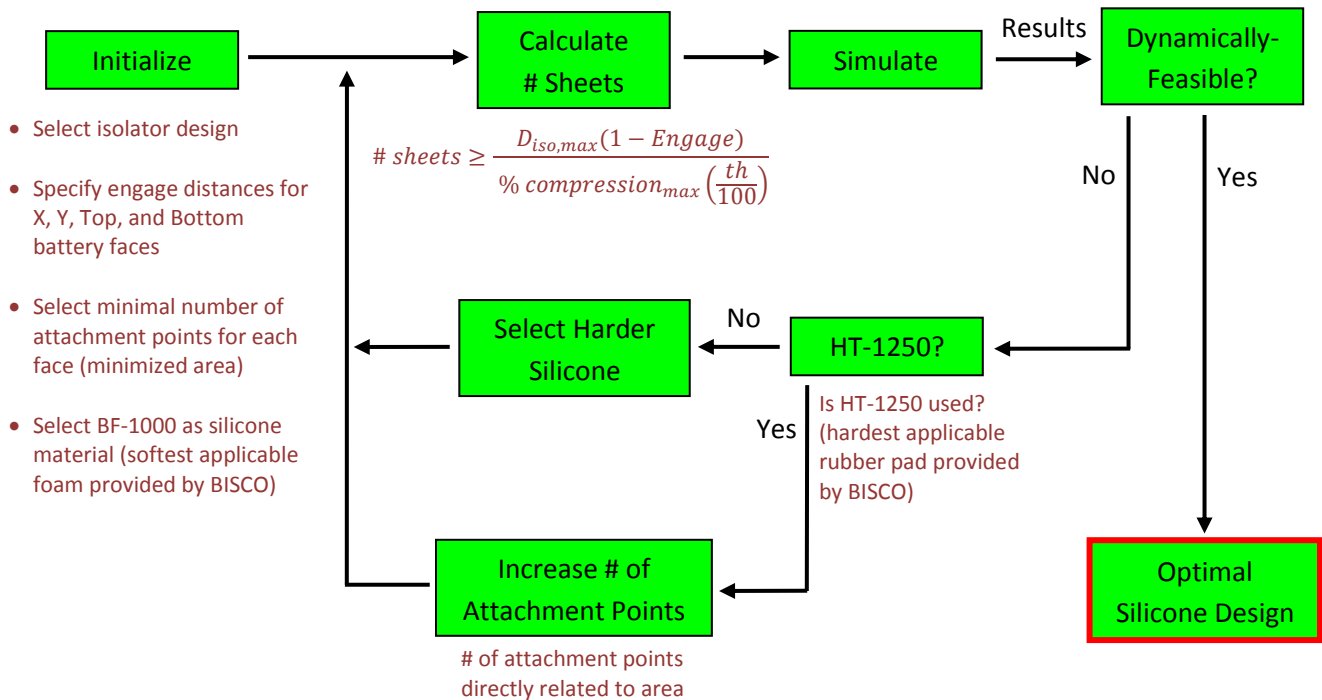


Figure 7-1. Bump stop optimization flow diagram

## 7.2 Analysis Methods

The simulation results are analyzed in a few ways. The first analysis is for dynamic-feasibility. The displacements of the eight corners of the battery/battery stack are compared to the clearances specified in Chapter 1. If the corner displacements exceed the clearances at any point, then a battery-tray collision has occurred. Furthermore, the deflections of the wire rope isolators are analyzed to see if they are operating within their elastic ranges. If both of these conditions are satisfied, then the results of the simulation are deemed dynamically-feasible.

The output battery accelerations produced from shock inputs are analyzed in the frequency domain using a shock response spectrum (SRS). A SRS is a technique that uses the acceleration response signal as the input to a single degree-of-freedom (SDOF) system. The natural frequency of the SDOF system varies with each simulation and the maximum peak acceleration magnitude is recorded. The SRS plots natural frequency on the x-axis and the peak acceleration of the response on the y-axis. More details of this method can be found in the Department of Defense military standard MIL-STD-816G, Method 516.6 [40].

Power spectral densities (PSD) are used to illustrate the effectiveness of vibration isolation. This is another frequency domain technique that plots the power density ( $g^2/Hz$ ) of the vibration signal as a function of frequency. The amount of isolation is quantified as the difference in power densities between the input and response. This difference is analyzed at 35 Hz since this frequency is where isolation is most necessary to avoid resonant excitation of the internal battery cells.

## 7.3 Stacked Battery Configuration

### 7.3.1 Isolator Design Generation

Many sizes of wire rope isolators are offered by IDC. Not all of these isolators are statically-feasible options to use in the suspension system. IDC's product catalog is initially filtered to extract isolators that physically comply with the clearances inside the tray. Specifically, the sum of the unsprung height of an isolator and its maximum deflection in the tension mode must be less than the total vertical clearance. This is shown with the inequality in Equation 7-1.

$$Height + D_{tension,max} < Clearance_z \quad (7-1)$$

Additionally, the relationship between the quantity of isolators required to statically support the battery stack's weight and the static load range is given by Equation 7-2.

$$Load_{min} \leq \frac{mg}{\# \text{ isolators}} \leq Load_{max} \quad (7-2)$$

Using these filtering criteria, three isolator sizes are identified. The number of isolators needed for these three sizes satisfies Equation 7-2. The geometric locations align with the attachment points on the bottom battery face that are closest to the bottom four corners (detailed in Section 5.1). These locations are the most effective isolator locations because the moment arms from the isolator forces are maximized. There are a total of six statically-feasible isolator designs for the battery stack configuration. Table 7-1 alphabetically labels these six designs A through F.

Table 7-1. Statically-feasible isolator designs for stacked battery configuration

Design	Isolator	$Load_{min}$ [lbs]	$Load_{max}$ [lbs]	$\frac{mg}{Load_{max}}$	$\frac{mg}{Load_{min}}$	# Isolators	$D_{static}$ [in]	Attachment Locations
A	M6-120	210	370	4.31	7.60	6	0.0634	1, 3, 5, 26, 28, 30
B	M6-130	160	280	5.70	9.98	6	0.0832	1, 3, 5, 26, 28, 30
C						8	0.0624	1, 2, 4, 5, 26, 27, 29, 30
D	M6-140	125	215	7.42	12.78	8	0.0798	1, 2, 4, 5, 26, 27, 29, 30
E						10	0.0639	1-5, 26-30
F						12	0.0532	1-5, 6, 10, 21, 25, 26-30

To supplement Table 7-1, Figure 7-2 shows the maximum allowable displacement for each of the isolator designs.

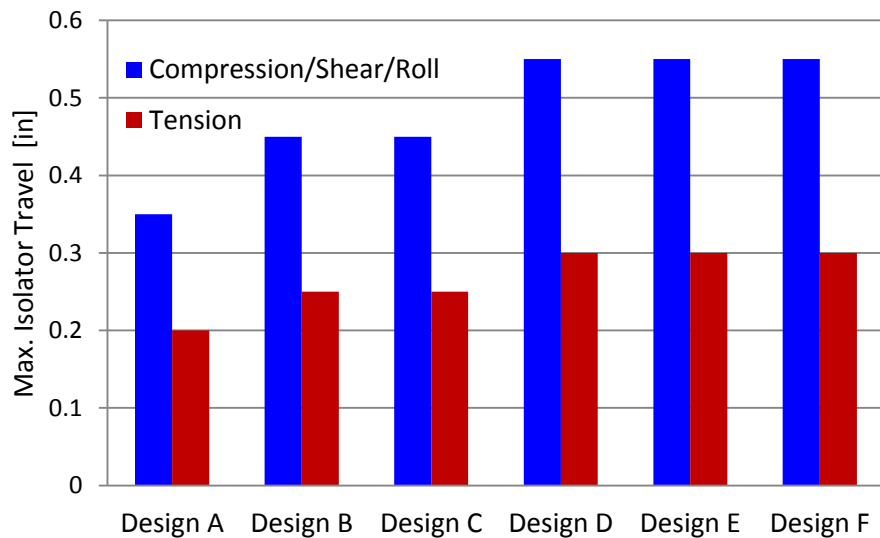


Figure 7-2. Maximum travel capabilities of battery stack isolator designs

### 7.3.2 Simulation Results

As discussed in Section 7.1, the isolator and bump stop designs cannot be completely decoupled. The bump stops are needed to prevent battery-tray collisions and to keep the isolators operating within their elastic ranges. To better illustrate the battery response without a bump stop, a simulation is performed only using the wire rope isolators comprising Design A. Six M6-120 isolators are placed underneath the battery stack in accordance with Table 7-1, and the system's response is simulated using the severe shock tray input. Figure 7-3 depicts the three-axis deflections of the wire rope isolators connected to attachment point '30'. The maximum allowable displacements of the M6-120 isolator (obtained from Figure 7-2) are shown as dotted magenta lines.

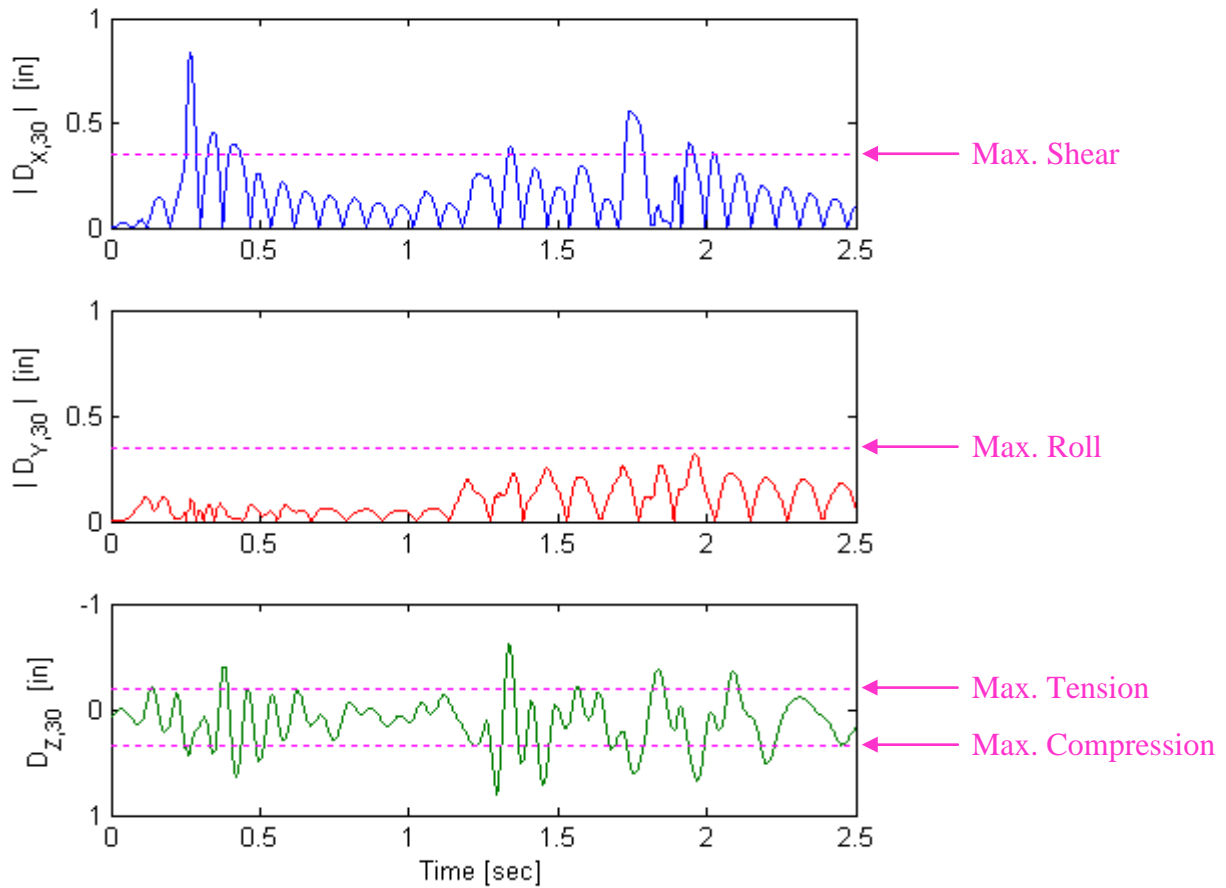


Figure 7-3. Isolator displacements without using bump stops (Design A)

The isolator in Figure 7-3 exceeds its maximum allowable travel in shear, compression, and tension, as indicated by intersection with the dotted magenta lines. The isolator cannot displace these amounts due to physical constraints, so these simulation results are dynamically infeasible.

Furthermore, the lateral displacement of the battery stack's corner that intersects the top, right, and front faces is shown in Figure 7-4. This corner travels more than 0.75" which exceeds the clearance in the  $Y_t$  direction. This represents a collision with the side wall of the tray, and again, invalidates the simulation results. This analysis illustrates why a bump stop must be utilized when simulating the six isolator designs.

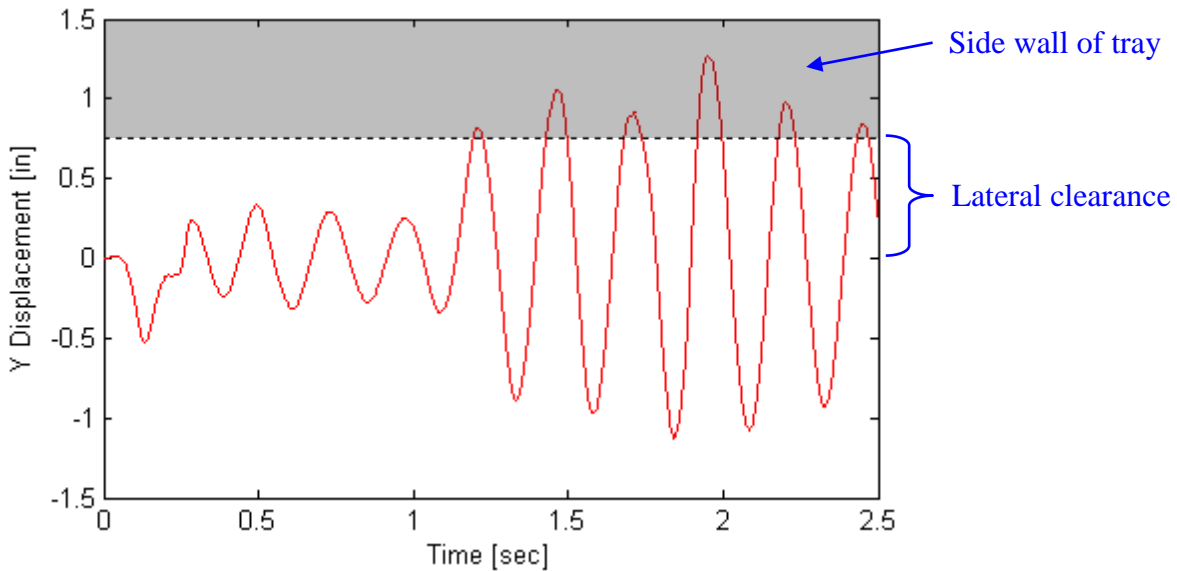


Figure 7-4. Battery stack collision with side wall of tray

In order to proceed with simulation of the isolator designs, bump stops must be incorporated. Through an iterative process, the bump stops for each isolator design are tuned such that the isolators achieve, but do not exceed, their maximum travel in each axis, as

mentioned in Section 7.1. The isolators in attachment locations “1”, “5”, “25”, and “30” always have the largest displacements because they are located furthest from the battery stack CG. Therefore, if these isolators are within the acceptable travel ranges, then it is guaranteed that all isolators have dynamically-feasible behaviors.

Design A is re-simulated using the severe tray input, but this time incorporating the tuned bump stops. Figure 7-5 shows the displacements of the attachment point ‘30’ isolator. The red shaded regions represent contact with a bump stop, since the bump stops become engaged at 50% maximum isolator travel.

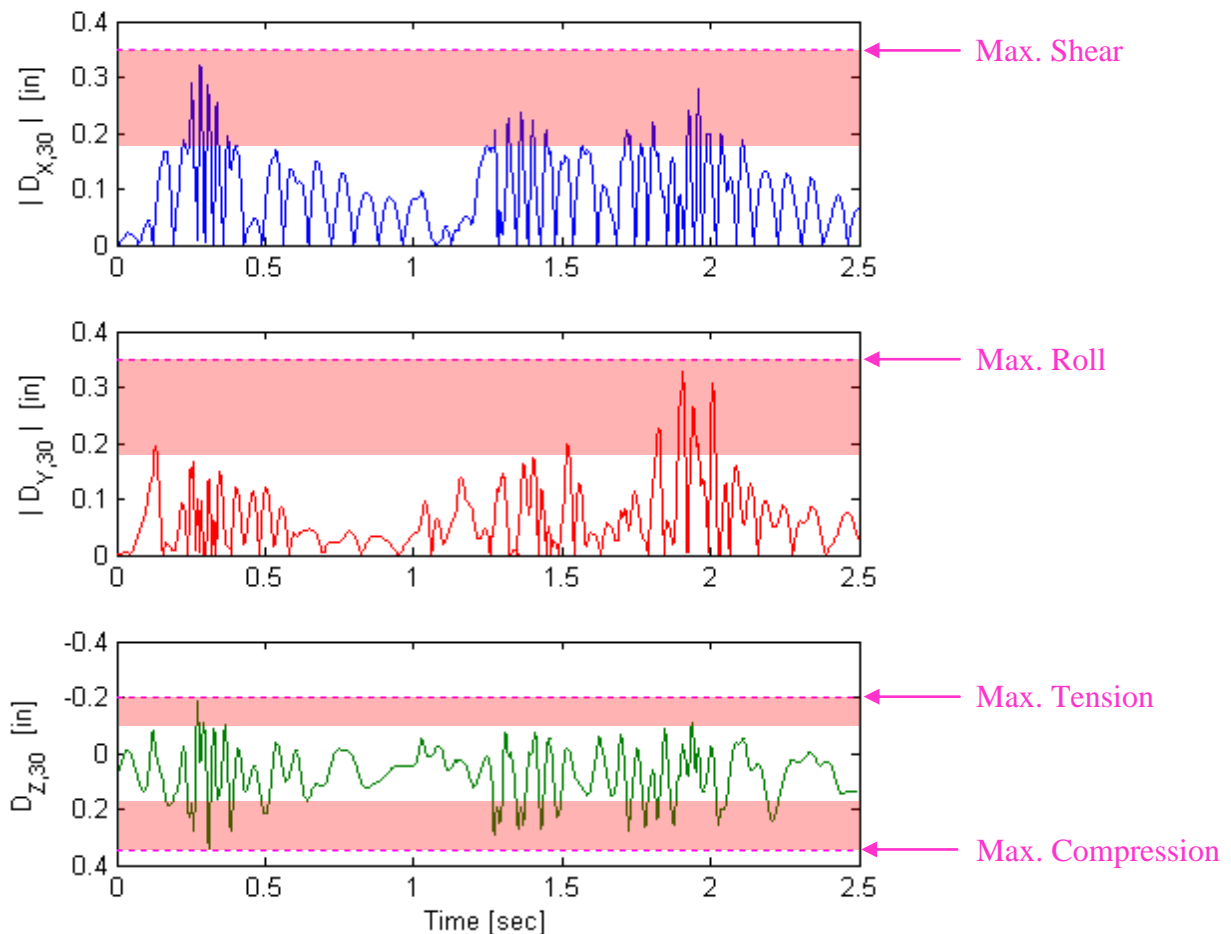


Figure 7-5. Isolator displacements with tuned bump stops (Design A)

Using the tuned bump stop design for Design A, the battery stack's acceleration response is analyzed using a shock response spectrum. The SRS corresponding to the severe tray input is plotted for all three axes in Figure 7-6. The SRS of the inputs are included as well for comparison.

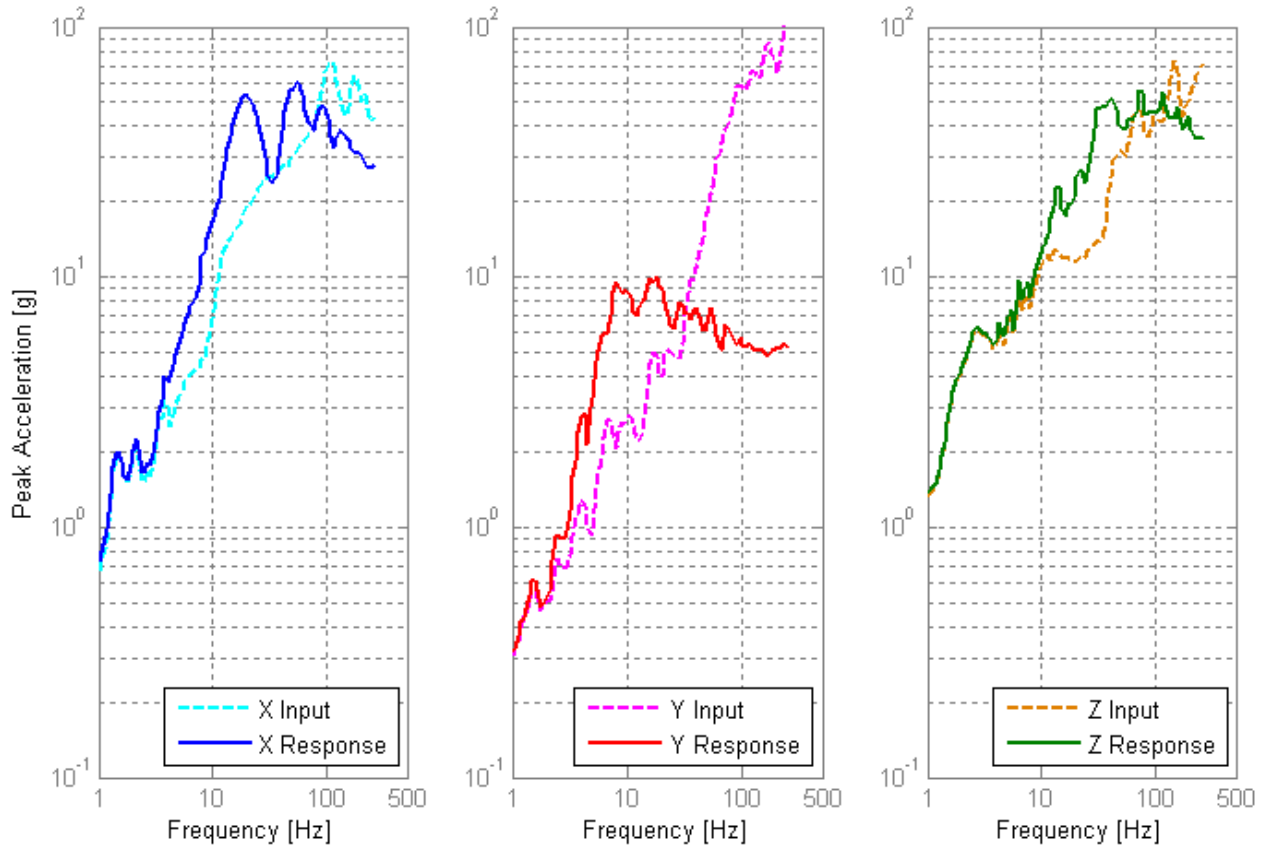


Figure 7-6. SRS using severe shock input (Design A)

This same system is again simulated using the typical shock input. The battery stack accelerations are analyzed in both the time and frequency domains, plotted in Figures 7-7 and 7-8. The typical SRS shows much lower acceleration peaks as compared to the severe SRS. From Figure 7-8, the accelerations peaks in the X and Z axes are roughly 10 g in magnitude.

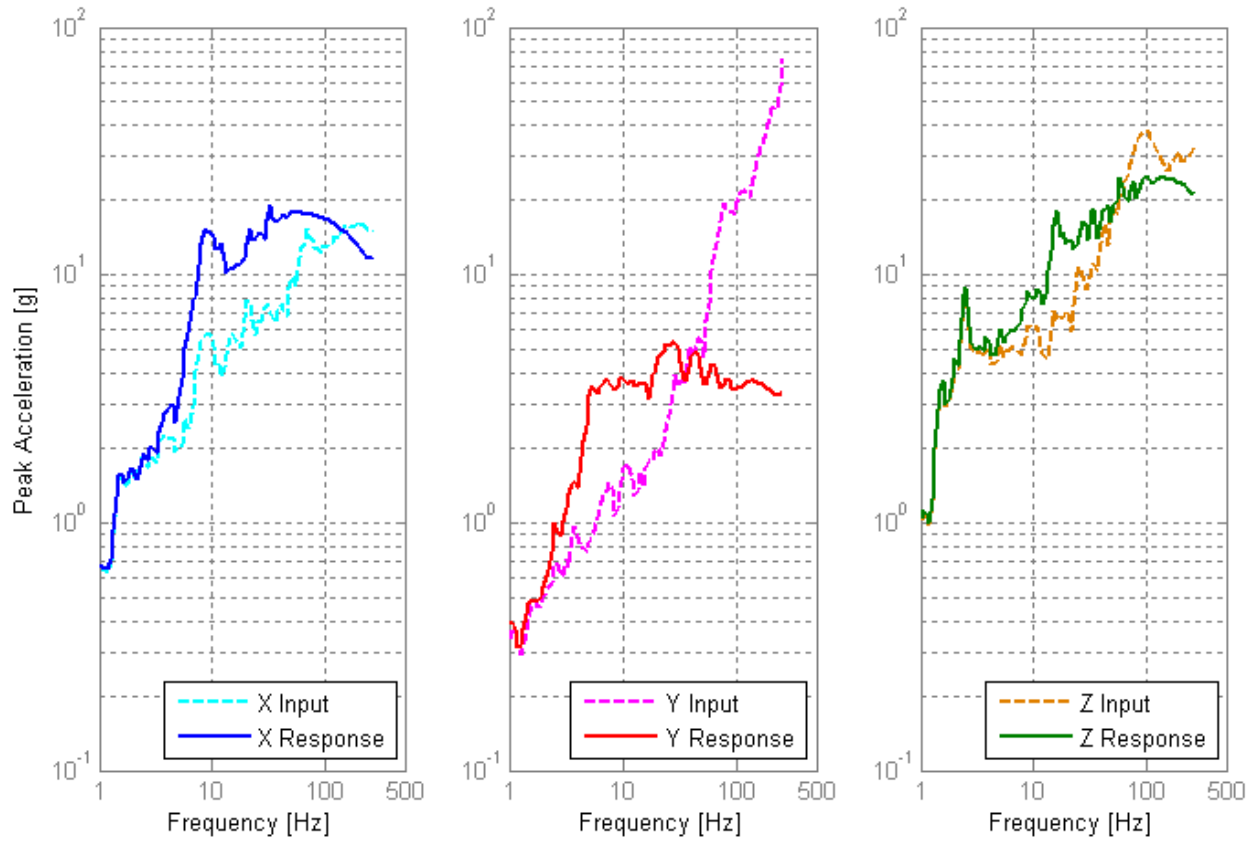


Figure 7-7. SRS using typical shock input (Design A)

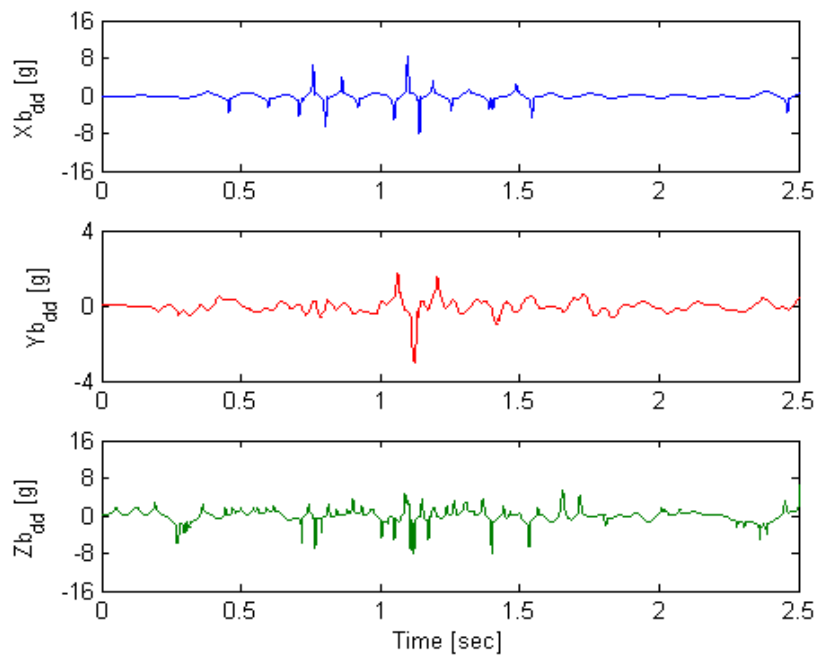


Figure 7-8. Battery stack CG accelerations using typical shock input (Design A)

The first six state variables for the typical shock simulation are plotted in Figure 7-9. These correspond to the relative translational and rotational displacements of the battery stack with respect to the tray. As shown, the battery stack's CG displaces less than 0.4" in all three directions. The stack undergoes negligible yaw and less than 1° of roll and pitch.

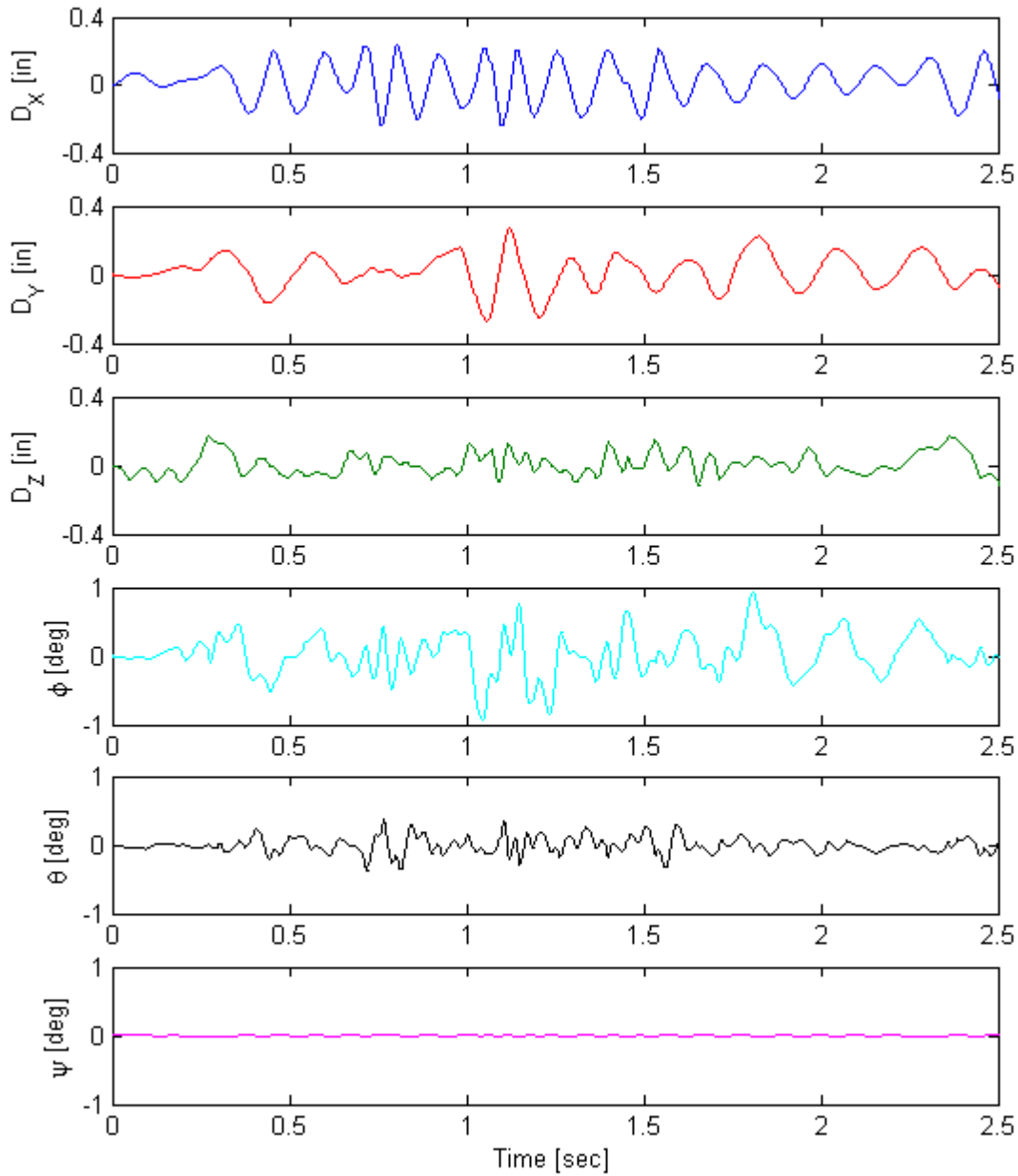


Figure 7-9. Relative displacements of battery stack using typical shock input (Design A)

Lastly, the vibration response is simulated for Design A. The power spectral densities in the three axes of the vibration input and response are plotted in Figure 7-10. At 35 Hz, the PSD of the response is lower than that of the input, indicating that isolation is achieved. The X and Y axes achieve about two orders of magnitude in isolation whereas the Z direction achieves about one order of magnitude reduction.

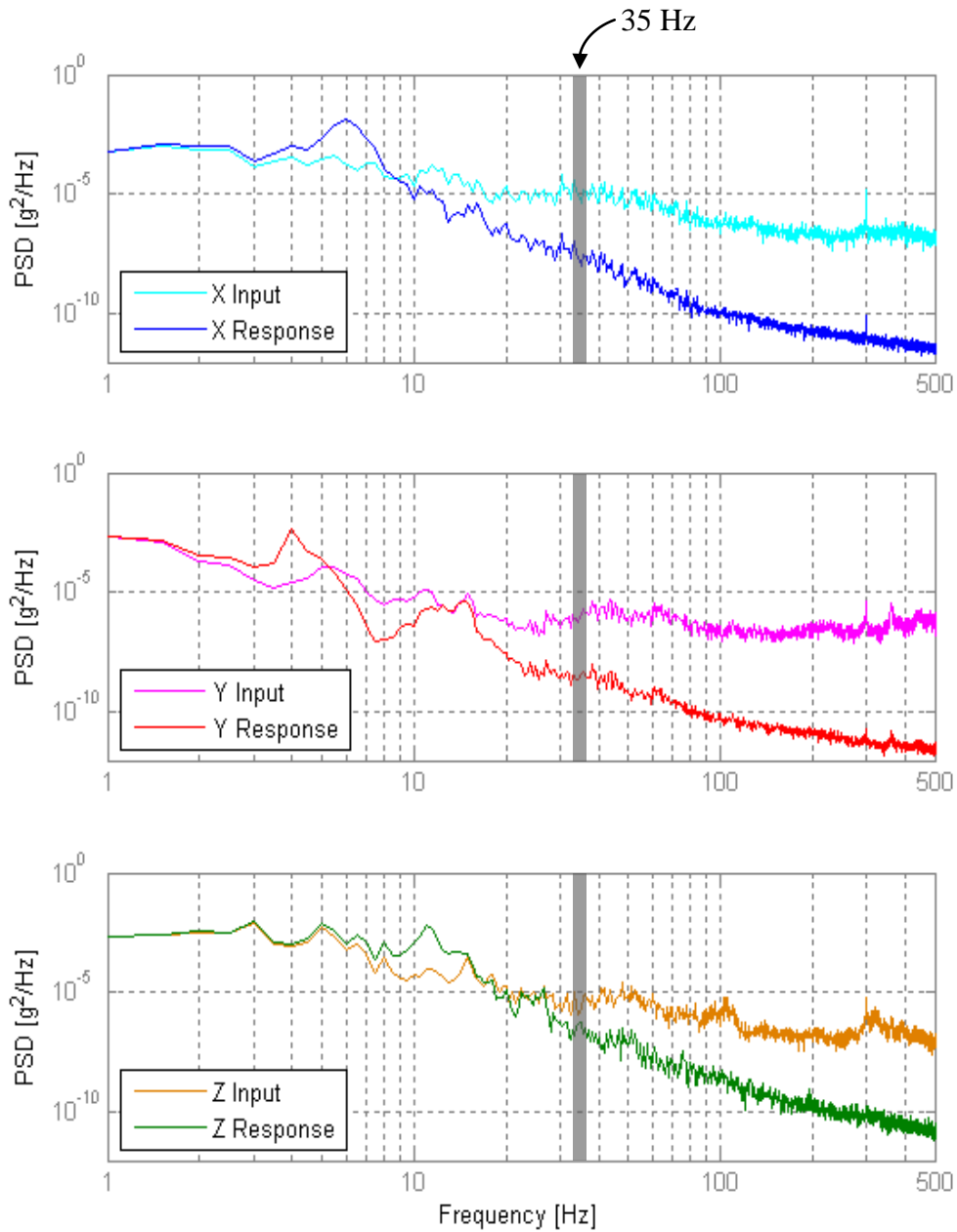


Figure 7-10. Power spectral density of vibration response (Design A)

The dynamic performances of all six isolator designs are now analyzed using the same exemplary plots shown for Design A. Each design incorporates its own iteratively tuned bump stops to utilize the full range of motions of the isolators. Firstly, simulations of Designs A through F are completed for the severe shock input. The SRS of the acceleration responses is shown in Figure 7-11. The maximum magnitudes of these acceleration responses are also recorded in the time domain and plotted as column graphs in Figure 7-12.

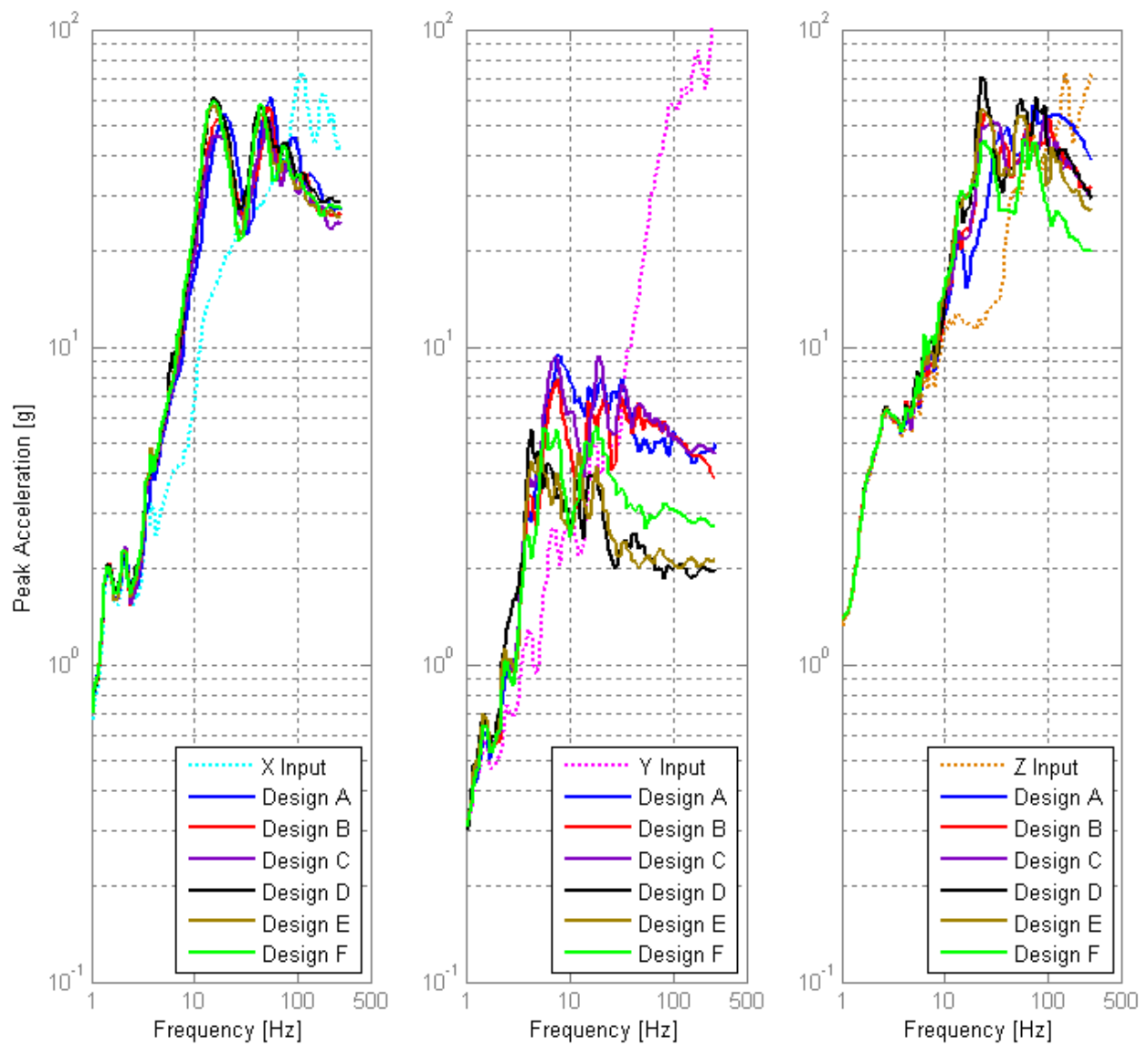


Figure 7-11. SRS of stacked battery designs using severe shock input

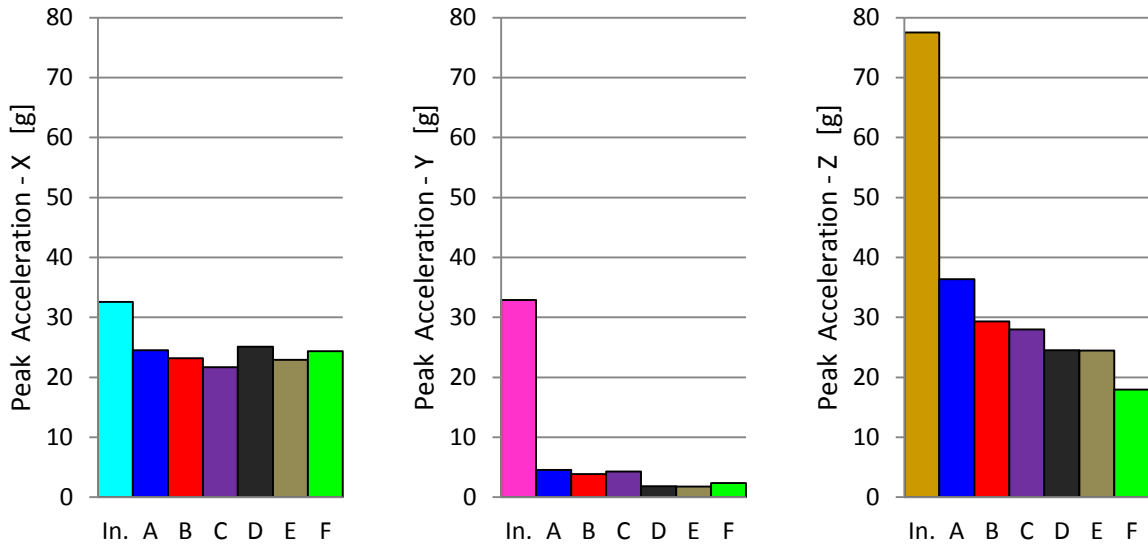


Figure 7-12. Maximum acceleration magnitudes of battery stack using severe shock input

The same designs are simulated using the typical shock tray input. The peak accelerations in the time domain are shown below in Figure 7-13. The corresponding SRS is plotted in Figure 7-14.

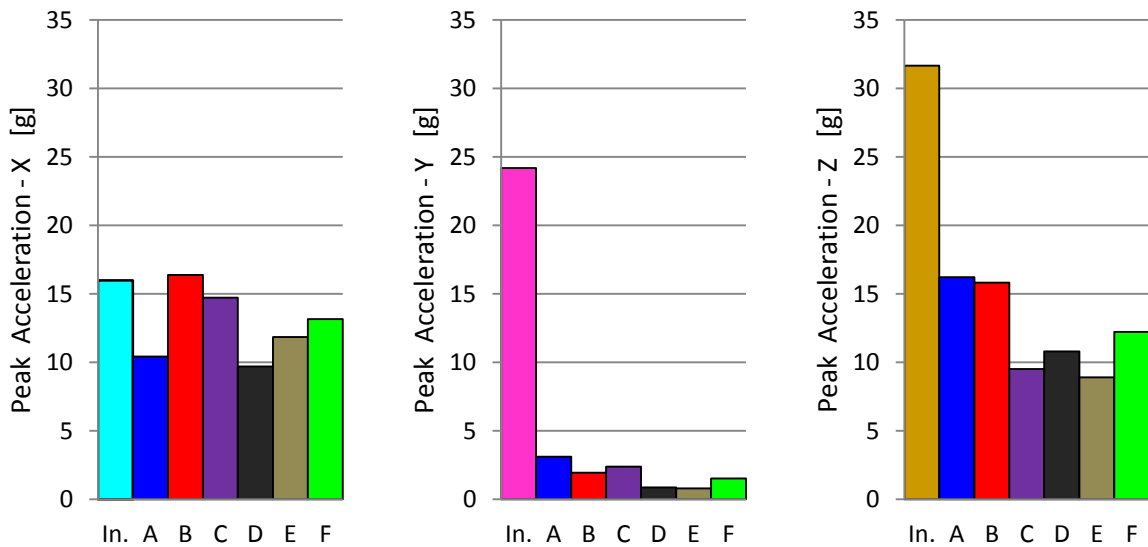


Figure 7-13. Maximum acceleration magnitudes of battery stack using typical shock input

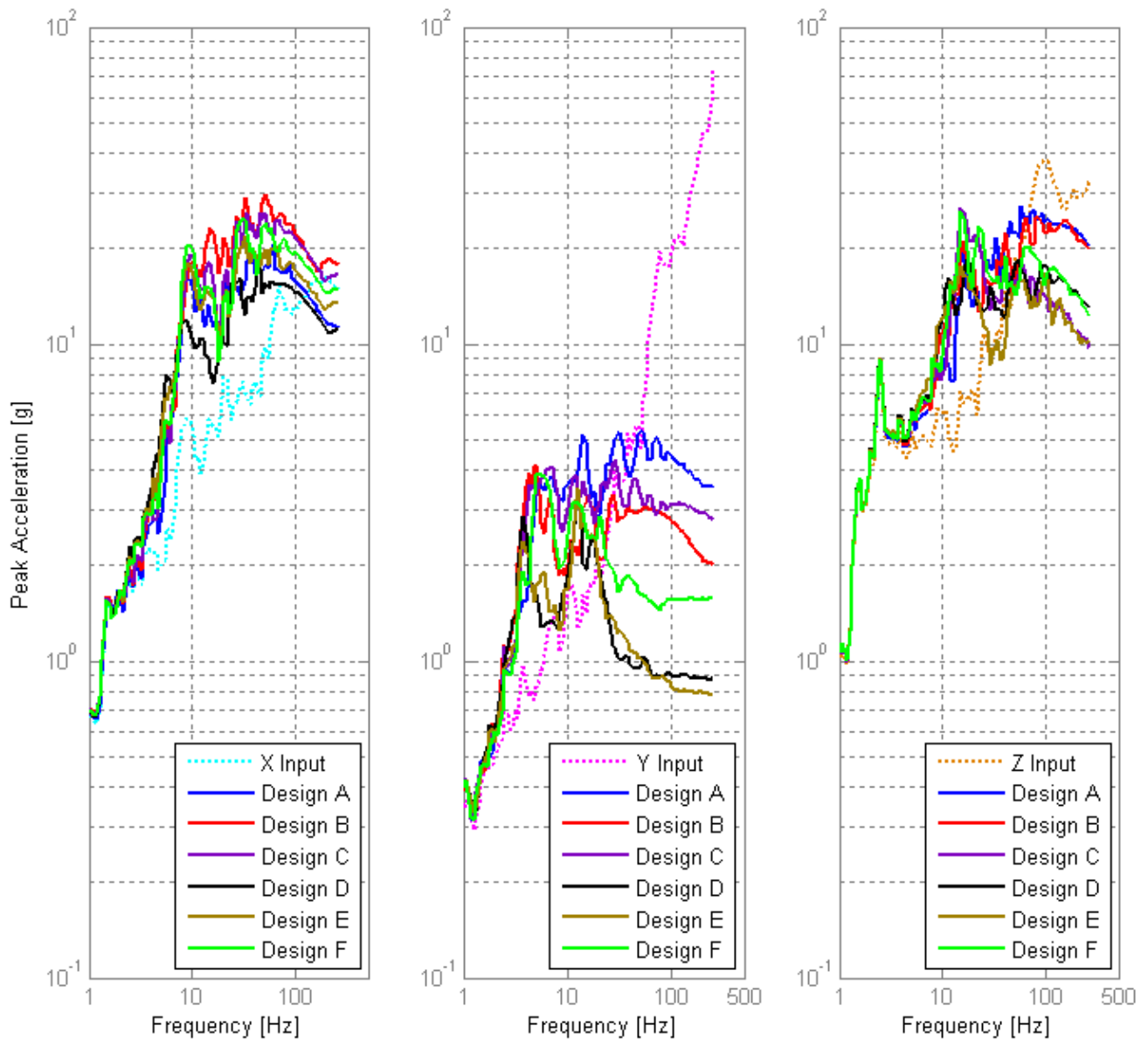


Figure 7-14. SRS of stacked battery designs using typical shock input

As is shown from the column graphs, all suspension designs offer significant shock attenuation in the *Y* and *Z* directions. The *Y* direction offers the best attenuation of the three axes. In the *X* direction, however, shock attenuation is inconsistent between designs. Design A displays the least amount of attenuation out of all designs in the *Y* and *Z* directions. The typical

and shock SRS figures show that the designs exhibit neither shock attenuation nor amplification at very low frequencies ( $< 4$  Hz). As the frequency increases, the responses begin to amplify the input signals. However, at sufficiently higher frequencies, the opposite is true and shock attenuation becomes prevalent. Designs D, E, and F, in general, seem to have the best shock attenuation across all three directions for typical and severe shock events.

Finally, the isolator designs are simulated using the vibration tray input. A PSD of the simulation results is performed to analyze the effectiveness of vibration isolation. Figures 7-15 through 7-17 show the PSD of the six designs in the X, Y, and Z axes, respectively.

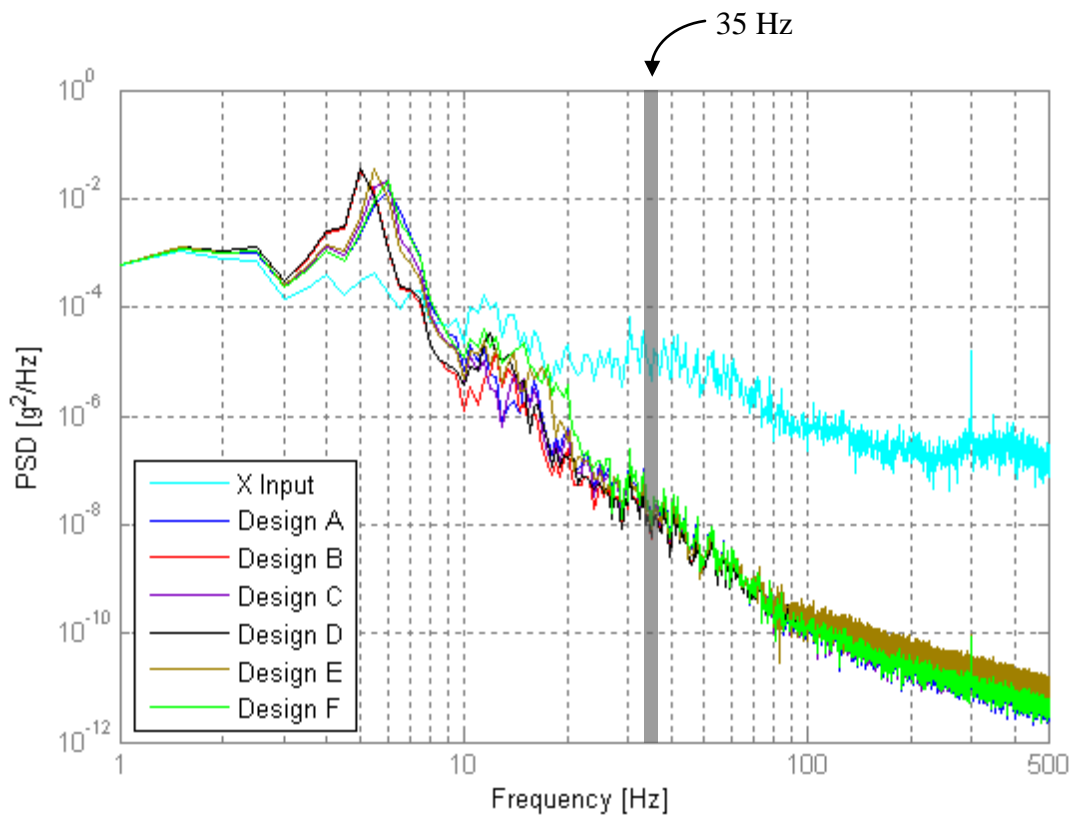


Figure 7-15. PSD of battery stack vibration response in X direction

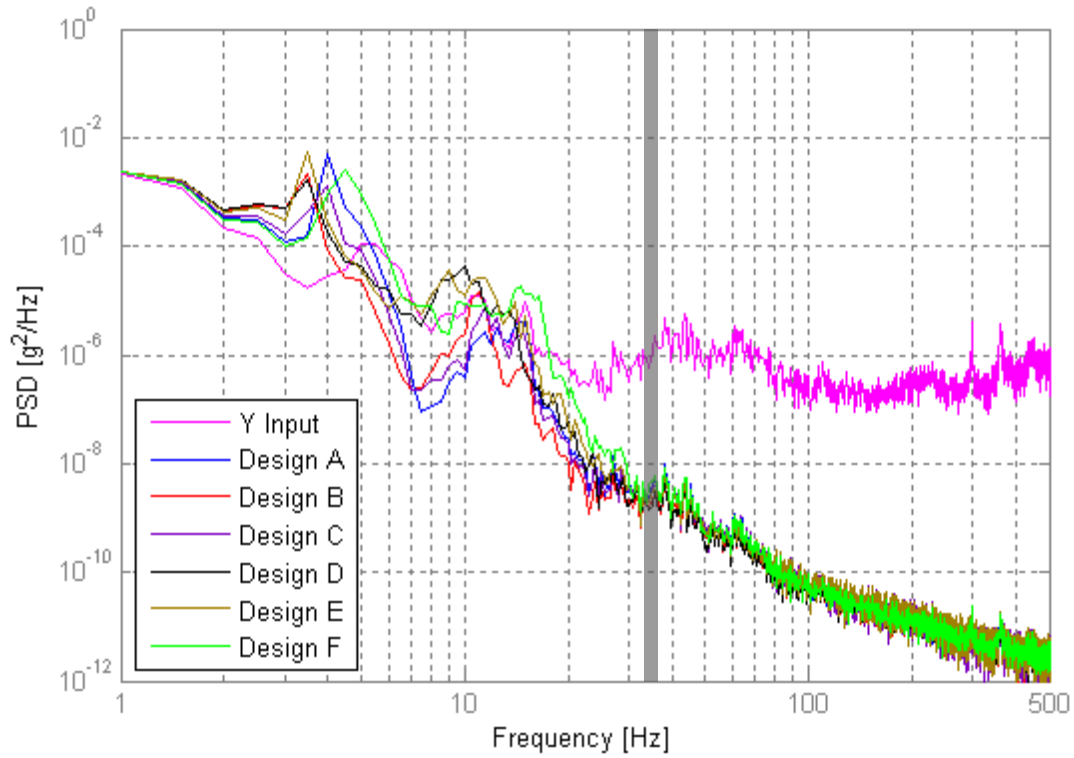


Figure 7-16. PSD of battery stack vibration response in Y direction

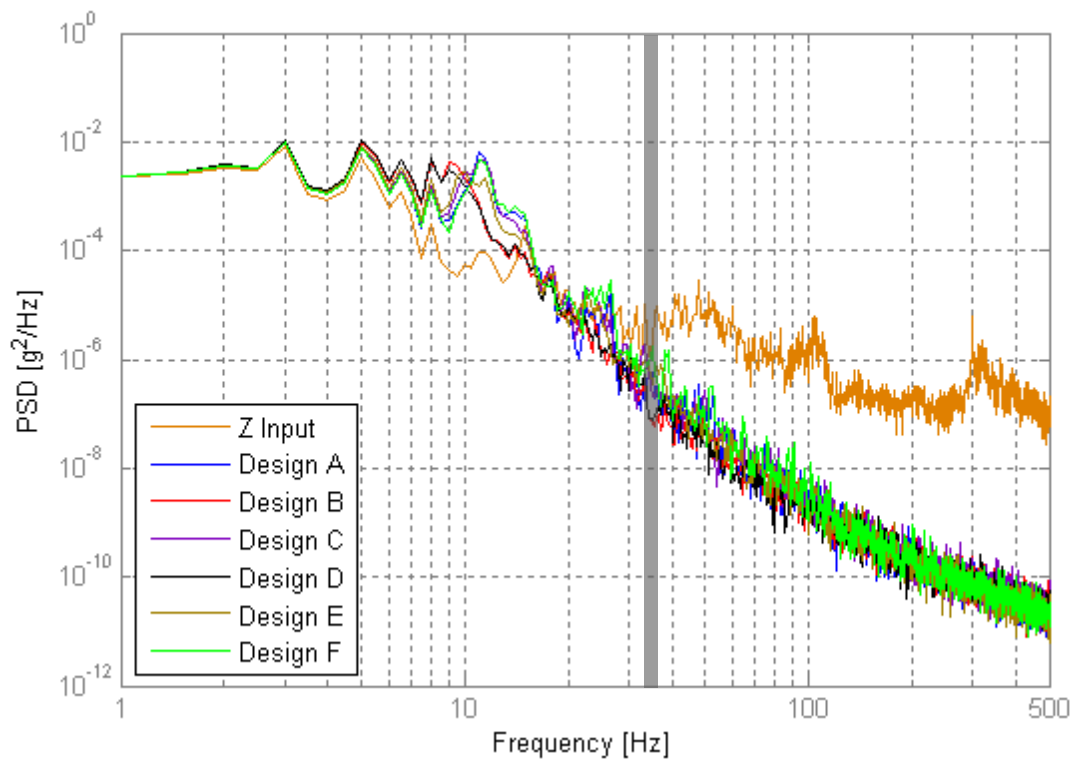


Figure 7-17. PSD of battery stack vibration response in Z direction

From Figures 7-15 through 7-17, all isolator designs provide vibration isolation at 35 Hz. Approximately three orders of magnitude reduction in power density is achieved in the *X* and *Y* signals for all designs as compared to the input. Roughly two orders of magnitude reduction is exhibited in the *Z* direction. There is very little disparity between the PSD responses of the isolator designs; this vibration analysis alone is not sufficient to distinguish the best isolator design.

### **7.3.3 Bump Stop Design**

From the studies presented for the stacked battery configuration, there is no one isolator design that stands well above the rest in terms of performance. Each design has similar performance across the vibration and shock evaluations. It does seem that Designs D, E, and F have slightly better attenuation characteristics. These three designs are composed of M6-140 wire rope isolators. The ultimate isolator selection will have to come down to other requirements such as cost and ease of installation.

For the purposes of demonstrating a feasible bump stop design, Design E is selected. The design procedure follows the flow chart detailed in Section 7-1. The engage distances are chosen to be 50% of the isolator's maximum travel in the shear, roll, compression, and tension deflection modes. The goal is to use adequately stiff BISCO silicone materials to minimize the area required to keep the suspension response within its dynamically-feasible limits.

The optimized bump stop design for Design E is shown in Figure 7-18. Table 7-2 details the design's parameters.

Table 7-2. Optimized bump stop design for Design E

Direction	Engage	Material	Thickness [in]	# Sheets	Attachment Locations
X	50 %	HT-1250	1/8"	4	5, 10, 15
Y	50 %	BF-1000	1/2"	1	1, 26
Top	50 %	HT-1250	1/8"	3	1, 5, 26, 30
Bottom	50 %	HT-1250	1/8"	4	

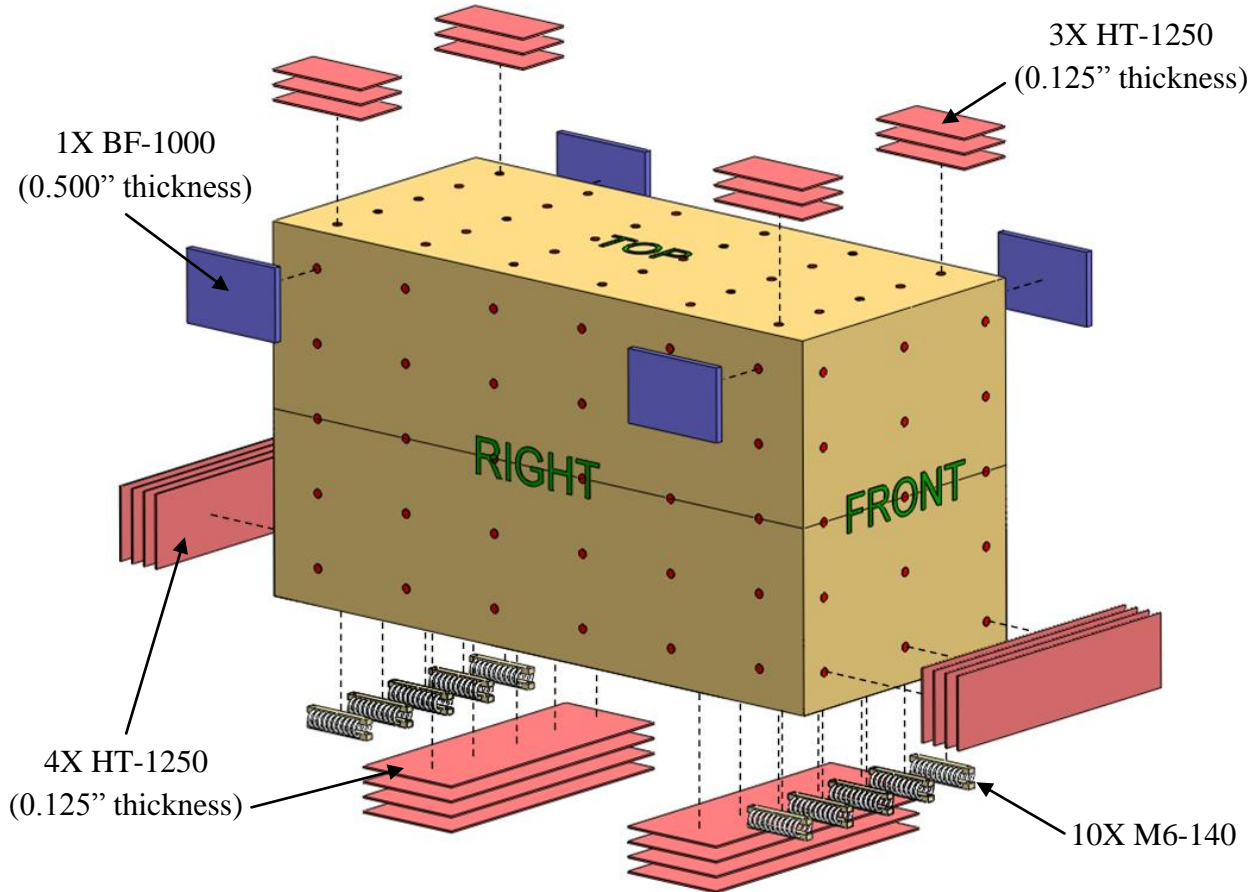


Figure 7-18. Bump stop design for Design E

Side and front views of the silicone bump stop design are also depicted in Figures 7-19 and 7-20. Shims are required between the inner walls of the tray and the silicone sheets in order to allow the bump stops to engage the battery stack at the desired displacements.

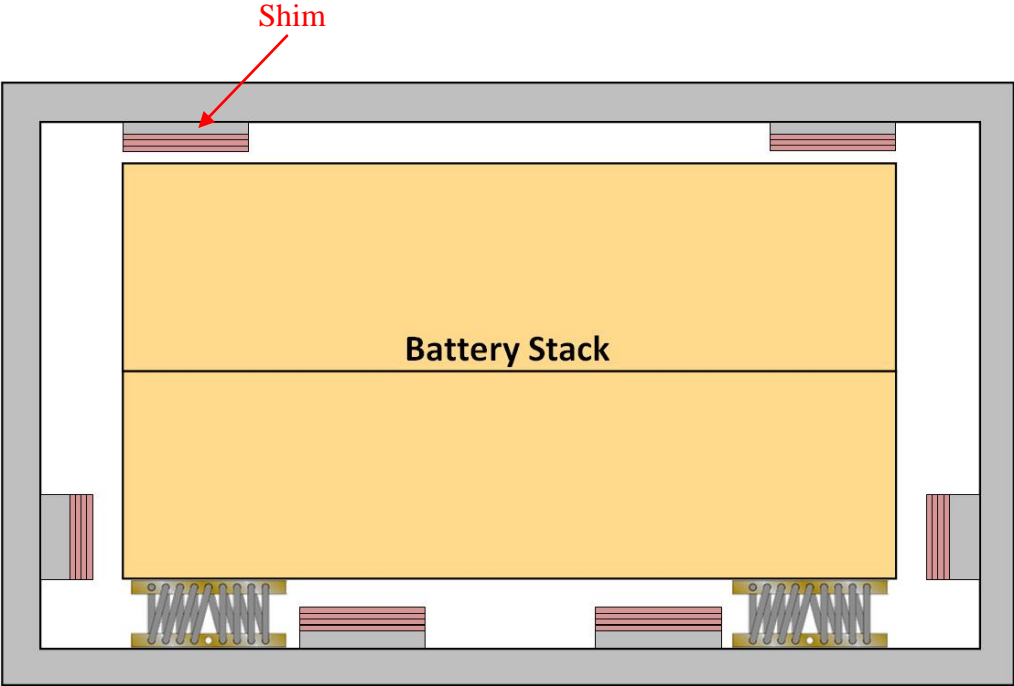


Figure 7-19. Side view of bump stop design for isolator Design E

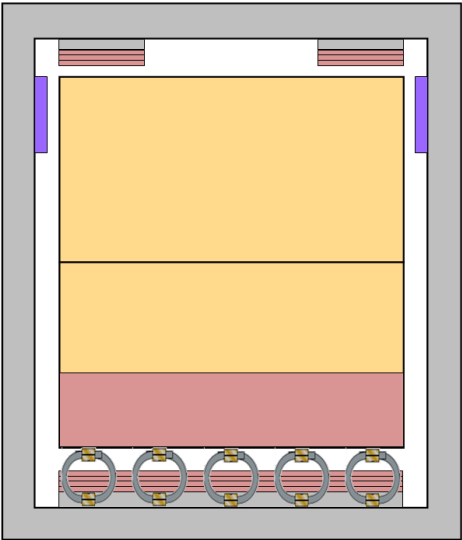


Figure 7-20. Front view of bump stop design for isolator Design E

## 7.4 Single Battery Configuration

### 7.4.1 Isolator Design Generation

The same isolator filtering process is performed for the single battery configuration to obtain statically-feasible isolator designs. The number of isolators required in a design is related to the static load range as previously mentioned in Equation 7-2. Since the isolators are placed in the front and back clearance gaps within the tray, their unsprung width and maximum shear deflection are the critical properties for geometric analysis. The isolator must satisfy the following size criteria

$$width + 2D_{shear,max} < Clearance_x \quad (7-3)$$

After eliminating the statically-infeasible isolator sizes, six isolator designs are deemed compatible with the single battery configuration. Table 7-3 presents these six designs.

Table 7-3. Statically-feasible isolator designs for single battery configuration

Design	Isolator	$Load_{min}$ [lbs]	$Load_{max}$ [lbs]	$\frac{mg}{Load_{max}}$	$\frac{mg}{Load_{min}}$	# Isolators	$D_{static}$ [in]	Attachment Locations
A	M6-120	210	370	2.45	4.32	4	0.0541	3, 13
B	M6-130	160	280	3.24	5.68	4	0.0710	3, 13
C	M6-140	125	215	4.22	7.26	6	0.0606	3, 8, 13
D	M6-150	95	160	5.68	9.56	6	0.0797	3, 8, 13
E						8	0.0598	1, 5, 11, 15
F	M10-215	169	304	2.99	5.37	4	0.0673	3, 13

Figure 7-21 shows the maximum allowable displacement for each of the isolators that comprise the six designs in Table 7-3.

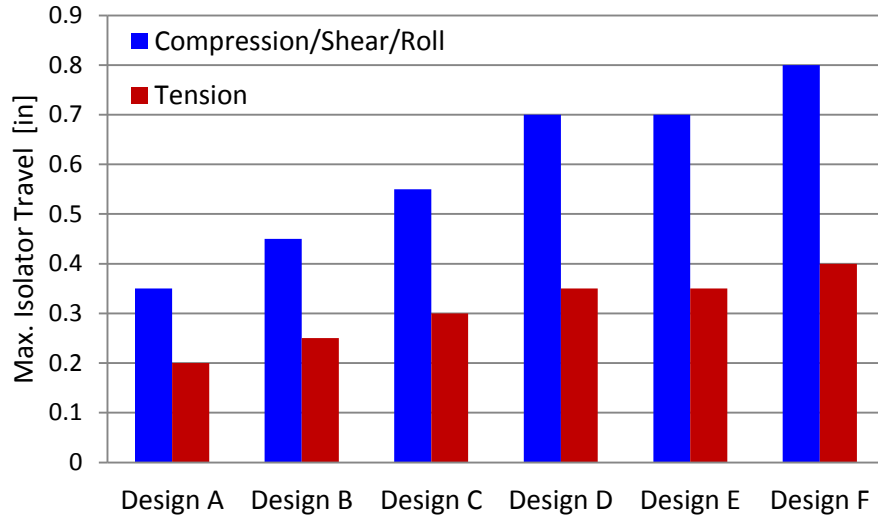


Figure 7-21. Maximum travel capabilities of single battery isolator designs

#### 7.4.2 Simulation Results

In all six designs, the isolators are installed symmetrically with respect to the battery CG. This setup keeps the battery inherently balanced within the tray and therefore, translational motion of the tray does not cause any rotation of the battery. Consequently, the 6DOF model is essentially reduced to three independent, SDOF systems for the single battery configuration.

The six isolator designs are simulated using the vibration and shock tray inputs. The simulation results for Design F are included for exemplary purposes. As with the stacked configuration, bump stops are needed to keep the system within its operable range. The time response of the isolator at attachment point '3' on the front battery face in Design F (using the severe shock input) is shown in Figure 7-22, in the absence of a bump stop design.

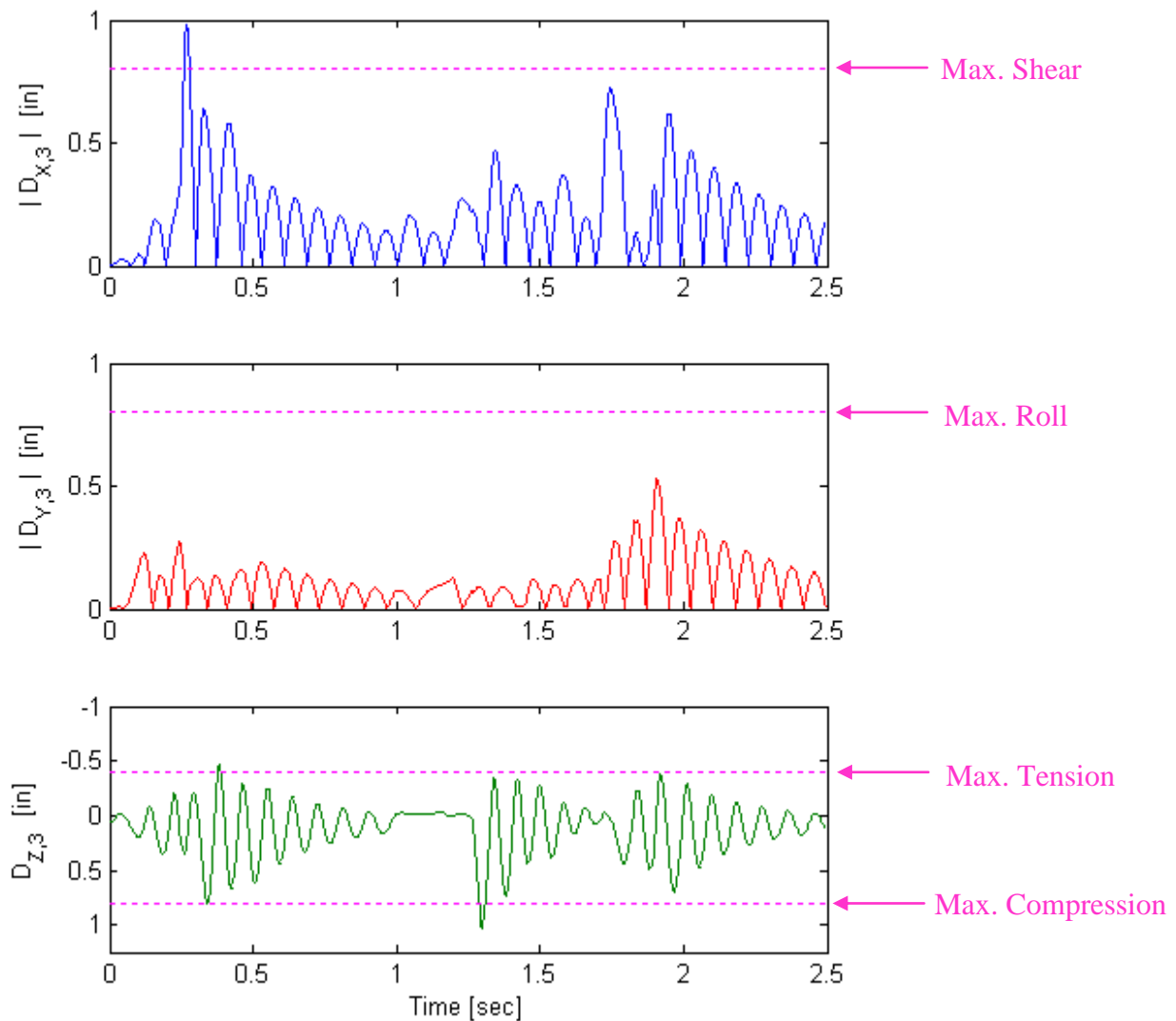


Figure 7-22. Isolator displacements without using bump stops (Design F)

In the single battery configuration, every isolator (every point on the battery in fact) experiences the same displacements because the battery does not rotate whatsoever. From Figure 7-22, isolator ‘3’, and equivalently every isolator, exceeds the maximum travel in shear, compression, and tension. As with the stacked configuration, bump stops must again be utilized to yield dynamically-feasible simulation results. Figure 7-23 shows the deflections of isolator ‘3’ in Design F after incorporating linear bump stops tuned at 50% engage distances.

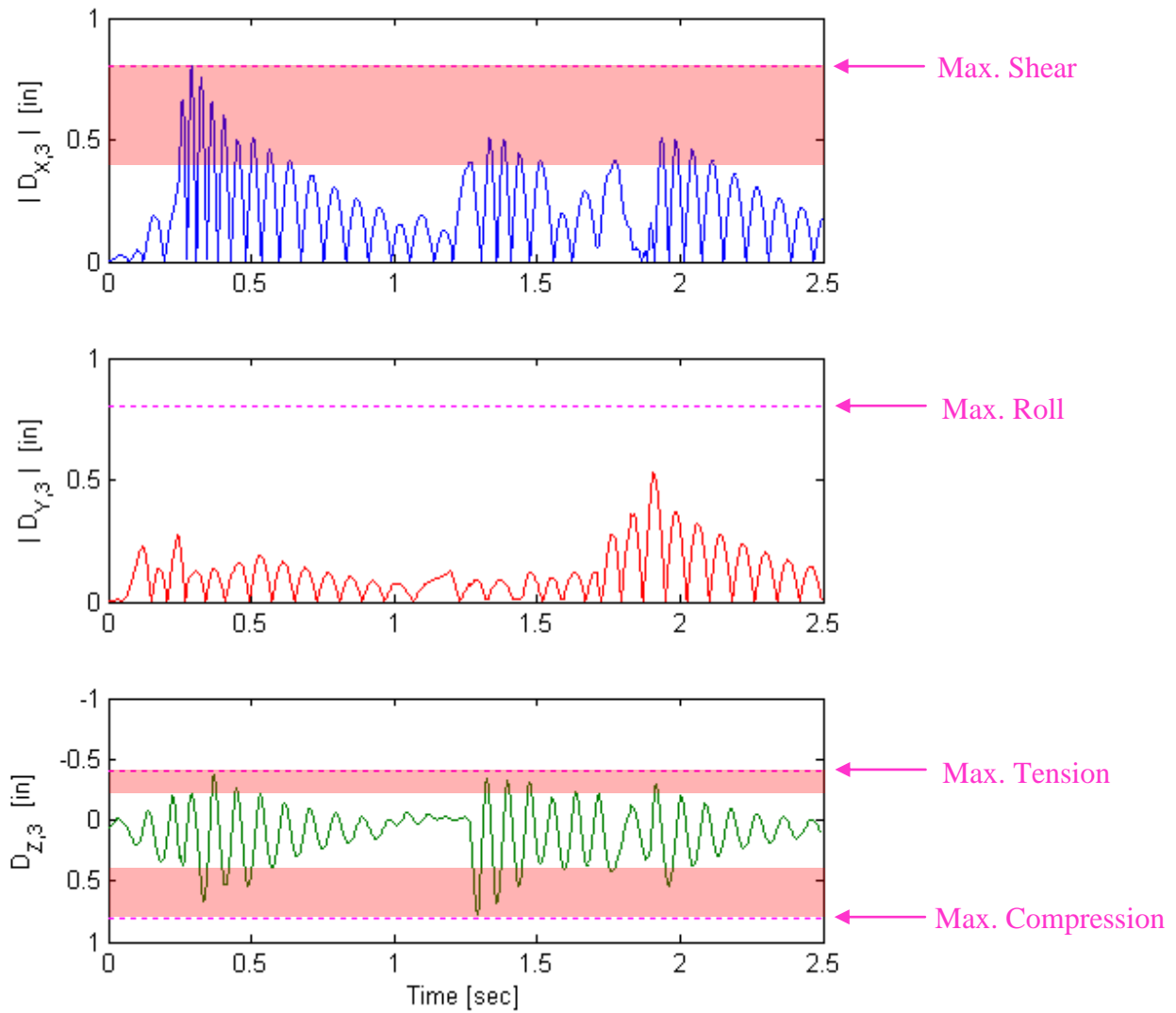


Figure 7-23. Isolator displacements with tuned bump stops (Design F)

The battery output accelerations and first six states corresponding to the above simulation are shown in Figures 7-24 and 7-25, respectively. It is seen from Figure 7-25 that no battery rotation occurs since all three Euler angles remain zero throughout the simulation.

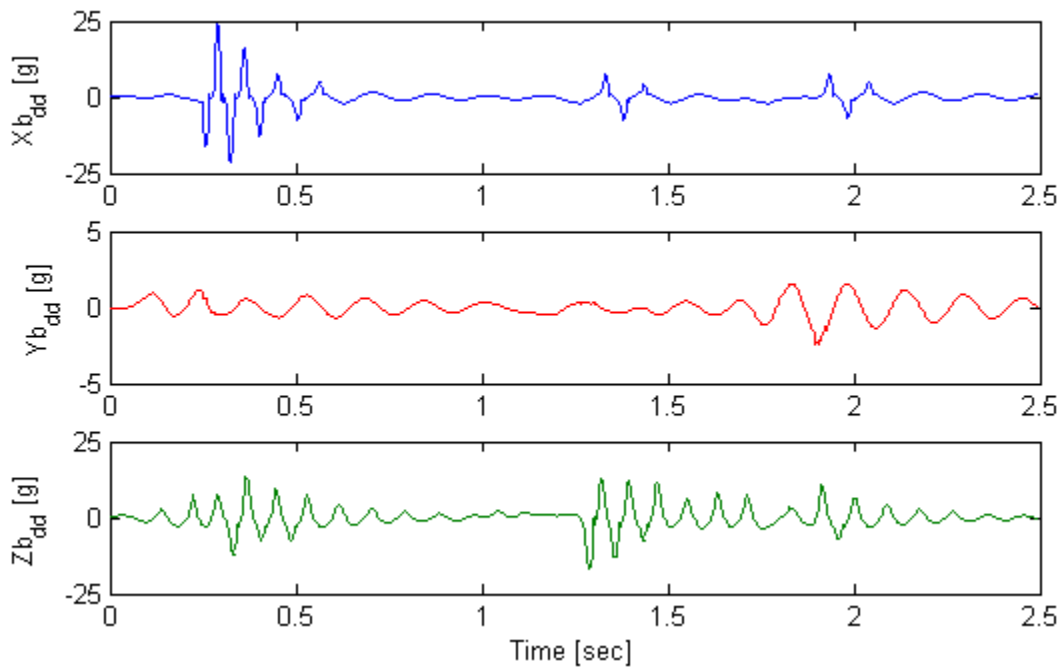


Figure 7-24. Battery CG accelerations using severe shock input (Design F)

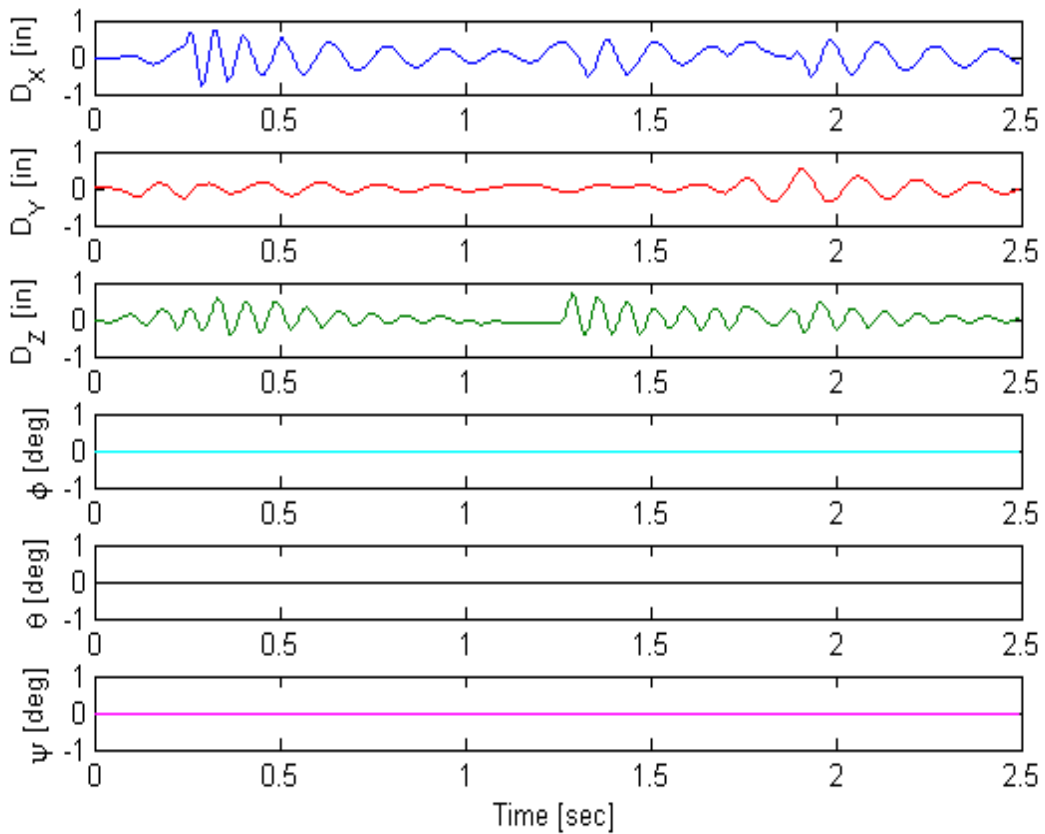


Figure 7-25. Relative displacements of battery using severe shock input (Design F)

A shock response spectrum is used to analyze the battery output accelerations of all six isolator designs in the frequency domain, as shown in Figure 7-26. These SRSs correspond to the severe shock input. The bump stops for each design are iteratively tuned to utilize the full range of motions of the isolators. Figure 7-27 displays the maximum peak amplitudes recorded in the time domain for the acceleration signals.

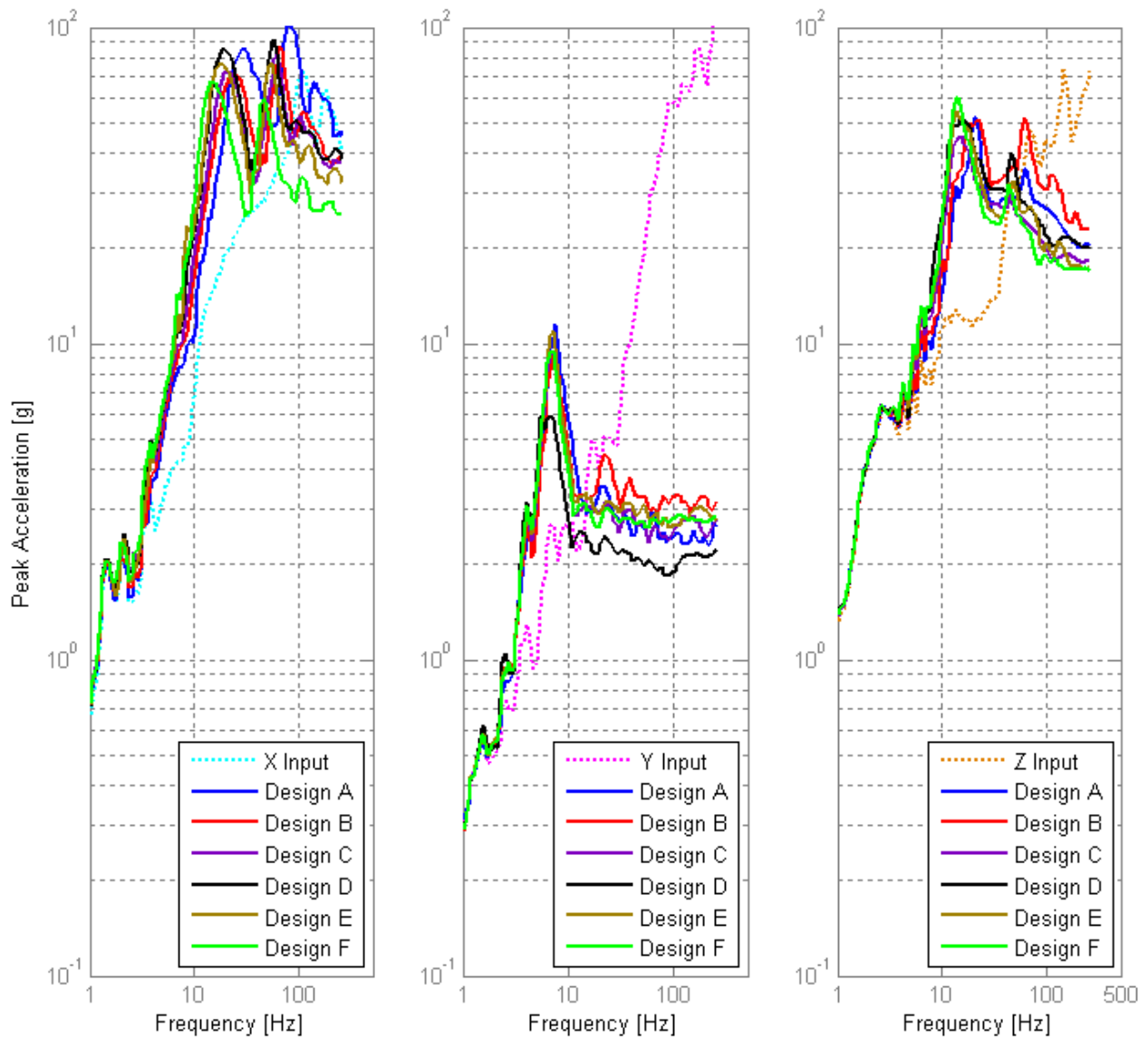


Figure 7-26. SRS of single battery isolator designs using severe shock input

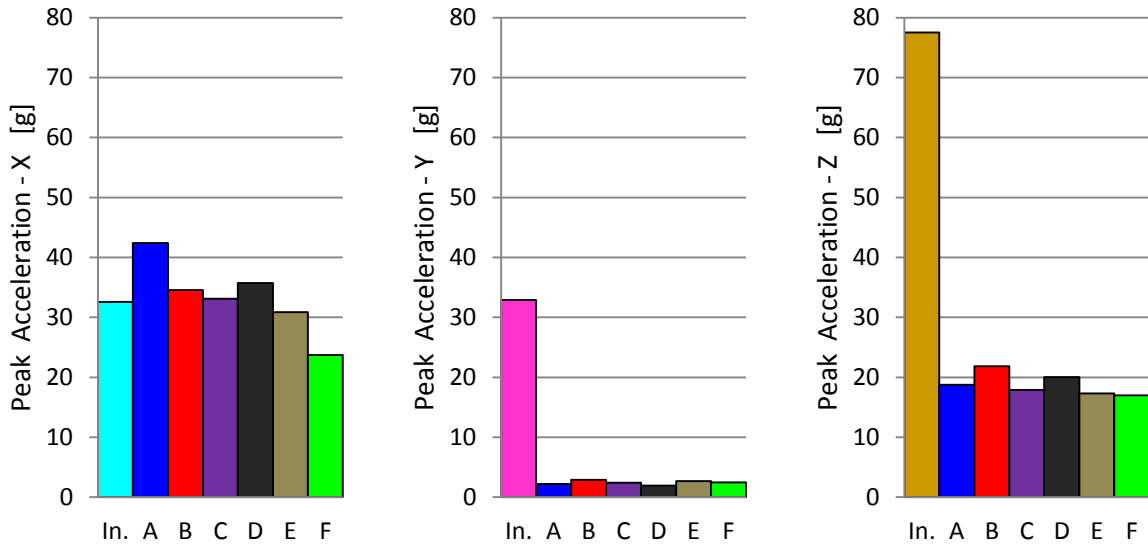


Figure 7-27. Maximum acceleration magnitudes of single battery using severe shock input

Similarly, simulations using the identical bump stop designs are performed with the typical shock input. Figure 7-28 shows the maximum accelerations of the typical input and battery CG responses. The SRS of the isolator designs for the typical shock input is also displayed in Figure 7-29.

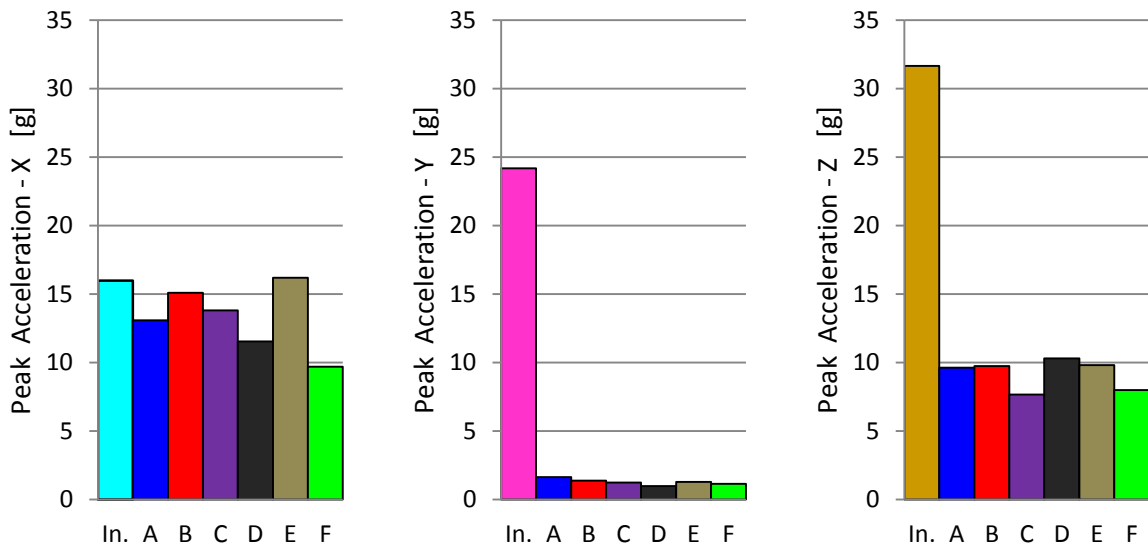


Figure 7-28. Maximum acceleration magnitudes of single battery using typical shock input

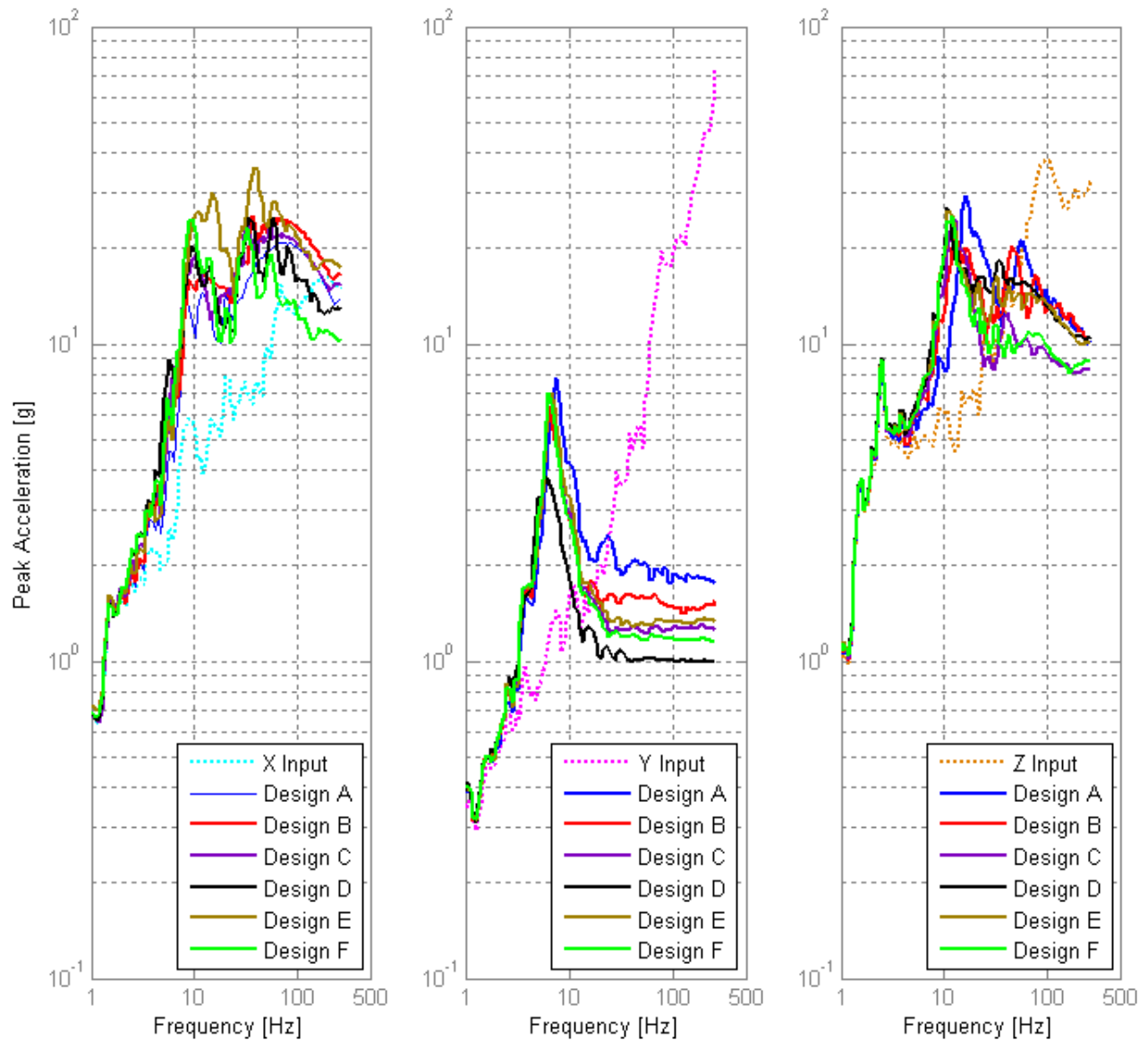


Figure 7-29. SRS of single battery isolator designs using typical shock input

As is shown, all suspension designs offer significant shock attenuation in the *Y* and *Z* directions. The *Y* direction offers the best attenuation of the three axes. In the *X* direction, however, shock attenuation is inconsistent between designs. Design A shows amplification of the *X* severe input. The typical and shock SRS figures show that the designs exhibit neither

shock attenuation nor amplification at very low frequencies ( $< 4$  Hz). As the frequency is increased, the responses begin to amplify the input signals. However, at sufficiently higher frequencies, shock attenuation becomes prevalent, particularly in the  $Y$  and  $Z$  directions. The performances of all isolator designs are rather similar. Design F, in general, seems to perform the best in all axes for typical and severe shock analysis.

Lastly, the isolator designs are simulated with the vibration tray input. A PSD of the simulation results is performed to analyze the effectiveness of the vibration isolation. Figures 7-30 through 7-32 show the PSD of the six designs in the  $X$ ,  $Y$ , and  $Z$  axes, respectively.

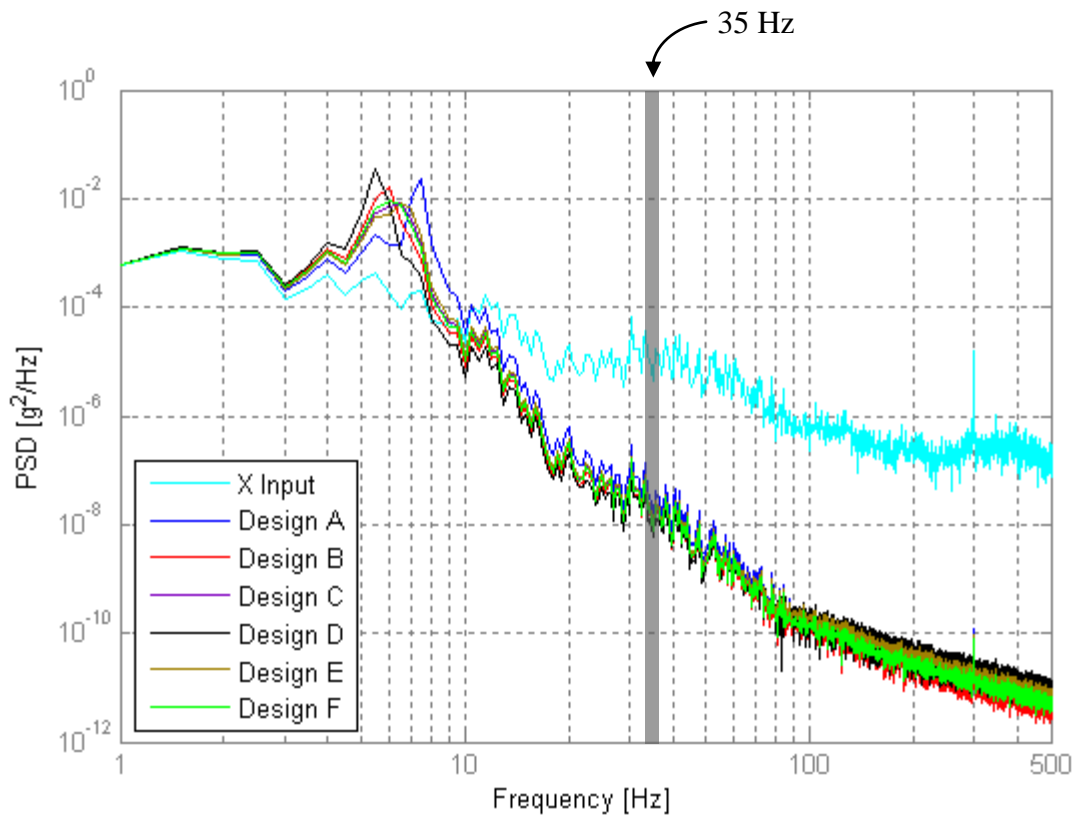


Figure 7-30. PSD of single battery vibration response in  $X$  direction

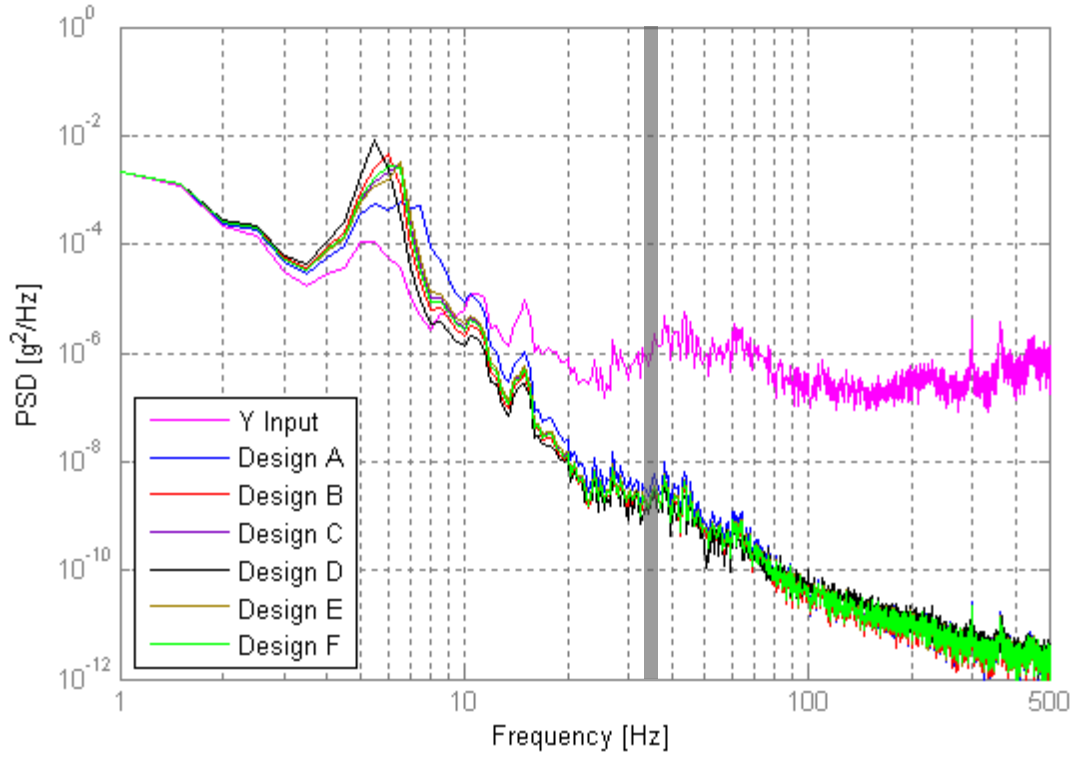


Figure 7-31. PSD of single battery vibration response in Y direction

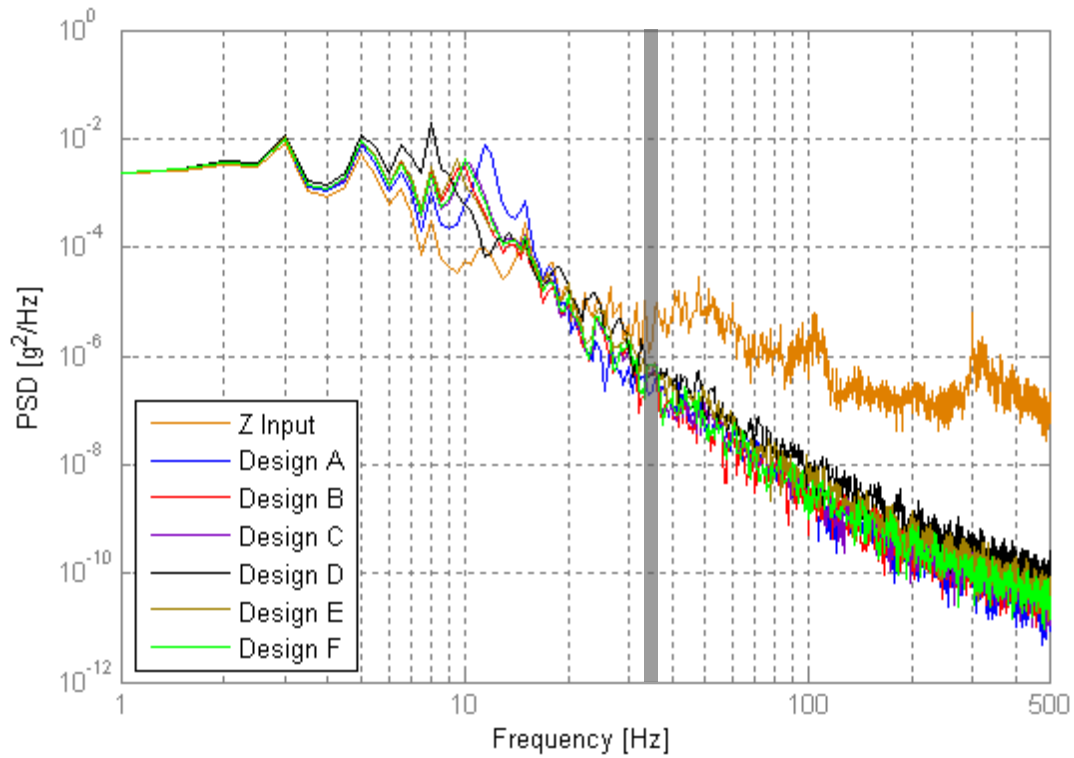


Figure 7-32. PSD of single battery vibration response in Z direction

From Figures 7-30 through 7-32, all isolator designs provide vibration isolation at 35 Hz. Approximately two to three orders of magnitude reduction in power density is achieved in the  $X$  and  $Y$  signals for all designs as compared to the input. Less isolation is seen in the  $Z$  direction, where roughly one order of magnitude reduction is exhibited. There is very little disparity between the PSD responses of the isolator designs; this vibration analysis alone is not sufficient to distinguish the best isolator design.

An exemplary time response of the vibration signal is shown in Figure 7-33. The battery CG acceleration response in the  $Z$  axes remains below 2 g in magnitude. All isolators exhibit very small deflections, and thus, the bump stops do not come into play. The mean compression of the isolators is not zero, illustrating the small amount of static compression from the battery's weight.

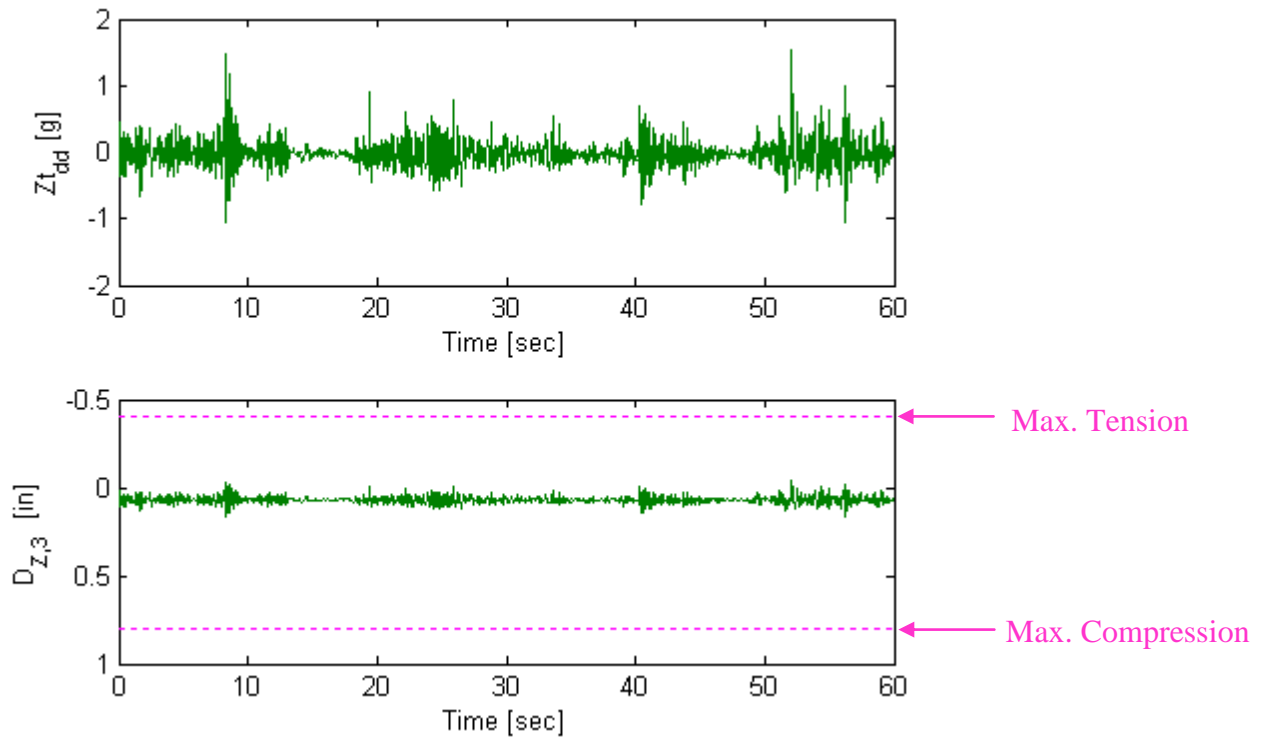


Figure 7-33. Time response of battery and isolators from vibration input

### 7.4.3 Bump Stop Design

From the studies presented for the single battery configuration isolator design, Design F appears to have the overall best performance. This design utilizes only four isolators (the least number across all designs) which best satisfies the low-cost requirements. Additionally, the M10-215 isolator has the greatest amount of travel capabilities of all designs. Design F is therefore used to simulate the preliminary bump stop design using BISCO silicone sheets.

Using the bump stop design procedure detailed in Section 7.1, multiple bump stop designs are dynamically feasible for Design F. One of these designs is presented here. The engage distances are chosen to be 50% of the isolator’s maximum travel in the roll deflection mode, and 75% in the compression and tension deflection modes. No bump stop is used at all for the left and right battery faces. The design goal is again to use adequately stiff BISCO silicone materials to minimize the area required to keep the suspension response within its dynamically-feasible limits.

The optimized bump stop design for Design F is shown in Figure 7-34. Table 7-4 details the design’s parameters.

Table 7-4. Optimized bump stop design for Design F

Direction	Engage	Material	Thickness [in]	# Sheets	Attachment Locations
X	50 %	HT-1250	1/8”	6	1, 5, 11, 15
Y	-	-	-	0	-
Top	75 %	HT-1250	1/8”	2	1, 5, 26, 30
Bottom	75 %	HT-1250	1/8”	3	1, 5, 26, 30

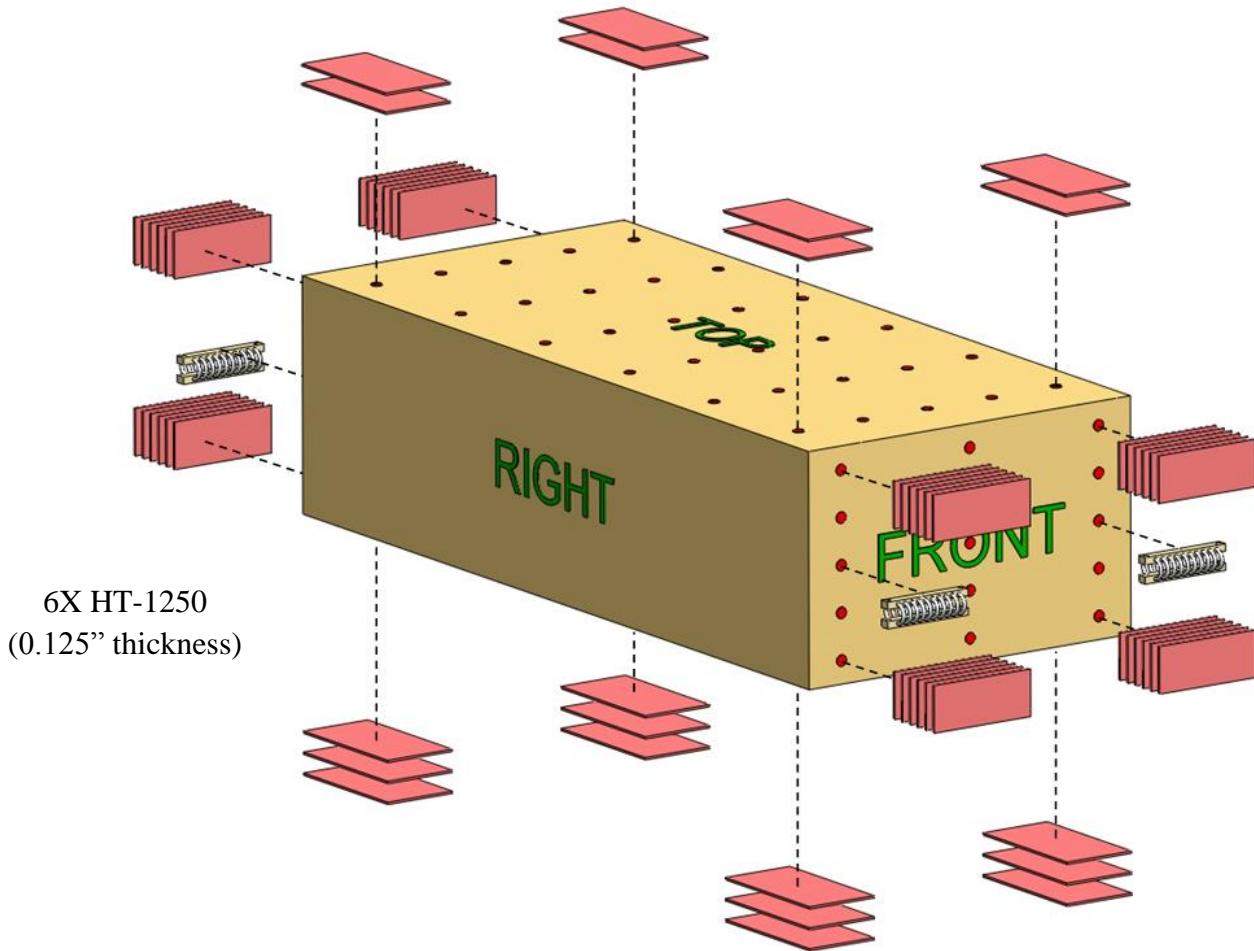


Figure 7-34. Bump stop design for Design F

## 7.5 Design Tradeoffs

Designing the Durathon Battery suspension system is a markedly complex process. There are many aspects of the design which require thorough consideration. The preliminary designs presented in this chapter meet the design requirements to various degrees, yet there are still additional parameters and concepts that should be explored. This section presents some of the fundamental tradeoffs that exist within the design, and more importantly, how they affect the

design requirements discussed in Chapter 2 such as performance, cost, and overall system complexity. The exemplary figures presented here are meant to aid in with tough design choices by first illustrating the tradeoff, and secondly discussing its implications on the design requirements.

### **7.5.1 Bump Stop Effective Thickness**

One tradeoff within the design that significantly affects performance of the suspension system is the effective thicknesses of the bump stops. The total amount of travel that the battery can undergo is directly determined by the wire rope isolators being used. The isolators have physical limitations on their deflections which consequently limit the battery's displacement. However, the amount of travel that the battery experiences before engaging a bump stop is not physically limited by either the isolator or bump stop material. Assuming that all of the isolator's available travel is utilized, the amount of clearance between battery and bump stop, or equivalently the bump stop *effective* thickness, is a tunable parameter of the system.

One way of analyzing bump stop performance is through the principle of mechanical work. The work done by a bump stop on the battery is equal to the area under the bump stop's force-deflection curve. Given an isolator design, this area is optimized to ensure that the isolators reach, but do not exceed their maximum deflections. The shape of the curve is tunable, however, by changing the stiffness and effective thickness of the bump stop. Figure 7-35 illustrates three linear bump stop designs that all have the same area under the curve, but different bump stop effective thicknesses.

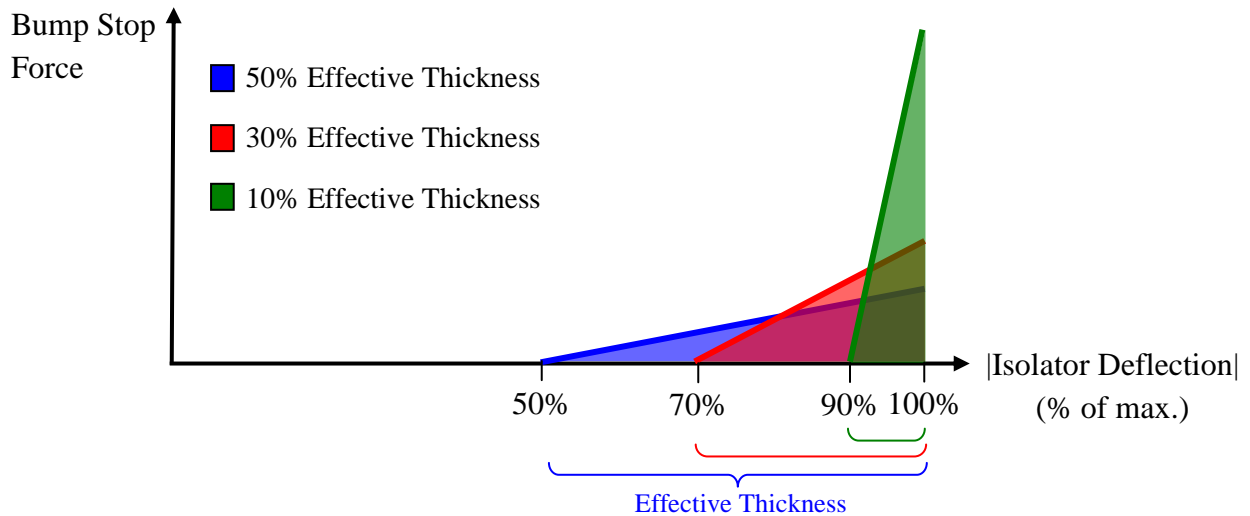


Figure 7-35. Variable bump stop effective thickness designs

The three bump stop designs in Figure 7-35 are incorporated with Design F of the single battery configuration, and each total system is simulated using the severe and typical shock inputs. The linear stiffness values of the three bump stops are tuned such that the isolators utilize their full range of motions. Figure 7-36 illustrates the SRS of the battery's X and Z responses to the severe shock input.

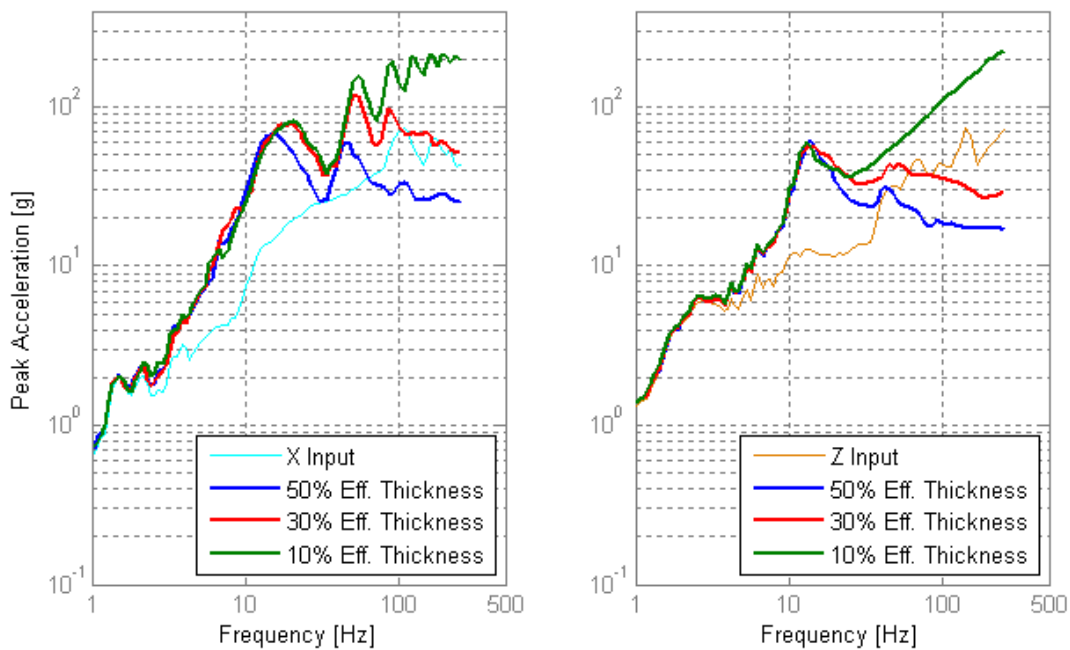


Figure 7-36. SRS using severe shock input for three bump stop designs

Figure 7-37 shows the SRS using the typical shock responses for the exact same designs.

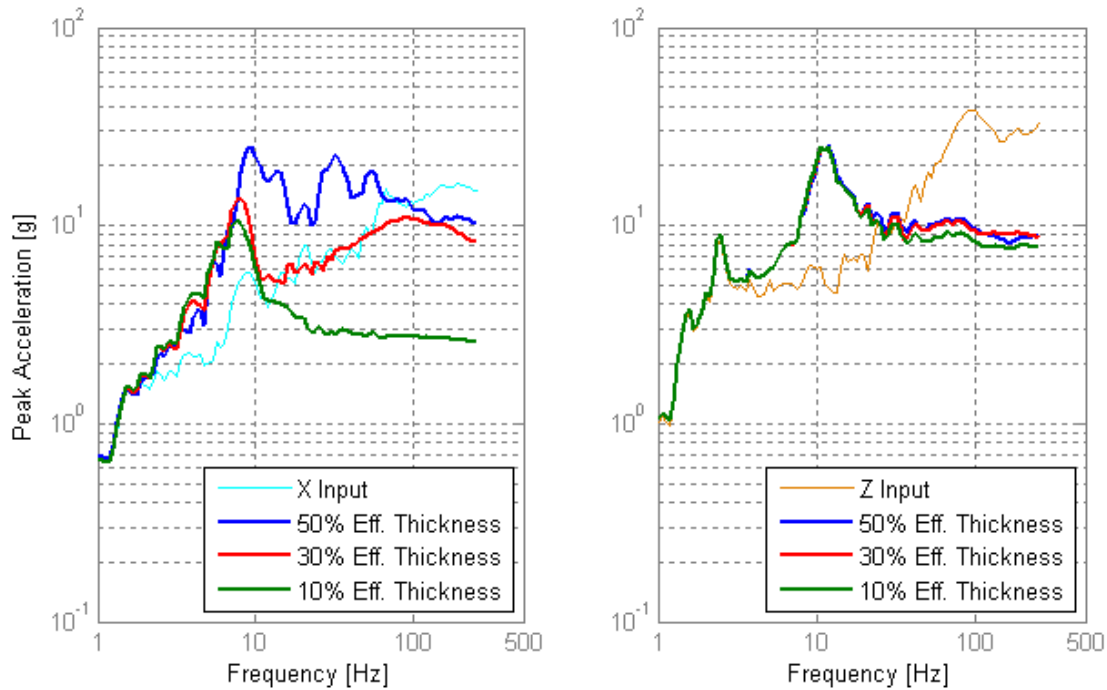


Figure 7-37. SRS using typical shock input for same three bump stop designs

These SRS figures demonstrate the tradeoff with bump stop effective thickness. The thinner bump stop designs have much higher SRS accelerations than the thicker designs for the severe shock input simulation. Conversely, the thinner designs show improved shock attenuation for the typical shock simulations. This behavior is explained as follows...

Because the bump stop has significantly higher stiffness than the wire rope isolators, engaging the bump stop at all drastically increases the force (and thus deceleration) acting on the battery. The magnitude of deceleration is related to the stopping distance / stopping time endured by the battery when coming to an instantaneous complete stop. Thicker bump stops have longer stopping distances which causes reduced deceleration magnitudes as compared to thinner bump stops.

On the other hand, as the bump stop effective thickness increases, the battery is more prone to making contact with the bump stop since the clearance gap is reduced. This explains why thicker bump stops actually hurt the battery response for typical shocks. The thinner bump stops are never contacted for these typical shocks which is why the 10% bump stop has significantly better performance in the X direction.

This tradeoff can be used to determine an optimal bump stop thickness for the design. If attenuating the severe shocks is the most critical design requirement, then a thicker bump stop is better. However, if reducing the average acceleration of the battery is imperative, then using a thinner bump stop is the better design choice. Thorough dynamic testing of the batteries is needed to determine which of these cases is more essential for battery performance and safety.

### **7.5.2 Supplementary Damping**

The amount of energy entering the tray is dependent on the vehicle's behavior during mining operations. The battery suspension system does not alter the tray's energy in any way but aims to distribute/absorb this energy in such a way to minimize harmful motion of the batteries. The spring behaviors of the isolators and bump stops convert energy between kinetic and potential forms, but only a small amount of energy is actually dissipated via the damping in the system. Increasing the system's damping by incorporating fluidic dampers, such as the one shown in Figure 7-38, can dissipate more of the tray's energy and prevent it from being transmitted to the batteries.



Figure 7-38. Example of a fluidic damper provided by Dorman Long Technology [41]

The effect of adding fluidic dampers to the system is investigated by using the 6DOF model. Design F of the single battery configuration is simulated four times using the severe shock input. Each time the overall damping ratio of the system is increased by 5%, 10%, 15%, and 25%, respectively. Figure 7-39 shows the resulting shock response spectrum of the battery's acceleration output in the X and Z directions.

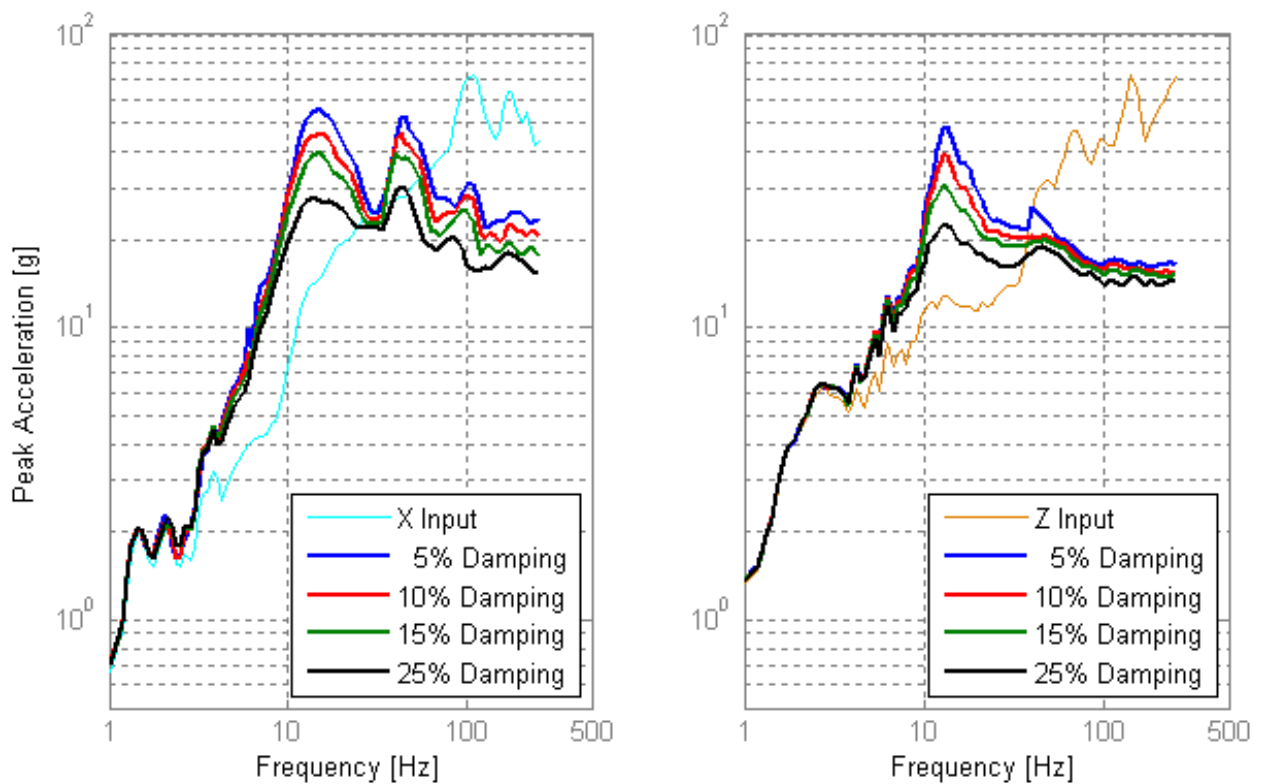


Figure 7-39. SRS of system response with additional damping

Figure 7-39 shows that the SRS peak accelerations decrease with increased damping. The biggest differences are seen at the resonant peaks. Response below 10 Hz is essentially identical for all damping levels.

The effect of increasing the system's damping is analyzed for the vibration tray input as well. Figure 7-40 shows that, contrary to the SRS responses, more damping actually hurts vibration isolation performance at 35 Hz in the *Y* direction. The resonant peak at 6 Hz is less for the 25% additional damping case, and remains so until the PSD curves intersect at roughly 9 Hz. Higher frequencies show that isolation is more effective for the 5% additional damping curve.

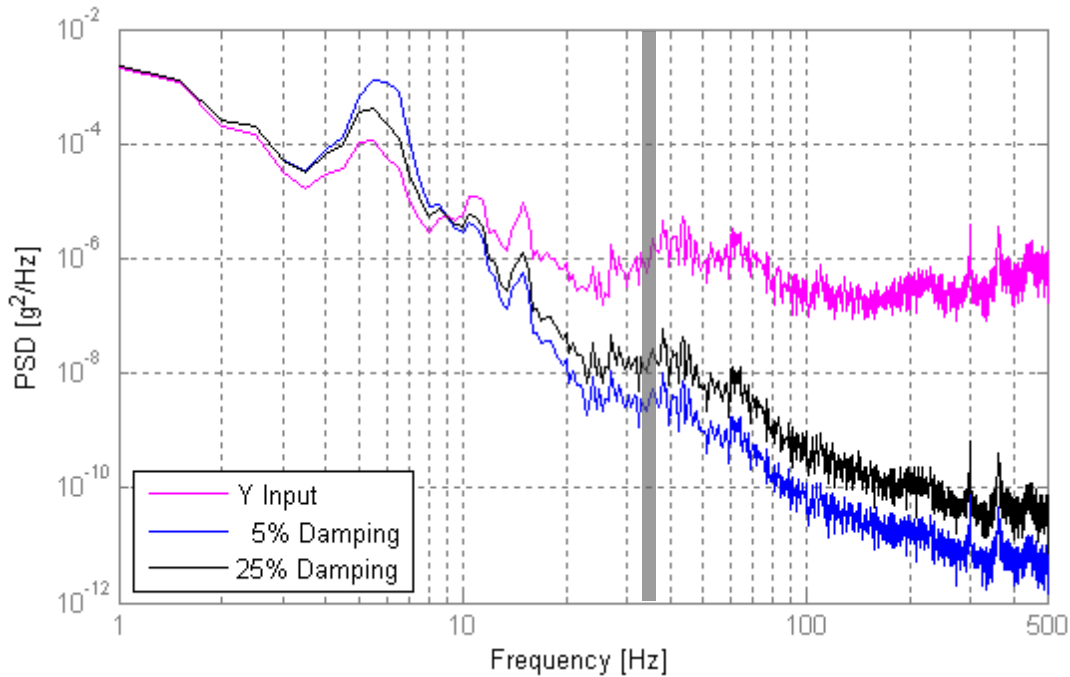


Figure 7-40. Vibration response with additional damping

Another drawback of adding fluidic dampers to the system is the increased cost and assembly complexity. Having more moving parts decreases system reliability and increases the probability of maintenance. Further analysis is needed to determine if the shock performance benefits warrant the extra cost and reduced vibration isolation associated with fluidic dampers.

### 7.5.3 Expanded Clearances

The final tradeoff that is investigated in this work is the sizes of the clearances between the batteries and carrier tray. The isolator designs are initially determined by the static requirements, one of them being the isolator dimensions which are constrained by the clearances of the system. If these clearances are not hard constraints, but can be slightly expanded, how will this possibly benefit the performance of the suspension system?

First it is assumed that the clearances can be increased to 4.5" in the *X* direction and 3" in the *Z* direction, keeping the lateral clearance at 1.5". With these slightly larger clearances, many new isolators are now available from Isolation Dynamics Corporation. One isolator size, for example, is M10-256-08. This has larger dimensions than any of the isolators already used, and also has larger travel capacities, with maximum deflections exceeding 1" in compression, roll, and shear.

The battery performance of a design using this isolator is simulated using typical and severe shock inputs. Eight isolators are required to support a single battery. Figures 7-41 and 7-42 illustrate the performance of this new design compared to the results obtained using Design F of the single battery configuration.

As the figures show, the new isolator design has significantly improved performance in the *X* direction for both typical and severe shocks. There is not much disparity in the *Y* direction, and some improvement is exhibited in the *Z* direction for severe shocks. This behavior is explained because the stiffness and isolator clearances of the new design are at a ratio such that the isolators alone constitute a dynamically-feasible design. The design does not utilize any bump stops and the battery performance is consequently much. This quick study illustrates that

slightly expanding the system's clearances opens the door for more suitable isolator designs which can drastically enhance shock attenuation.

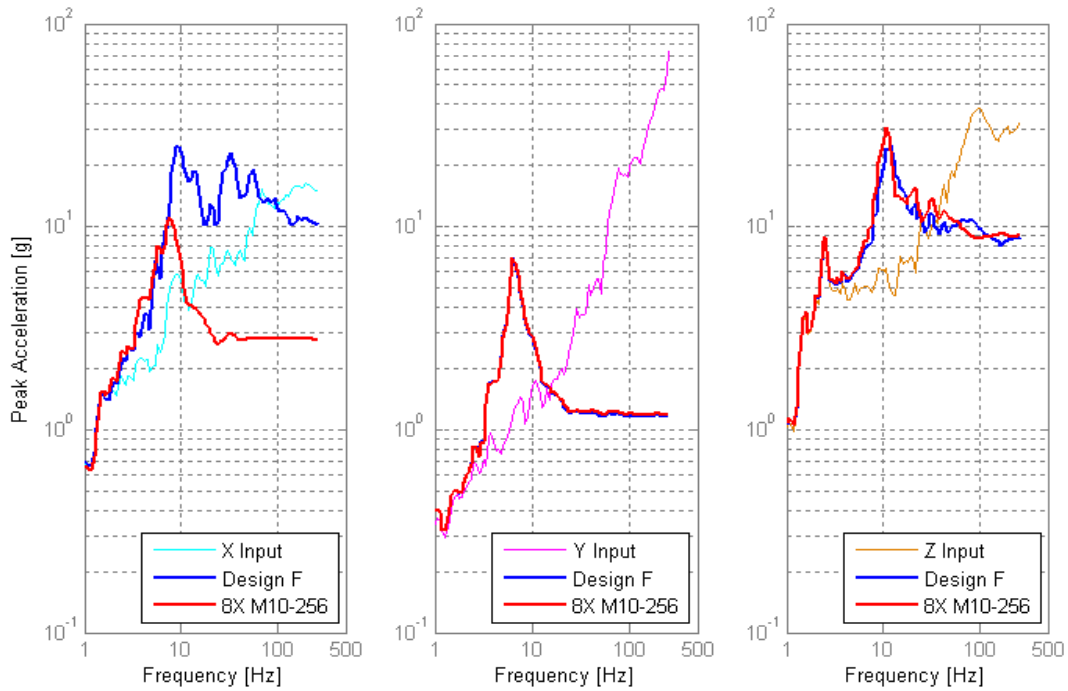


Figure 7-41. SRS expanded clearance design using typical shock input

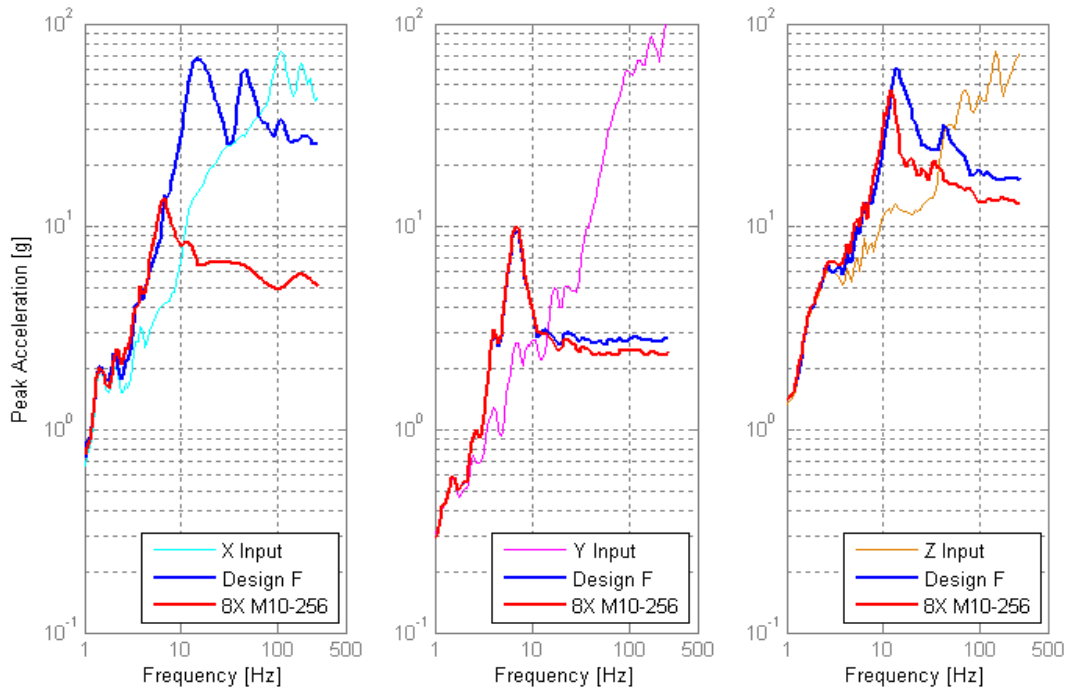


Figure 7-42. SRS of expanded clearance design using severe shock input

## 7.6 Discussion

The use of the 6DOF dynamic model has shed light on the feasibility, effectiveness, and tradeoff considerations of various suspension designs. Two assembly configurations are investigated using wire rope isolators. For each configuration, six different isolator designs are statically feasible. Bump stops composed of silicone materials are incorporated such that they protect both the battery and isolators during shock events. This approach yields a two-phase, nonlinear suspension design with multiple tuning parameters. From the simulation results presented in this chapter, several conclusions are drawn.

All of the wire rope isolator designs that meet the geometric and static load requirements effectively satisfy the vibration requirements of the battery. The battery experiences between one and three orders of magnitude reduction in power spectral density for frequencies at and above 35 Hz. All of the isolator designs achieve comparable isolation characteristics because the natural frequency of each system is very similar. Figure 7-43 shows the vibratory natural frequencies of the six isolator designs for the single battery configuration. As depicted, the natural frequencies of each design are within 3 Hz in the compression, tension, and shear deflection modes. This is driven by the fact that wire rope isolators have a recommended static load range which keeps the feasible system natural frequencies within a small range. It is therefore expected that each system undergoes amplification at similar resonant frequencies and subsequent vibration isolation at higher frequencies. Vibration analysis alone is not sufficient for selecting the best isolator design; the designs must instead be differentiated via shock response analyses.

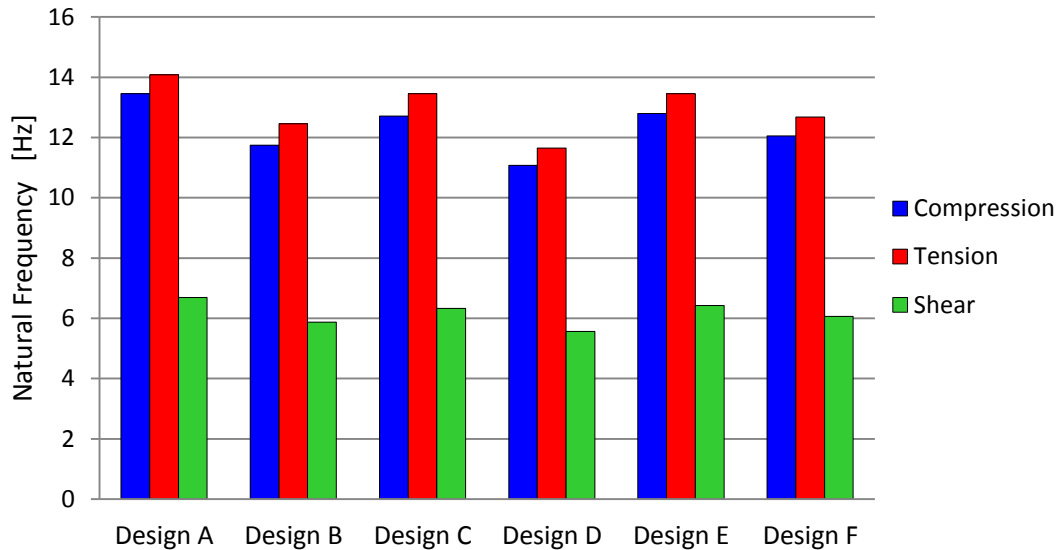


Figure 7-43. Vibratory natural frequencies of single battery isolator designs

Unlike the vibration responses, larger performance discrepancies are indeed illustrated in the isolator designs' abilities to provide shock attenuation. As previously discussed, the natural frequency of each system is similar because of the restriction on isolator static load. The combinations of number of isolators and stiffness do not define unique design characteristics. A distinguishing characteristic between designs is the maximum rated travel of each isolator size. As shown in Figures 7-2 and 7-21, different isolator sizes can have significantly different travel capabilities. The shock response results for both assembly configurations illustrate that isolators with more allowable deflection, such as the M10-215 isolator, tend to give better shock attenuation because the battery displaces a larger distance. These designs utilize more of the available clearances, and as a result, achieve more gradual decelerations. Design A for both configurations generally exhibited the worst shock attenuation. This design is comprised of M6-120 isolators, which unsurprisingly have the smallest amount of allowable travel out of all of the simulated isolators. From basic shock theory, shock attenuation is directly related to

displacement, where larger displacements yield better attenuation responses. The clearances between battery and tray are rather tight to begin with, so it is advantageous to use isolator designs that utilize as much of these clearances as possible. This conclusion is further supported by the clearance tradeoff study in Section 7.5.3. Larger clearances / larger isolator displacements allow for vast improvement in shock performance.

Furthermore, Section 7.5 illustrates that bump stop effective thickness is a critical design parameter. This parameter (or equivalently the engage distance between battery and bump stop) proportions the shock attenuation capabilities between typical and severe shocks. Severe shock attenuation is improved with thicker bump stops and shorter engage distances. The penalty of this type of design is that bump stops are utilized more frequently for milder shock events. The average accelerations experienced by the battery over time are consequently increased. If more clearance is incorporated between the battery and onset of the bump stops, then it is more probable that typical shocks are attenuated without bump stop contact, and the average accelerations of the battery over time decrease. However, when a severe shock input does occur in this type of design, the attenuation is much worse since bump stop effective thickness is so small. Therefore, the question is posed whether it is more essential to reduce the maximum accelerations of the battery (by using shorter engage distances) or to minimize the average accelerations of the battery over time (by using longer engage distances). This question must be answered through battery testing which can solidify the survivability requirements. Once the battery requirements are better understood, the effective thickness of the bump stops can be better designed.

Finally, damping has been investigated throughout the design process. Adding damping to the system by using a dissipation mechanism such as a fluidic damper improves the shock

attenuation as shown in Section 7.5.2. The resonant peaks in the shock response spectrums, in particular, are greatly reduced with increased system damping. Vibration isolation, on the other hand, decreases when more damping is used. Again, battery testing is required to establish isolation and shock attenuation standards that must be satisfied. These will determine if the system responses utilizing fluidic damping are both necessary and warranted to offset to added cost and complexity.

## **CHAPTER 8**

### **CONCLUSION**

With the recent growth of off-road BEVs, the need for sophisticated battery pack suspensions is more prevalent than ever. Suspension design for battery packs is a complex process; the battery's environment is often much harsher than typical battery applications and thus there tends to be more design requirements and constraints. Vibration and shock loading transferred from the vehicle create multi-directional base accelerations encompassing a wide range of frequencies and amplitudes. Furthermore, large battery packs are extremely heavy and pose static-support challenges. Given the tight clearances typically available between the vehicle and its battery pack, designing a compact system that is both functional and cost-effective proves to be a difficult task.

The suspension designs presented in this work offer potential solutions for ensuring long life of many BEV battery packs. These designs integrate wire rope isolators and silicone bump stops that constitute two-phase, passive suspension systems. Both classes of materials are able to operate reliably in extreme environments without sustaining damage. The two-phase approach yields versatility in suspension performance by partially decoupling the vibration and shock behaviors of the battery pack.

Wire rope isolators prove to be effective products for this application because they offer multi-axial stiffness characteristics in a compact size. High stiffness of the compression mode allows for the support of large static loads without requiring many isolators. These products also inherently dissipate energy which aids with shock attenuation, again minimizing the complexity and overall cost of the suspension. Two installation methods have been successfully demonstrated, showing versatility for many battery pack configurations.

Silicone bump stops are installed to combat shock impacts. Their thickness, area, and material properties can be adjusted to obtain optimal shock attenuation characteristics. By utilizing clearance between the bump stops and battery pack, bump stop design does not affect the vibration behavior of the battery pack. In conventional, single-phase suspensions, increasing the system's overall stiffness to mitigate transient shock disturbances always compromises vibration isolation. However, these suspension designs allow for low natural frequencies suitable for excellent vibration isolation and also amplitude-dependent stiffness gains for enhanced shock attenuation.

The suspension design has successfully demonstrated vibration isolation and shock attenuation for an underground mining vehicle battery pack; however, the tunable capabilities of the design allow it to be applied to many other battery pack systems. Wire rope isolators are sold in many sizes that can support a variety of battery packs. The behaviors of silicone bump stops can be optimally adjusted by simply changing the material, thickness, and area used. This thesis has illustrated that the two-phase, passive suspension can be an effective solution for ensuring long life of battery packs and may assist in the implementation of battery packs on off-road BEVs in the years to come.

## REFERENCES

- [1] Benefits and Considerations of Electricity as a Vehicle Fuel. (n.d.). *US Department of Energy*. Retrieved February 27, 2014, from [http://www.afdc.energy.gov/fuels/electricity\\_benefits.html](http://www.afdc.energy.gov/fuels/electricity_benefits.html)
- [2] Rahn, C. D., & Wang, C. (2013). *Battery systems engineering*. Chichester: Wiley.
- [3] Shadow Reconnaissance, Surveillance, Targeting Vehicle (RST-V). (n.d.). *Army-Technology*. Retrieved February 28, 2014, from <http://www.army-technology.com/projects/shadow/>
- [4] Greener underground mining - Electric vehicles lead the way. (n.d.). *Mineweb*. Retrieved February 27, 2014, from <http://www.mineweb.com/mineweb/content/en/mineweb-technology?oid=187840&sn=Detail>
- [5] Muckmaster 300EB Evolution. (2014). *RDH Mining Equipment*. Retrieved February 27, 2014, from <http://www.rdhminingequipment.com/New-Products.page?CategoryID=38383&CurrentPage=1&ItemID=191844>
- [6] Doughty, D., & Roth, E. P. (2012). A General Discussion of Li Ion Battery Safety. *The Electrochemical Society*. Retrieved February 27, 2014, from [https://www.electrochem.org/dl/interface/sum/sum12/sum12\\_p037\\_044.pdf](https://www.electrochem.org/dl/interface/sum/sum12/sum12_p037_044.pdf)
- [7] *2004 SAE handbook*. (2004). Warrendale, PA: Society of Automotive Engineers.
- [8] Doughty, D., (2010). SAE J2464 "EV & HEV Rechargeable Energy Storage System (RESS) Safety and Abuse Testing Procedure", SAE Technical Paper 2010-01-1077
- [9] Karnopp, D. (1995) Active and Semi-Active Vibration Isolation. *Journal of Mechanical Design*, 117(B), 177-185.
- [10] Jazar, R. N. (2008). *Vehicle dynamics theory and applications*. New York: Springer.
- [11] Air Springs and Air Shock Absorbers. (n.d.). *ITT Enidine*. Retrieved April 8, 2013, from <http://www.enidine.com/Industrial/Airsprings.html>
- [12] Nichols, K. E., (1959) "New Trends in Using Air Suspension," *Engineering Materials and Design*, 371.
- [13] Esmailzadeh, E. (1978). Optimization of pneumatic vibration isolation system for vehicle suspension. *Journal of Mechanical Design*, 100(3), 500-506.
- [14] 32k Fifth Wheel Air Hitch. (n.d.). *Air Safe Hitches*. Retrieved February 27, 2014, from <http://www.airsafehitches.com/32k.html>

- [15] gStreet Air-Spring Suspension. (n.d.). *Chassisworks, Inc.*. Retrieved February 27, 2014, from <http://www.cachassisworks.com/c-288-air-spring-suspensions.aspx>
- [16] Air Suspension. (n.d.). *The Car Suspension Bible*. Retrieved February 27, 2014, from [http://www.carbibles.com/suspension\\_bible\\_pg3.html](http://www.carbibles.com/suspension_bible_pg3.html)
- [17] Yu, Y., Naganathan, N. G., & Dukkipati, R. V. (2001). A literature review of automotive vehicle engine mounting systems. *Mechanism and Machine Theory*, 36(1), 123-142.
- [18] Mosher, M. W. (n.d.). Reduction of Shock Response Spectra. *Taylor Devices, Inc.*. Retrieved March 4, 2014, from <http://taylordevices.com/spectra.html>
- [19] Blair, M. & Sills, J. (1994). *Application of foam isolation systems in satellite orbital transportation*. Proc. of the 12th International Modal Analysis Conference, 1662-1669.
- [20] Ibrahim, R. (2008). Recent advances in nonlinear passive vibration isolators. *Journal of Sound and Vibration*, 314(3-5), 371-452.
- [21] Demetriades, G., Constantinou, M., & Reinhorn, A. (1993). Study of wire rope systems for seismic protection of equipment in buildings. *Engineering Structures*, 15(5), 321-334.
- [22] Karnopp, D., Crosby, M. J., & Harwood, R. A. (1974). Vibration Control Using Semi-Active Force Generators. *Journal of Engineering for Industry*, 96(2), 619-626.
- [23] Choi, Y., Jeon, Y., & Wereley, N. (2005). Semi-Active Vibration Isolation Using Magnetorheological Isolators. *Journal of Aircraft*, 42(5), 1244-1251.
- [24] Choi, Y., Brigley, M., & Wereley, N. (2005). Vibration isolation of precision payloads for aerial vehicles using magnetorheological isolators. Proc. of the International Design Engineering Technical Conference
- [25] Isa, H., Mahadi, W., Ramli, R., & Abidin, M. (2011). *A review on electromagnetic suspension systems for passenger vehicle*. Paper presented at International Conference on Electrical, Control and Computing Engineering, Pahang, Malaysia. 399 - 403
- [26] GE Durathon Batteries Successfully Power Underground Mining Scoop. (2013). *Green Car Congress*. Retrieved December 29, 2013, from <http://www.greencarcongress.com/2013/09/20130912-ge.html>
- [27] GE's Fairchild Mining Equipment - Products. (2013). *GE's Fairchild Mining Equipment*. Retrieved December 29, 2013, from <http://www.fairchildint.com/products.php>
- [28] Frutschy, K., Chatwin, T., Mao, L., Smith, C., & Bull, R. (2012). *Sodium nickel chloride battery design and testing*. Paper presented at ASME 2012 International Mechanical Engineering Congress and Exposition, Houston, Texas. 429-438.

- [29] Wire Rope Isolators. (n.d.). *ITT Enidine*. Retrieved April 8, 2013, from <http://www.enidine.com/Industrial/Airsprings.html>
- [30] Collins, M. J. (1996). *U.S. Patent No. 5,549,285*. U.S. Patent and Trademark Office.
- [31] CAVOFLEX. (2013). *Anti-Vibration Methods*. Retrieved January 3, 2014, from <http://www.antivibrationmethods.com/product/cavoflex>
- [32] M Series Literature Library. (2008). *Isolation Dynamics Corp*. Retrieved July, 16 2013, from [http://www.isolator.com/m\\_series\\_isolators.html](http://www.isolator.com/m_series_isolators.html)
- [33] BISCO Silicones. (2013). *Rogers Corporation*. Retrieved August 1, 2013, from <http://www.rogerscorp.com/hpf/bisco/index.aspx>.
- [34] Cai, Y., & Zhang, C. (2011). Mechanical damping properties of silicone rubber prepared by nano-SiO<sub>2</sub> and AGE-Modified polysiloxane blends. *Advanced Materials Research* 337, 41-45.
- [35] Silicone Foam Sheet. (n.d.). *Fullchance Rubber Sheet Roll*. Retrieved January 8, 2014, from [http://www.rollsheetrubber.com/html\\_1.aspx?id=544](http://www.rollsheetrubber.com/html_1.aspx?id=544).
- [36] Ni, Y., Wong, C., & Ko, J. (1996). *Modeling the unsymmetric hysteretic loops of friction-type isolators*. Proc. of 14th International Modal Analysis Conference. 1579-1585.
- [37] Tinker, M., & Cutchins, M. (1992). Damping phenomena in a wire rope vibration isolation system. *Journal of Sound and Vibration*, 157(1), 7-18.
- [38] McConnell, K. G. (1995). *Vibration testing: theory and practice*. New York: Wiley.
- [39] Stevens, B. L., & Lewis, F. L. (1992). *Aircraft control and simulation*. New York: Wiley.
- [40] MIL-STD 810G, Method 516.6. (2008). *Environmental Considerations and Laboratory Tests*. 365-423
- [41] DLT Viscous Dampers and Lock-up Devices. *Dorman Long Technology Product Page*. Retrieved July 1, 2014, from <http://www.dormanlongtechnology.com/en/Products/DL-VD.htm>

## **APPENDIX A – MODEL VALIDATION**

The study of battery pack suspensions presented in this thesis uses an entirely computer-based approach. Simulation results of the 6DOF dynamic model, which rely on the properties of wire rope isolators and silicone sheets taken from vendor catalogs, pave the way for determining feasible suspension designs. In the absence of experimental testing of a real suspension, it is uncertain to what degree of accuracy the model predicts true dynamic behavior of a battery. Some of the assumptions and simplifications implemented into the model will not be properly validated until prototype testing commences. However, steps have been taken to compare the model's simulation results with other non-experimental means. While this approach does not verify the assumptions within the model, it does provide confidence that the model's governing equations are correctly derived and implemented into MATLAB.

### **A.1 SDOF Analytical Equations**

The first form of model validation is using the analytical equations for a linear single degree-of-freedom (SDOF) mass-spring-damper system. These equations describe a system that has one mass (no inertia) translating along a single axis. The mass is attached to a base by a linear spring and linear damper. This SDOF system can replicate the behavior of the single battery configuration if a few simplifications are made to the 6DOF dynamic model. First, no bump stops are used because they cause the battery's behavior to be inherently nonlinear. Next, the wire rope isolators are installed symmetrically about the battery CG such that no battery rotation occurs. Finally, the viscous damping in the model achieves a 5% damping ratio throughout the isolators' entire range of motion and does not characterize the piecewise damping

shown in Section 4.3. By making these simplifications to the 6DOF model, the single battery configuration should behave identically to a linear SDOF system.

A free response simulation is used to compare the results between the SDOF analytical system and the simplified 6DOF single battery model. There is no input to the system, but nonzero initial conditions are applied to the displacement and/or the velocity of the mass. The second order differential equation of a SDOF system with viscous damping and zero input is given by

$$m\ddot{x} + c\dot{x} + kx = 0 \quad (\text{A-1})$$

where the undamped and damped natural frequencies are given by equations A-2 and A-3, respectively.

$$\omega_n = \sqrt{\frac{k}{m}} \quad (\text{A-2})$$

$$\omega_d = \omega_n \sqrt{1 - \zeta^2} \quad (\text{A-3})$$

The damping ratio is calculated as

$$\zeta = \frac{c}{2\sqrt{km}} \quad (\text{A-4})$$

The free response solution for an underdamped system ( $0 < \zeta < 1$ ) with initial conditions  $x_0$  and  $v_0$  is given as

$$x(t) = X e^{-\zeta \omega_n t} \cos(\omega_d t - \phi) \quad (\text{A-5})$$

where the 0-peak amplitude is

$$X = \sqrt{\left(\frac{v_0 + \zeta \omega_n x_0}{\omega_d}\right)^2 + x_0^2} \quad (\text{A-6})$$

and the phase is

$$\phi = \tanh^{-1}\left(\frac{v_0 + \zeta \omega_n x_0}{\omega_d x_0}\right) \quad (\text{A-7})$$

The free responses using the simplified single battery configuration and analytical equations are simulated using the properties listed in Table A-1. For the single battery configuration, four M10-215 wire rope isolators are installed symmetrically about the battery CG (shown in Figure 7-34) so the battery does not rotate. The initial conditions for the battery moving along the  $X$  axis are the 1<sup>st</sup> and 7<sup>th</sup> elements in the state vector at  $t=0$ . Figure A-1 illustrates the free responses using both the SDOF analytical equations and the 6DOF single battery model after the previously described simplifications have been applied.

Table A-1. Free response system properties for analytical comparison

SDOF Analytical Equations			Simplified Single Battery Configuration (4X M10-215 Isolators)		
Parameter	Value	Unit	Parameter	Value	Unit
$m$	412	kg	$m$	412	kg
$c$	1642	N-s/m	$c_{s, shear}$	410.5	N-s/m
$k$	654272	N/m	$k_{s, shear}$	163568	N/m
$\zeta$	0.05	-	$\zeta$	0.05	-
$x_0$	0.018	m	$x_0(1)$	0.018	m
$v_0$	0	m/s	$x_0(7)$	0	m/s

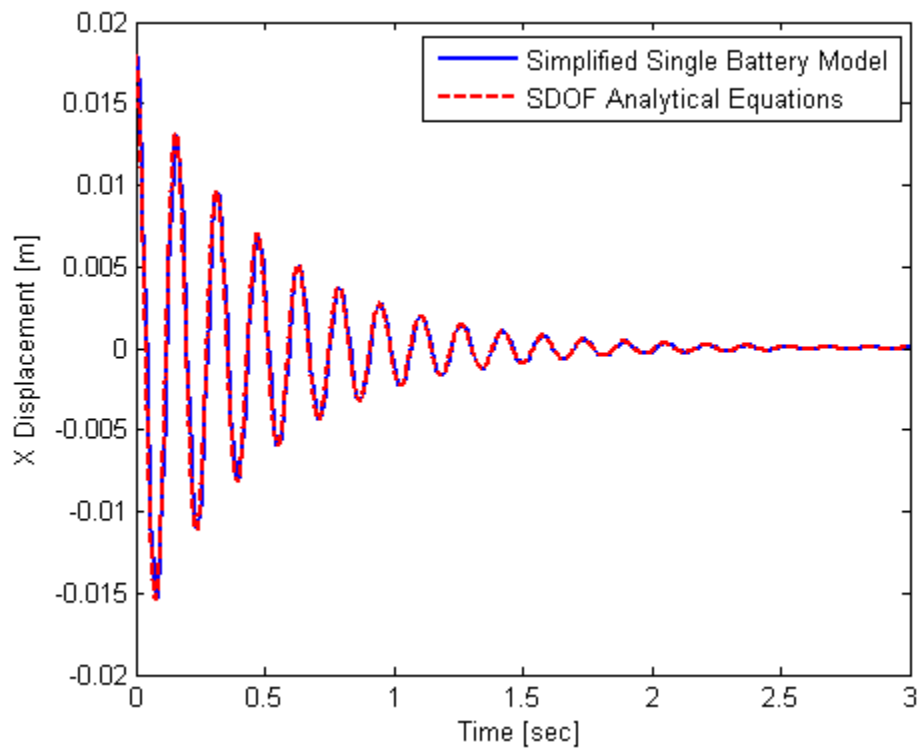


Figure A-1. Free responses using SDOF analytical equations and simplified 6DOF model

Figure A-1 shows excellent agreement between the analytical equations and the simplified 6DOF model. Both the exponential decay rate and the frequency of oscillation are perfectly aligned. This free response study indicates that the equations of motion for the translational dynamics of the battery are correctly derived and properly implemented into MATLAB.

## A.2 SolidWorks Motion Study

The second form of model validation utilizes SolidWorks Motion Study. In this 3D computer-aided design (CAD) package, the tray and battery are modeled as rigid bodies. The motion of the tray is prescribed using linear motors where accelerations are specified. The density of the battery's material is customized such that the battery's mass, inertia, and volume match the properties used in the 6DOF dynamic model. Spring elements are attached between the inner tray walls and the battery surface. These elements possess linear stiffness and linear viscous damping characteristics. At each attachment point, three springs are used to capture stiffness and damping in three directions simultaneously (to match the multi-axial behavior of wire rope isolators). Figure A-2 shows the battery-tray system modeled in SolidWorks.

3 Spring/Damper Elements

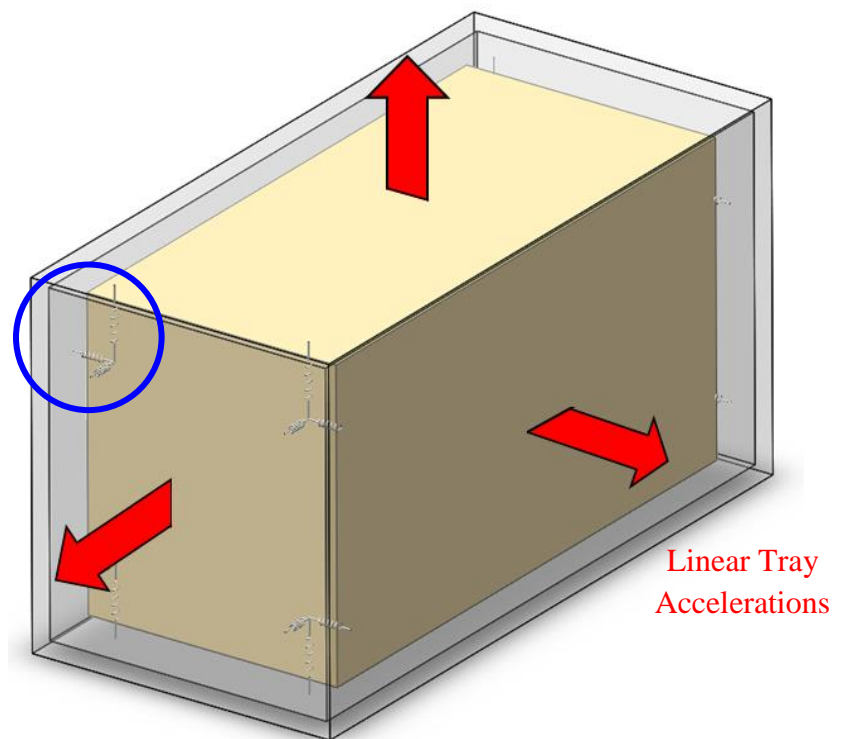
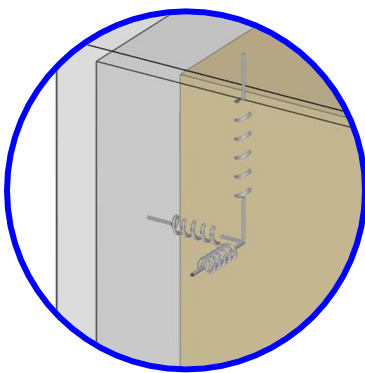


Figure A-2. Battery-tray system modeled in SolidWorks Motion Study

A few simplifications are made to the 6DOF MATLAB model in order to match its simulation results with the SolidWorks Motion Study results. SolidWorks can only incorporate linear springs and dampers; therefore, the damping in the MATLAB model is changed to a constant damping ratio, independent of isolator deflection. Bump stops are not utilized as well since these exhibit nonlinear forces. In addition, the tensile and compression spring rates of the isolators are assumed to be identical. These simplifications allow the SolidWorks results to validate the dynamic model.

A verification study uses a half sine acceleration pulse as the tray input. Figure A-3 shows the acceleration input. This pulse is applied independently in the X, Y, and Z directions.

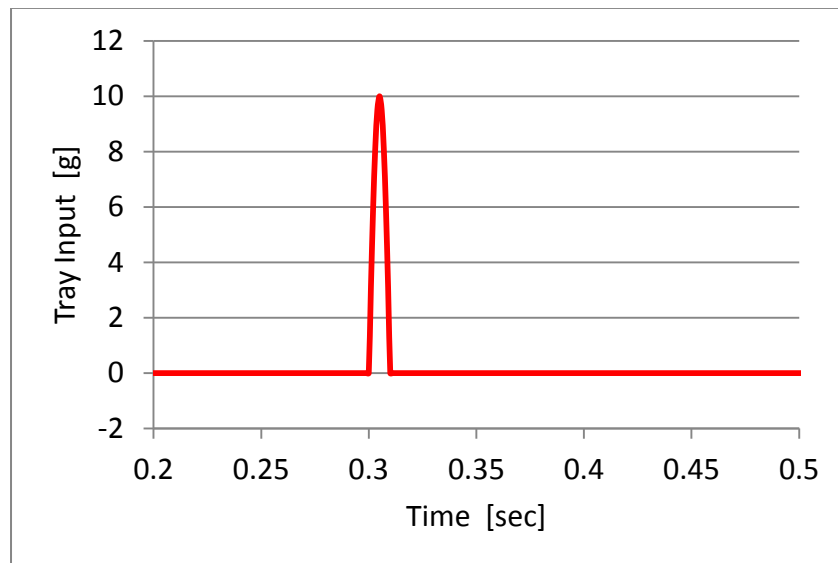


Figure A-3. Half sine acceleration pulse for SolidWorks Motion Study validation

Using this input, the results of the 6DOF stacked battery configuration model in MATLAB and the SolidWorks model are compared. The stacked battery configuration uses spring and damper elements underneath the bottom battery face which induces battery rotation.

Figures A-4 and A-5 display the acceleration response of the battery CG in the Y and Z directions, respectively, when exposed to the pulse input in Figure A-3.

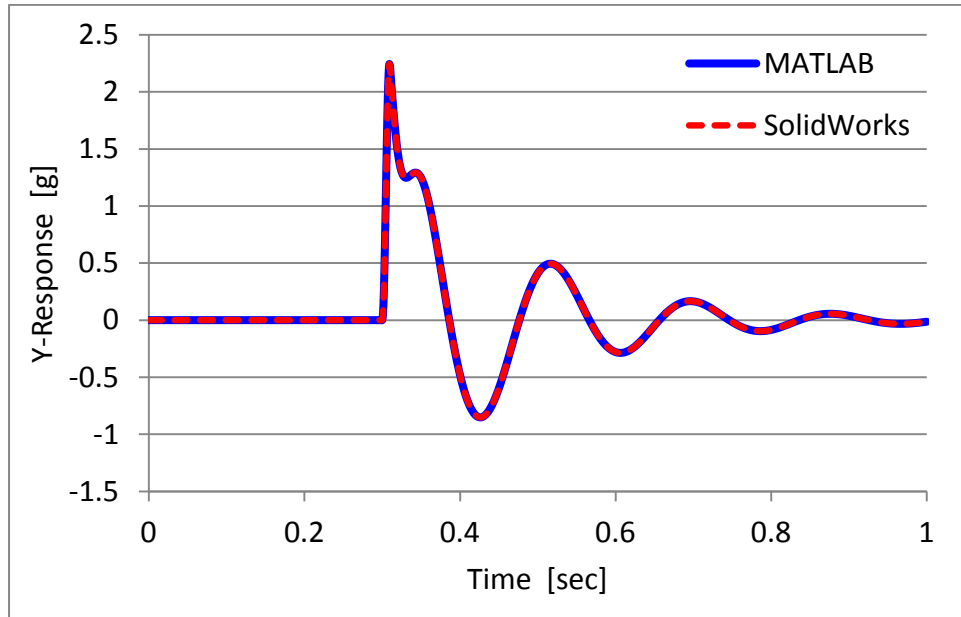


Figure A-4. Pulse response in Y direction using SolidWorks and linear 6DOF MATLAB models

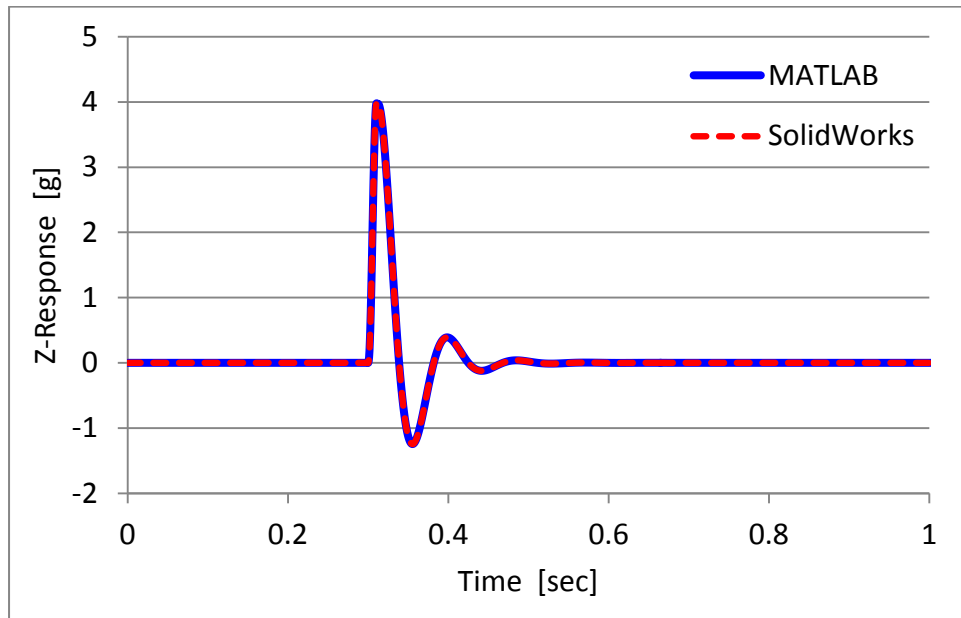


Figure A-5. Pulse response in Z direction using SolidWorks and linear 6DOF MATLAB models

Figures A-4 and A-5 show that the SolidWorks and MATLAB models agree very well. The shape of the response in the  $Z$  direction resembles that of a SDOF system, since no rotation occurs for an input solely in the  $Z$  direction (the battery is symmetrically supported from underneath). The initial amplitude, decay rate, and frequency of oscillation are identical for both the SolidWorks and MATLAB results. Similarly, the  $Y$  direction responses are perfect matches as well. The shape of Figure A-4 does not resemble a SDOF pulse response since some rotation does occur about the longitudinal axis. The validation procedure using SolidWorks Motion Study gives confidence that both the linear translational and rotational equations in the 6DOF MATLAB model are indeed correctly implemented.

## **APPENDIX B – MATLAB FILE STRUCTURE**

The 6DOF dynamic model is implemented in MATLAB. This software offers complete control of the incorporation of model complexities and versatility in the analysis of the results. It also allows for a modular file structure by easily interchanging input data, wire rope isolator sizes, and bump stop design, as each is represented by an independent function file. This setup facilitates expedient tuning of the designs.

The structure of the model consists of one simulation script file and multiple functions corresponding to tray inputs, battery dynamics, bump stop dynamics, and analysis tools. Three .mat data files are used as well which contain samples of accelerometer test data describing the three tray inputs discussed in Chapter 6. A diagram of every file of the model is shown on the next page in Figure B-1. Table B-1 and Figure B-2 depict a flow chart of the model. Detailed descriptions of each of these files are provided in Appendix C.

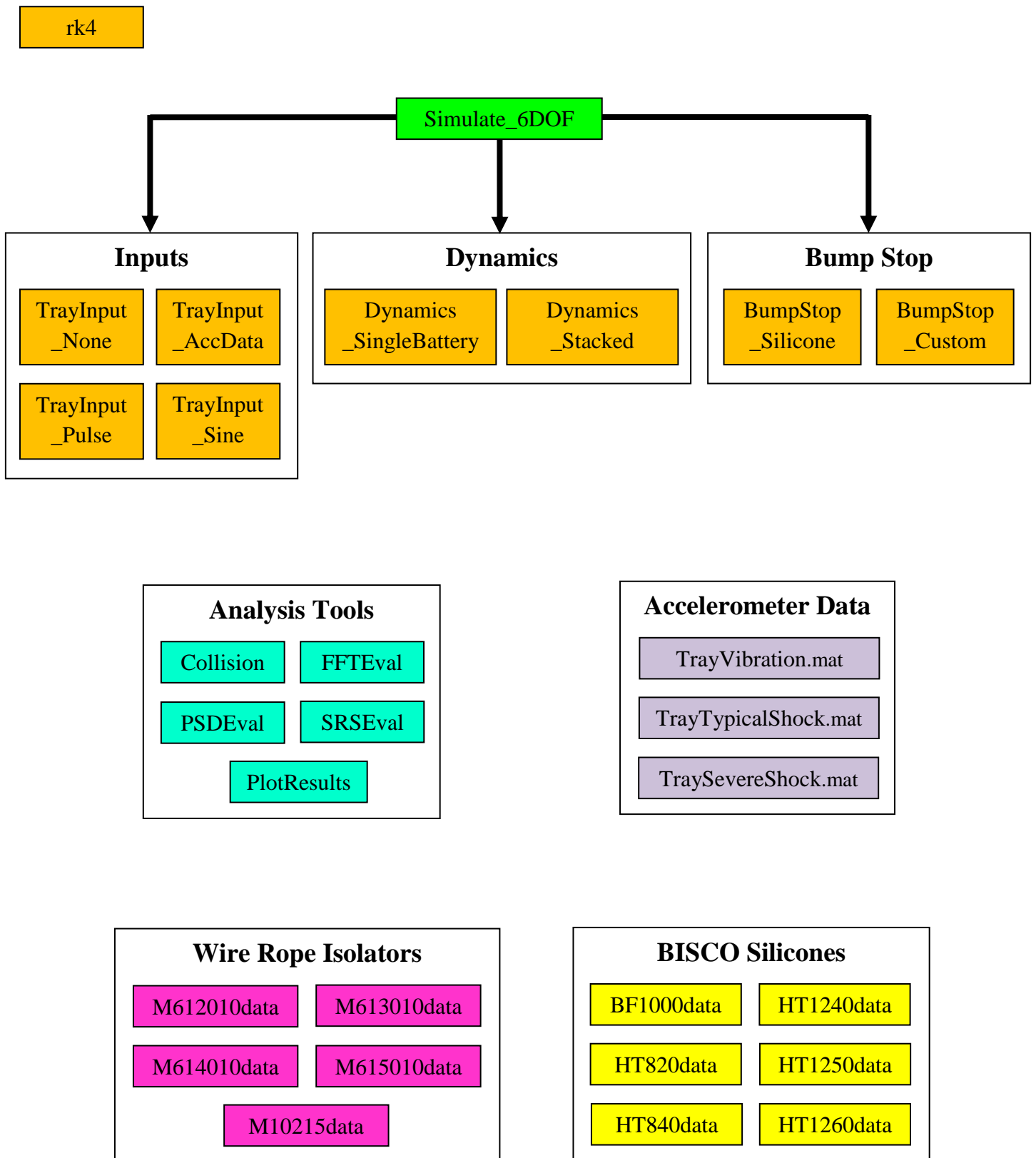


Figure B-1. MATLAB file structure

Table B-1. List of all MATLAB files

	<b>File Name</b>	<b>Type</b>	<b>Function Input</b>	<b>Function Output</b>
1	Simulate_6DOF	script	-	-
2	rk4	function	fdyn, finp, time, dt, xcurr, u0, SimDetails, AccData	xnew
3	TrayInput_AccData	function	t, u0, AccData	u
4	TrayInput_None			
5	TrayInput_Pulse			
6	TrayInput_Sine			
7	Dynamics_SingleBattery	function	t, x, u, SimDetails	xdot, y, SimDetails
8	Dynamics_Stacked			
9	BumpStop_Silicone	function	dispBattery, velBattery, Points, Rzyx, SimDetails	disp_BS, Forces_BS, Moments_BS, SimDetails
10	BumpStop_Custom			
11	Collision	function	Results, Clearances	[]
12	FFTEval		Results	freq, ampInput, ampOutput
13	PSDEval		Results	freq, PowerInput, PowerOutput
14	SRSEval		Results	fn, maximaxInput, maximaxOutput
15	PlotResults		Results, Clearances	[]
16	M612010data	function	()	IsolatorData
17	M613010data			
18	M614010data			
19	M615010data			
20	M1021508data			
21	BF1000data	function	()	BumpStopData
22	HT820data			
23	HT840data			
24	HT1240data			
25	HT1250data			
26	HT1260data			
27	TrayVibration	.mat	-	-
28	TrayTypicalShock			
29	TraySevereShock			

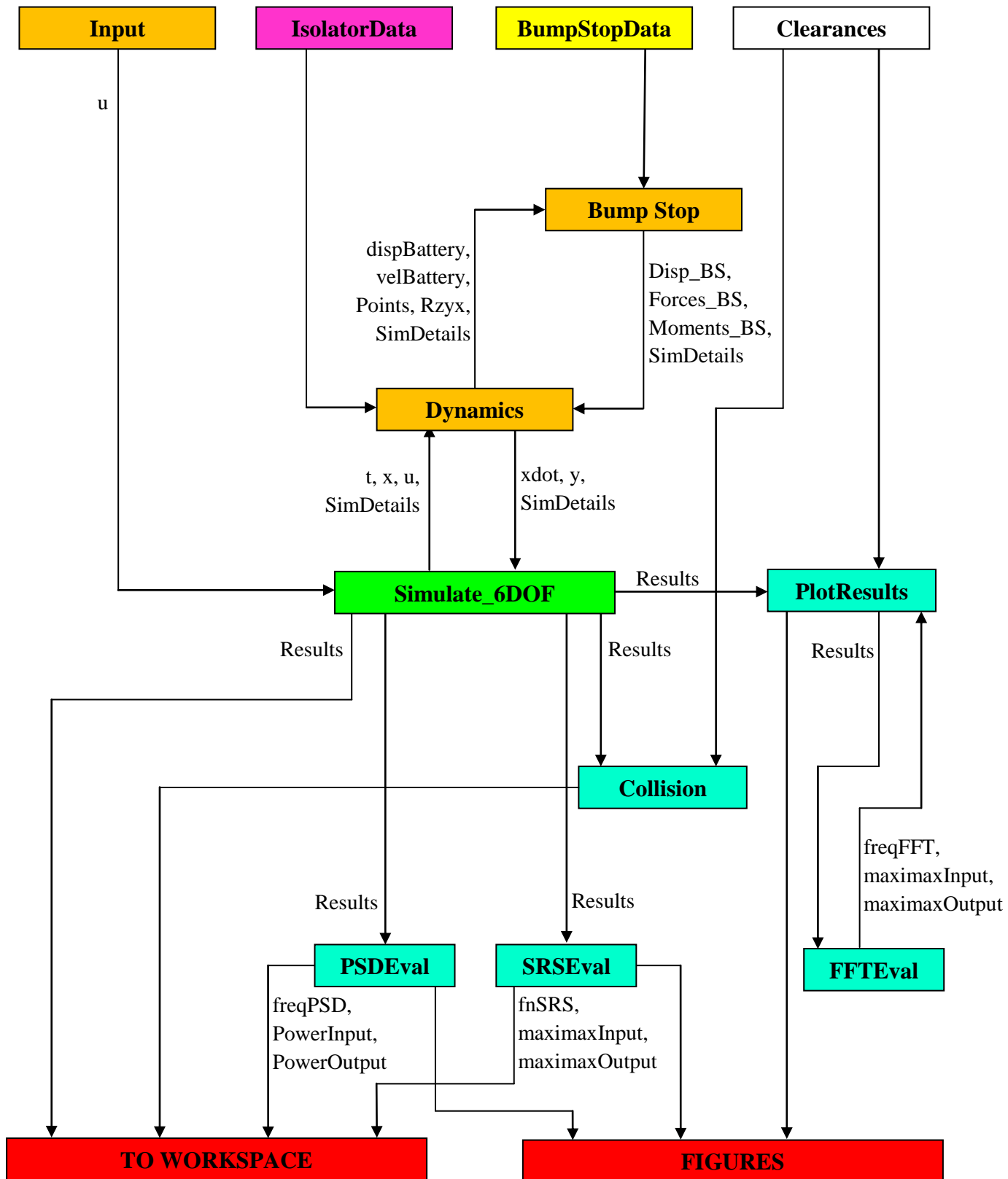


Figure B-2. Flow diagram of MATLAB input/output variables

## APPENDIX C – DESCRIPTIONS OF MATLAB FILES

The following writing convention is used to discuss the MATLAB files. The names of MATLAB script or function files are placed inside quotations, e.g. “Dynamics\_SingleBattery”. Names of variables or structures are italicized, e.g. *SimDetails*. Names of strings are typed in purple text with single quotations, e.g. ‘TrayInput\_SevereShock’.

### C.1 Simulate\_6DOF

“Simulate\_6DOF” is the script file that executes the simulation. It is the home file that directs the usage of all other files. The functionality of “Simulate\_6DOF” is divided into three distinct sections.

The first section is where the Input, Dynamics, and Bump Stop functions are selected. Initial conditions of the input and state variables can also be specified (particularly for analyzing a free response). Lastly, the space clearances between the tray and battery module are specified to be used for collision detecting. See Section D.1 for instructions on how to enter these criteria.

The next section performs a few tasks. Firstly, it creates a structure *SimDetails* that contains time invariant information about the simulation. *SimDetails* passes this information along to use in other functions. It is also a way of saving the details of a simulation all in one place such that the simulation can easily be replicated at a later date. Next, if the system input is accelerometer data, the file allocates which Accelerometer Data .mat file to load. If accelerometer data is not used, a default time step of 0.0005 sec and total simulation time of 3 sec is used (for sine, pulse, and zero inputs). The simulation is then performed by calling the

“rk4” numerical integration function. A waitbar is executed as soon as the simulation begins. It updates every 1% of the simulation time until the simulation is complete at 100%.

Finally, the results of the simulation are stored and plotted. The time-varying variables of the simulation (such as the input vector, states, output vector, displacements of the battery corners, isolator deflection, etc) are stored in a structure *Results*. To plot and analyze the data in *Results*, the analysis tools can be automatically executed. The four Analysis Tools listed are “Collision”, “PlotResults”, “PSDEval”, and “SRSEval”. If these tools are not automatically executed, they can be used at a later date given that the *Results* structure is saved.

## **C.2 rk4**

This function performs the forward time numerical integration for the simulation. It uses a 4<sup>th</sup> order Runge-Kutta algorithm to predict the future states given the present values of the inputs and states.

## **C.3 Tray Inputs**

The input functions describe the translational accelerations of the tray. For all Input functions, the same function inputs are used. The function inputs are time  $t$ , the initial input values  $u0$ , and *AccData*. Depending on which Input function is being used, *AccData* may contain accelerometer data from vehicle testing or be an empty matrix. There are four Input functions that can be selected from “Simulate\_6DOF”.

### **C.3.1 TrayInput\_AccData**

This Input function is used whenever tray accelerometer data is chosen as the system input. The time step of the simulation matches the inverse of the sampling frequency of the data. The function also converts the contents of *AccData* from units of g's to SI units.

### **C.3.2 TrayInput\_None**

“TrayInput\_None” makes all three elements of the input vector  $u$  equal to zero. This function should be used when nonzero initial conditions are specified, as in a free-response simulation.

### **C.3.3 TrayInput\_Pulse**

This Input function creates a halfsine pulse in any or all of the three tray axes. The amplitude (in g's) and pulse width of the halfsine pulse are specified, as well as time that the pulse begins.

### **C.3.4 TrayInput\_Sine**

“TrayInput\_Sine” creates a sine function in any or all of the tray axes. The amplitude (in g's) and frequency of the sine wave are specified. This Input is particularly useful for examining the transmissibility and damping ratio in the system by simply comparing the amplitude of the input to the steady-state amplitude of the response.

## C.4 Dynamics

The Dynamics functions are the most intricate functions in the MATLAB model. They contain the governing equations of motion for the system. These equations calculate the rate of change of the state vector, which fully defines the battery's motion at every instant in time. Two separate Dynamics functions are created. The first function, "Dynamics\_SingleBattery", simulates the single battery assembly configuration, where isolators are installed on the front and back faces. The second dynamic function, "Dynamics\_Stacked", simulates the battery stack configuration. This configuration uses wire rope isolators are on the bottom face of the battery stack. Both functions have identical formats and perform the following tasks...

The beginning of the Dynamics functions selects a wire rope isolator size by allocating its properties from a specified Isolator function. The attachment points of the isolators are selected as well. Next, the current values of the input  $u$  and the state  $x$  are stored. These values update at every time step via the numerical integration in "rk4". The physical parameters of the battery, such as mass, inertia, and dimensions are defined.

Using the battery parameters and the current battery state, the displacement and velocity at every attachment point on all six battery faces is calculated. This information is stored in multiple displacement and velocity matrices, sorted by the corresponding battery face. The forces applied at each isolator attachment point are calculated using the displacement / velocity matrices and the isolator stiffness and damping information. For every attachment point without an isolator, the force is set to zero. Nonlinear effects such as increased damping ratio and the transition from compressive to tensile stiffness are applied as well. Next, the cross product of the attachment point positions and forces is performed to calculate the body-fixed moments about the battery. If a bump stop is used, the displacement and velocity matrices of the battery are sent

to the Bump Stop function where bump stop forces and moments are calculated. These forces and moments are then returned to the Dynamics function to be used in the equations of motion. If no bump stop is used, all bump stop forces and moments are set to zero.

The equations of motion and output battery accelerations are derived using the isolator and bump stop forces and moments. The equations of motion calculate the rate of change of the state vector. This rate of change gets fed into “rk4” and the entire Dynamics function is called again for every instant in time using the updated input and state values.

The displacements of four chosen isolator positions are stored in a matrix *IsoDisp*. This matrix is used to analyze the deflections of pivotal isolators to ensure that they do not exceed the maximum travel capacities. For the battery stack, the four corner isolators exhibit the most significant deflections and are thus the best choices to use in *IsoDisp*. Furthermore, the displacements of the eight corners of the battery are calculated for collision detection purposes. The corners have the most extreme displacements and are the first locations to make contact with the tray.

Finally, any time-varying vector that needs to be passed to other functions, besides *xdot*, needs to be stored in the output vector *y*. This vector contains at minimum the output battery accelerations, isolator displacement, and the corner displacements.

## **C.5 Bump Stops**

The bump stops are secondary suspension materials that are used to prevent the battery’s displacements from becoming too large. The bump stops are responsible for 1) preventing any collision between the battery and the tray, and 2) preventing the wire rope isolators from exceeding their maximum rated deflections. Two Bump Stop functions are provided with this

model. The first, “BumpStop\_Silicone” utilizes the properties of BISCO silicone materials. The second function, “BumpStop\_Custom” incorporates behavior of a fictitious material that can be tuned to desired characteristics. Both functions are explained in more detail below.

### **C.5.1 BumpStop\_Silicone**

This function uses battery displacements and velocities to calculate the corresponding bump stop forces and moments at every attachment point. The bump stop properties can be independently assigned for the following four directions: X, Y, Top, and Bottom. It is assumed that the same bump stop design is used on the front and back battery faces, which are grouped as the X direction design. Similarly, the left and right bump stop designs are grouped together to be the Y design.

The extrinsic properties of the bump stops are described here such as area, engage distances, number of sheets, and attachment locations. The function incorporates these extrinsic properties with the intrinsic polynomial curve fit coefficients from the material’s structure *BumpStopData* to generate forces and moments acting on the battery. The bump stop forces and moments are then sent to the dynamics function to be used in the equations of motion.

### **C.5.2 BumpStop\_Custom**

This function is used to tune the bump stop design without having to associate a bump stop material function. The battery displacements and velocities are taken from the Dynamics function, which can be incorporated into a linear or nonlinear equation to convert these variables

into bump stop forces. For instance, linear bump stop forces can be implemented by multiplying the displacement by a constant stiffness value  $k$  to yield the force. Furthermore, this function allows for a quick way to implement a new material's force-deflection curve without making a separate function file. Any relationship between deflection, velocity, and force can be used.

## **C.6 Analysis Tools**

There are five functions created to analyze and/or plot the results of the simulation. These are “Collision”, “FFTEval”, “PSDEval”, “SRSEval”, and “PlotResults”. These tools help illustrate the effectiveness of the suspension designs and provide visual evidence needed to compare the results of multiple simulations.

### **C.6.1 Collision**

This function uses battery displacements to detect any collision between the battery and tray as well as bottoming-out effects of the wire rope isolators. “Collision” also analyzes the weight of the battery with the vendor model and quantity of wire rope isolators to determine if the isolators' static loads are exceeded.

Any contact between the battery and tray is analyzed by looking at the displacements of the eight battery corners, and comparing with the space clearances specified by the user. The corners are labeled as shown in Figure C-1.

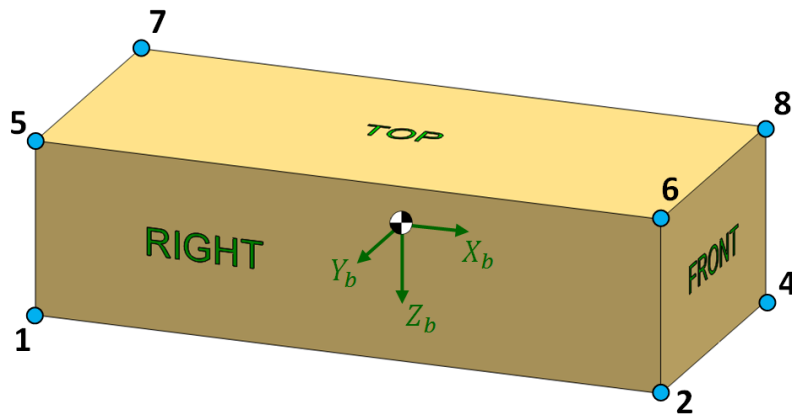


Figure C-1. Battery corner labeling

The results of the collision detection are returned as text to the workspace. An example reading might be...

```

Isolator Deflection Analysis...
Isolator Bottom Out in X Direction (Shear)
Isolator Bottom Out in Z Direction (Compression)

Tray-Collision Analysis...
Collision Detected with Bottom of Tray

Isolator Static Load Analysis...
Rated static load of isolators is not exceeded

```

## C.6.2 FFTEval

This function performs a fast Fourier transform (FFT) on the input and response signals in each of the three directions (X, Y, Z). A 3-element subplot is created for each axis showing the input and response in the time domain, FFT of the input signal, and FFT of the battery response. These plots quickly show the primary frequencies contained in the input and response signals and thus indicate where amplification and attenuation occur.

### **C.6.3 PSDEval**

“PSDEval” performs a power spectral density on the input and response signals in each of the three directions (X, Y, Z). A 3-element subplot is generated showing the PSD vs. frequency of the input and response for each axis. This function is primarily used when analyzing vibration results.

### **C.6.4 SRSEval**

This function performs a shock response spectrum analysis on the input and battery response signals in each of the three directions (X, Y, Z). A 3-element subplot is generated showing the SRS vs. natural frequency of the input and battery response for each axis. This function is primarily used when analyzing shock results.

### **C.6.5 PlotResults**

“PlotResults” generates ten figures showing various results of the simulation. The plots are as follows...

1. Tray Accelerations
2. States
3. Battery Accelerations
4. X Corner Displacements
5. Y Corner Displacements
6. Z Corner Displacements
7. Isolator Deflections
8. FFT – X Direction
9. FFT – Y Direction
10. FFT – Z Direction

## C.7 Wire Rope Isolators

All information pertaining to a particular wire rope isolator is stored in a separate function. This allows for isolator sizes to be easily interchanged by simply selecting a different isolator function. These functions possess the multi-axis spring constants as well as maximum rated deflections for each deflection mode. These characteristics are stored in a structure *IsolatorData* which is fed into the Dynamics functions for simulation. There are five isolator functions included with the dynamic model. They are “M612010data”, “M613010data”, “M614010data”, “M615010data”, and “M1021508data”. These isolators are provided by Isolation Dynamics Corporation (IDC).

## C.8 BISCO Silicones

Six independent functions contain the intrinsic material properties of BISCO silicone foams and solids. Three are silicone foams (“BF1000data”, “HT820data”, “HT840data”), and three are silicone solid rubber pads (“HT1240data”, “HT1250data”, “HT1260data”). The formats for these six functions are all identical. Polynomial curve fitting coefficients are generated using force-deflection data obtained from BISCO. These coefficients, along with the maximum rated deflection of the sheet is stored and output in the structure *BumpStopData*.

## APPENDIX D – USER INSTRUCTIONS

This section lists step-by-step instructions explaining how to properly use the MATLAB model. The majority of the MATLAB code never needs to be altered by the user; thus, it is helpful to show exactly what parameters may need to be changed and where they are located throughout the code.

### D.1 Prepare “Simulate\_6DOF”

#### **Step 1** – Specify Input, Dynamics, and Bump Stop Functions

There are many simulation options that need to be selected in the “Simulate\_6DOF” script file. Firstly, the function files used for the simulation input, dynamics, and bump stop need to be specified. This is done by assigning strings of the file names to the variables `fin`, `fdyn`, and `fbs`, respectively.

The simplest way to select these functions is list all possible function names and change all of the unused function names to comments. This is done by placing a “%” sign at the beginning of the code line (the entire line turns to green text). The only line of code that is not green should be the desired function name that will be used for the simulation. As seen in Figure D-1, the Input function selected is ‘TrayInput\_SevereShock’, the Dynamics function is ‘Dynamics\_SingleBattery’, and the Bump Stop file is ‘BumpStop\_Silicone’.

```

22
23     %%%%%%%%%%%%%%%%%%%%%%%%%%%%%%%%%%%%%%%%%%%%%%%%%%%%%%%%%%%%%%%%%%%%%%%%% Beginning of user input section %%%%%%%%%%%%%%%%%%%%%%%%%%%%%%%%%%%%%%%%%%%%%%%%%%%%%%%%%%%%%%%%%%%%%%%%%
24
25
26     % Select which Input Function to use
27     % finp = 'TrayInput_None';
28     % finp = 'TrayInput_Vibration';
29 -   finp = 'TrayInput_TypicalShock';
30     % finp = 'TrayInput_SevereShock';
31     % finp = 'TrayInput_Sine';
32     % finp = 'TrayInput_Pulse';
33
34
35     % Select which Dynamics Function to use
36 -   fdyn = 'Dynamics_SingleBattery';
37     % fdyn = 'Dynamics_Stacked';
38
39
40     % Select which Bump Stop Function to use
41     % fbs = 'None';
42 -   fbs = 'BumpStop_Silicone';
43     % fbs = 'BumpStop_Custom';
44

```

Figure D-1. Select Input, Dynamics, and Bump Stop functions

## **Step 2 – Specify Initial Conditions**

The initial conditions of the system’s inputs and states are listed in two column vectors,  $u0$  and  $x0$ , as shown in Figure D-2. For most simulations, these vectors can contain all zero elements. It is unnecessary to use nonzero initial conditions when utilizing accelerometer data because the transient data occurs after  $t=0$ . The only situation when nonzero initial conditions should be utilized is for simulating the free response of the system. To do this, the Input function selected from **Step 1** is `finp = ‘TrayInput_None’`,  $u0$  is a zero column vector, and  $x0$  should contain one or more nonzero elements. This simulates the battery having an initial displacement or velocity relative to its equilibrium state.

### Step 3 – Specify Clearances

The clearances represent the linear distances between the outer surfaces of the battery and the inner walls of the tray. It is assumed that the battery is installed symmetrically inside the tray with respect to the longitudinal and lateral directions, i.e. the clearances in front and behind the battery are equal and the clearances to the left and right of the battery are equal. The clearances in the vertical direction, however, are not assumed to be symmetric. This implementation is motivated by the fact that wire rope isolators have different travel capabilities in tension as compared to compression.

The clearance information is stored in a structure called *Clearances*. This structure has four fields, labeled X, Y, Top, and Bottom. Simply enter clearance dimensions (in units of inches) for these four fields, as illustrated in Figure D-2. The *Clearances* structure gets passed on to other functions such as “Collision” to detect if the battery and tray collide.

```
45
46   % Set initial conditions
47 -   u0 = [0;0;0];           % initial values of inputs [m/s^2]
48
49 -   x0 = [0;0;0;0;0;0;0;0;0;0;0;0]; % initial values of states
50   % units [m;m;m;rad;rad;rad;m/s;m/s;m/s;rad/s;rad/s;rad/s]
51
52   % Define clearances between battery and tray [in]
53 -   Clearances.X          = 3.25;
54 -   Clearances.Y          = 0.75;
55 -   Clearances.Top        = 0.75;
56 -   Clearances.Bottom     = 0.75;
57
58
59   %%%%%%%%%%%%%%%%%%%%%%%%%%%%%%%%%%%%%%%%%%%%%%%%%%%%%%%%%%%%%%%%%%%%%%%%% End of user input section %%%%%%%%%%%%%%%%%%%%%%%%%%%%%%%%%%%%%%%%%%%%%%%%%%%%%%%%%%%%%%%%%%%%%%%%%
60
```

Figure D-2. Specify initial conditions and clearances

#### **Step 4** – Specify Plotting

The last portion of code in “Simulate\_6DOF” contains the list of Analysis Tools functions that plot and analyze the simulation results. The function “Collision” displays text in the workspace according to Section C.6.1. “PlotResults” plots ten different figures showing the simulation results in both the time and frequency domains. Two analysis functions, “PSDEval” and “SRSEval”, are included to plot the acceleration results in the frequency domain.

These four analysis functions can be turned on and off by simply adding or removing a % sign in front of the line of code with the function of interest (similar to the method in **Step 1**). Any function that is not a comment automatically executes when “Simulate\_6DOF” is run. For example, the situation in Figure D-3 executes “Collision”, “PlotResults”, and “SRSEval”, but does not execute “PSDEval”.

```
161
162     % Analyze results and plot
163 -    Collision(Results,Clearances);
164 -    PlotResults(Results,Clearances);
165
166     % Plot Power Spectral Density (for vibration inputs)
167     % [freqPSD, PowerInput, PowerOutput] = PSDEval(Results);
168
169     % Plot Shock Response Spectrum (for shock inputs)
170     [fnSRS, maxInput, maxOutput] = SRSEval(Results);
171
```

Figure D-3. Specify which analysis tools are automatically executed after simulation

## D.2 Prepare the Dynamics File

### **Step 5** – Select Isolator and Attachment Location

In the dynamics file, the two most important characteristics regarding the wire rope isolators are their vendor model and their attachment position with respect to the battery. The vendor model is specified in the structure *IsoData*. *IsoData* contains all pertinent isolator information provided by the vendor, such as stiffness values and allowable deflection. Simply assign the isolator function file to *IsoData*.

Next, the geometric location of the wire rope isolators needs to be specified in terms of attachment points on the battery surfaces (see Section 4.4). As an example, Figure D-4 utilizes four total M10-215-08 wire rope isolators attached at locations ‘3’ and ‘13’ on the front and back battery faces.

```
10
11      % Select the wire rope isolator size
12 -   IsoData = M1021508data();
13
14      % Select attachment locations on front and back faces of battery
15 -   ISO_Attach = [3 13];           % 4 total isolators
16
```

Figure D-4. Isolator selection and attachment location

### **Step 6** – Specify Battery Parameters

The parameters of the battery module such as its mass and dimensions are defined in the Dynamics file. Before running a simulation, ensure that these values are accurate with the updated battery design. If the battery stack is being simulated, the mass and dimensions represent the entire rigid body, not an individual battery module.

```

63
64     % Battery Parameters-----
65 -   m = 412;           % battery mass           [kg]
66 -   g = 9.81;        % gravity constant      [m/s^2]
67
68     % Module Stack Dimensions
69 -   Lx = 1.162;       % length of battery    [m]
70 -   Ly = 0.4978;     % width of battery     [m]
71 -   Lz = 0.313;     % height of battery    [m]
72

```

Figure D-5. Battery mass and dimensions

### **Step 7 – Specify which Isolator Displacements to Output**

An important concern in the dynamic model is ensuring that the maximum rated deflections of the wire rope isolators are not exceeded. Since the lengths of the wires are fixed in the real isolators, having simulated deflections that exceed the rated isolator travel is not physically feasible. It is essential to make sure the isolators are operating within their allowable ranges at all times.

To do this, specify which of the isolators from **Step 1** to analyze for deflection ranges. The deflections of these isolators are elements that can be extracted from the battery surface displacement matrices. The columns of the displacement matrices correspond to attachment points and the rows correspond to the  $X_t$ ,  $Y_t$ , and  $Z_t$  directions. For example, if the isolator of choice is installed to attachment point ‘5’ on the bottom battery stack face, then extract the fifteen column in the displacement matrices for the bottom face:  $disp\_Bottom(1,5)$ ,  $disp\_Bottom(2,5)$ , and  $disp\_Bottom(3,5)$ . When variables are assigned to all of the isolator deflections of interest, combine these variables in a vector  $DispIso$ . This variable is placed in the  $y$  output vector at the end of the Dynamics file.

An example of this process is shown below. Four isolators are chosen, attachment points ‘1’, ‘5’, ‘26’, ‘30’ on the bottom face. The displacements at those locations are extracted from the battery surface displacement matrices and are assigned four variables. Note that the static displacement *StaticDisp* needs to be added in the Z direction because the isolator is deformed in the static equilibrium state. Finally, these variables are grouped into *DispIso*.

```

439
440 % Specify which isolator deflections are desired for plotting-----
441 % All displacements in [m]
442
443 - disp1 = zeros(1,3);
444 - disp1(1) = disp_Bottom(1,1);
445 - disp1(2) = disp_Bottom(2,1);
446 - disp1(3) = disp_Bottom(3,1) + StaticDisp;
447
448 - disp5 = zeros(1,3);
449 - disp5(1) = disp_Bottom(1,5);
450 - disp5(2) = disp_Bottom(2,5);
451 - disp5(3) = disp_Bottom(3,5) + StaticDisp;
452
453 - disp26 = zeros(1,3);
454 - disp26(1) = disp_Bottom(1,26);
455 - disp26(2) = disp_Bottom(2,26);
456 - disp26(3) = disp_Bottom(3,26) + StaticDisp;
457
458 - disp30 = zeros(1,3);
459 - disp30(1) = disp_Bottom(1,30);
460 - disp30(2) = disp_Bottom(2,30);
461 - disp30(3) = disp_Bottom(3,30) + StaticDisp;
462
463 % Collect isolator displacements in DispIso
464 - DispISO = [disp1 disp5 disp26 disp30];
465

```

Figure D-6. Isolator deflections assigned to *DispIso*, which is used in “PlotResults”

### D.3 Prepare the Bump Stop File

If a Bump Stop file is used, many bump stop parameters need to be defined in those functions. The steps to prepare the bump stops are different for the two included Bump Stop functions. If “BumpStop\_Silicone” is selected, proceed to Section D.3.1. If “BumpStop\_Custom” is selected, follow the steps listed in Section D.3.2.

### D.3.1 Prepare “BumpStop\_Silicone”

#### **Step 8a** – Select Silicone Materials and Attachment Points

Similar to **Step 5** for the wire rope isolator selection, the silicone bump stops needs to be assigned materials and attachment positions. The bump stops can be applied to all six faces of the battery, and a different silicone design can be applied to the Top, Bottom, X, and Y faces. Again, symmetry is assumed for the Front/Back faces and Left/Right faces.

```
38 % Select bump stop material for the longitudinal, lateral, top and bottom
39 % battery faces
40 - BumpStopX      = HT1240data();
41 - BumpStopY      = HT1240data();
42 - BumpStopBottom = HT1240data();
43 - BumpStopTop    = HT1240data();
44
45 % Select locations to attach the bump stop material
46 AttachX         = [1 5 11 15]; % same location on front and back faces
47 - AttachY       = [1 5 26 30]; % same location on left and right faces
48 - AttachBottom  = [1 5 26 30];
49 - AttachTop     = [1 5 26 30];
50
```

Figure D-7. Silicone bump stop material and attachment positions

#### **Step 9a** – Specify Attachment Point Areas

When using silicone as the bump stop material, the force that the silicone provides is directly proportional to the area at which the silicone is acting. The area can be specified independently for the X, Y, Bottom, and Top faces of the battery. This area corresponds to the area at each attachment point, NOT the total area acting on a particular face. Therefore, there are physical limits as to how large the area at each attachment point can be.

The largest area that can be applied to an attachment point is the total area of that battery surface divided by the total number of possible attachment points on that face. These maximum areas are shown as comments on lines 105-108 in Figure D-8. The area can, however, be less than this maximum allowable area. For example, 12 in<sup>2</sup> is applied for each of the specified attachment points in Figure D-8.

```

97
98      % Area of silicone acting at each attachment point [m^2]-----
99 -    Lx = SimDetails.BatteryParameters.Dimensions.Lx;      % [m]
100 -    Ly = SimDetails.BatteryParameters.Dimensions.Ly;      % [m]
101 -    Lz = SimDetails.BatteryParameters.Dimensions.Lz;      % [m]
102
103 -    in2m = 0.0254; % convert inches to meters
104
105 -    areaX      = 12*in2m*in2m;      % max Ly*Lz/15;
106 -    areaY      = 12*in2m*in2m;      % max Lx*Lz/30;
107 -    areaBottom = 12*in2m*in2m;      % max Lx*Ly/30;
108 -    areaTop    = 12*in2m*in2m;      % max Lx*Ly/30;
109

```

Figure D-8. Bump stop individual attachment areas

**Step 10a – Specify Numbers of Silicone Sheets**

The thickness of an individual silicone sheet is constrained by the vendor. If a thicker bump stop is desired, multiple silicone sheets can be stacked in series. This increases the effective bump stop thickness, while reducing the effective bump stop stiffness. Specify the number of sheets to stack for each of the four directions.

```

110
111      % Select number of silicone sheets to stack in series-----
112      % (same area used for each sheet)
113 -    nsheetsX      = 4;
114 -    nsheetsY      = 1;
115 -    nsheetsBottom = 2;
116 -    nsheetsTop    = 2;
117

```

Figure D-9. Number of silicone sheets stacked in series

### **Step 11a** – Specify Engage Distances

Not only do the bump stops' areas and number of sheets need to be specified, but the displacements at which the battery surfaces initially engage the bump stops are additional tunable parameters. These displacements are specified as percentages of the maximum rated isolator travel. For example, if the isolator travel in the X direction is 0.80” and there is 0.6” of space between the battery and bump stop at equilibrium, then the battery engages the bump stop at 75% of isolator maximum travel, or  $engageX = 0.75$ .

The engage distances for each of the four directions need to be specified, as shown in Figure D-10.

```
117
118   % Percentage of isolator displacement when bump stop engages battery
119   % Example: engageX = 0.75 means that the battery will contact the bump stop
120   % when its displacement is equal to 75% of the isolators' available travel
121   % in the X direction
122 -   engageX           = 0.75;
123 -   engageY           = 0.75;
124 -   engageBottom     = 0.50;
125 -   engageTop        = 0.50;
126
```

Figure D-10. Engage distances

### **D.3.2 Prepare “BumpStop\_Custom”**

#### **Step 8b** – Select Attachment Points

The effects of a bump stop can be applied to all six faces of the battery module, and the bump stop properties are independent in the Top, Bottom, X, and Y faces. Again, symmetry is assumed for the Front/Back faces and Left/Right faces. Assign the bump stop to the attachment points on any or all of the six battery faces, as detailed in [Step 8a](#).

## **Step 9b** – Select Engage Distances

Refer to [Step 11a](#).

## **Step 10b** – Implement Force-Deflection Relationship

Unlike “BumpStop\_Silicone”, no external functions are called from this Bump Stop function. All of the bump stop characteristics are entered internally. Bump stop area and thickness do not influence the bump stop characteristics. In fact, the custom bump stop does not need to be a foam material at all. Instead, the relationship between battery displacement/velocity and force is independently defined. This can be a linear, quadratic, or other polynomial relationship that calculates forces given displacement and velocity information of the battery.

As an example, a linear relationship is specified below in Figure D-11. The damping ratio and linear stiffness in each of the four directions is entered by the user.

```
93
94     % Damping ratios
95 -   zX      = 0.05;
96 -   zY      = 0.05;
97 -   zBottom = 0.05;
98 -   zTop    = 0.05;
99
100    % Tunable linear stiffness values [N/m]
101 -   ktuneX    = 10^7;
102 -   ktuneY    = 0;
103 -   ktuneBottom = 10^6;
104 -   ktuneTop  = 10^4;
105
106    % Linear viscous damping coefficients [N-s/m]
107 -   cX      = 2*zX      *sqrt(m/numel(AttachX)) *ktuneX;
108 -   cY      = 2*zY      *sqrt(m/numel(AttachY)) *ktuneY;
109 -   cBottom = 2*zBottom *sqrt(m/numel(AttachBottom))*ktuneBottom;
110 -   cTop    = 2*zTop    *sqrt(m/numel(AttachTop)) *ktuneTop;
111
```

Figure D-11. Custom stiffness and damping properties

Next, the damping and stiffness are incorporated into a relationship between displacement/velocity and force. The custom bump stop force and moment equations for the top face of the battery are listed in Figure D-12.

The code works as follows: First, a for loop marches through every attachment point where the bump stop exists. Next, it is determined if the bump stop is engaged using the battery's current displacement. If the bump stop is engaged, the bump stop compression is calculated. The bump stop force is calculated in tray coordinates using the bump stop compression and velocity values at that instant in time. Lastly, the body-fixed moment is determined using the cross product between position and force and the inverse of the coordinate transformation matrix. This algorithm repeats for each of the battery faces.

```
128
129 % Top Side-----
130 - for i = AttachTop
131 -   if disp_TopZ(i) < -IsoMaxDispTension*engageTop
132 -     disp_Top(i) = - disp_TopZ(i) - IsoMaxDispTension*engageTop;
133 -     FTop(i) = ktuneTop*disp_Top(i) - cTop*vel_TopZ(i);
134
135 -     FTopb = Rzyx'*[0;0;FTop(i)];
136 -     tauTop(1,i) = Points_Top(2,i)*FTopb(3) - Points_Top(3,i)*FTopb(2);
137 -     tauTop(2,i) = Points_Top(3,i)*FTopb(1) - Points_Top(1,i)*FTopb(3);
138 -     tauTop(3,i) = Points_Top(1,i)*FTopb(2) - Points_Top(2,i)*FTopb(1);
139 -   end
140 - end
141
```

Figure D-12. Custom bump stop force and moment calculation

The final information that the user needs to specify is what variables to save in *SimDetails*. Any information needed to recreate this bump stop design should be specified in *SimDetails* found at the end of the file. Variables to save might be the linear stiffness values and damping ratios, for example.

## Step 11 – None

### D.4 Run, Analyze, Save

#### Step 12 – Run Simulation

Once all the steps in Sections D.1-D.3 are completed, the simulation is ready to be run.

Click the Run button in the “Simulate\_6DOF” script.

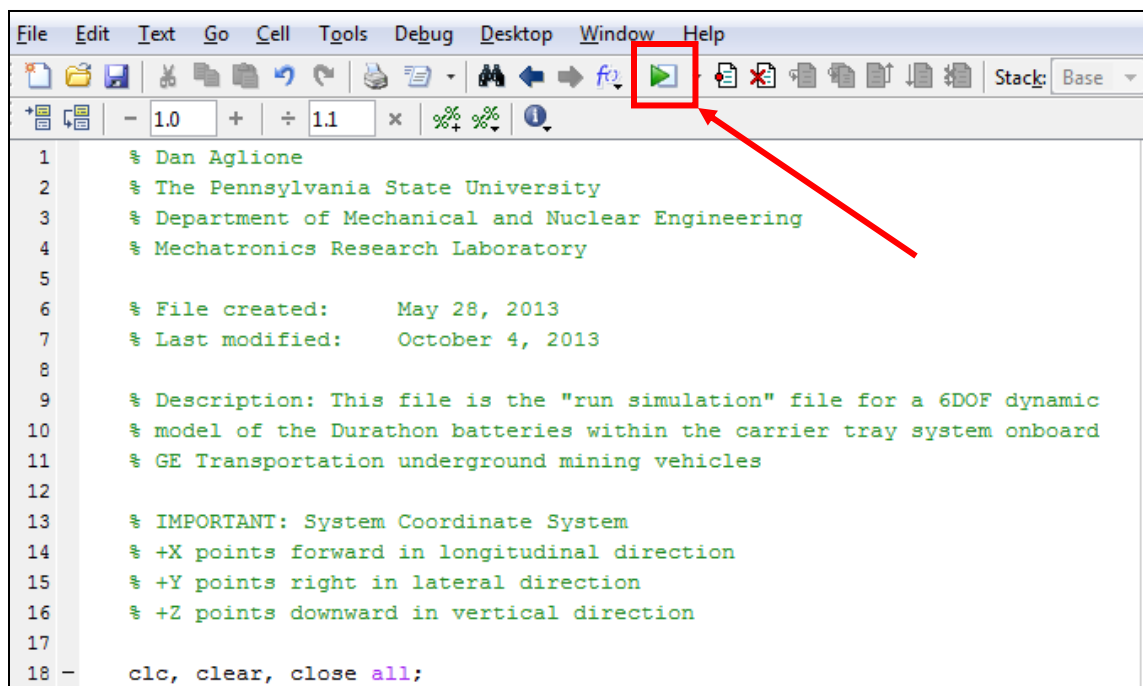


Figure D-13. Execute "Simulate\_6DOF"

A waitbar shows the progress of the simulation. This updates every 1% of the total simulation time.

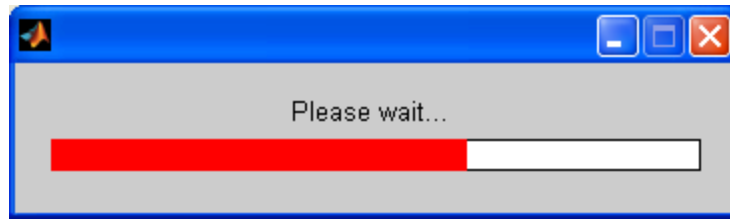


Figure D-14. Waitbar

### **Step 13** – Analyze/Save Results

Once the simulation is completed, the analysis tools selected in **Step 4** are automatically executed. If selected, “Collision” returns text to the workspace listing any interference detection. Plots open showing time and/or frequency domain results.

In addition, all of the pertinent simulation information needed to recreate these results are stored in the structure *Results*. This structure contains the time-invariant structure *SimDetails* as well as the default contents of the y output vector located the bottom of the Dynamics function.

Field	Value	Min	Max
SimDetails	<1x1 struct>		
time	<8000x1 double>	0	3.9995
dt	5.0000e-04	5.000...	5.000...
InputAccel	<8000x3 double>	-31.6...	24.2854
States	<8000x12 double>	-0.7715	0.5681
OutputAccel	<8000x3 double>	-4.9993	9.9719
CornerDeflect	<1x1 struct>		
IsoDeflect	<8000x12 double>	-0.0107	0.0152

Figure D-15. Contents of the structure *Results*

The contents of *SimDetails* are shown in Figure D-16. They include the names of the Input, Dynamics, and Bump Stop functions specified in **Step 1**, as well as the battery parameters specified in **Step 5**. Furthermore, the details of the isolator and bump stop as determined in Sections D.2 and D.3 are included in the structures *IsolatorInfo* and *BumpStopInfo*. *StaticDisp\_inch* is the static deflection of each isolator at the static equilibrium position.

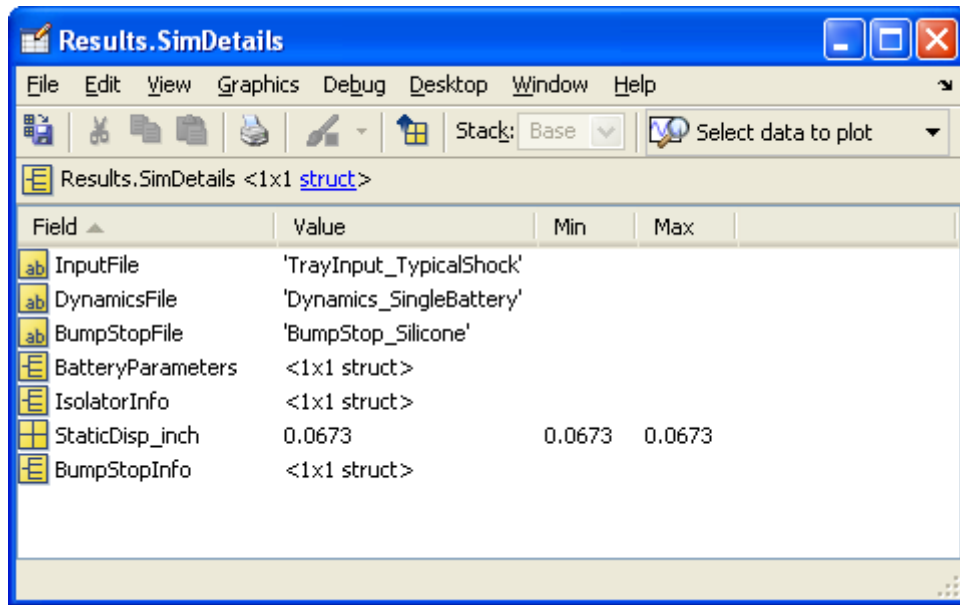


Figure D-16. Contents of *SimDetails*

*IsolatorInfo* contains the wire rope information specified in **Step 5**.

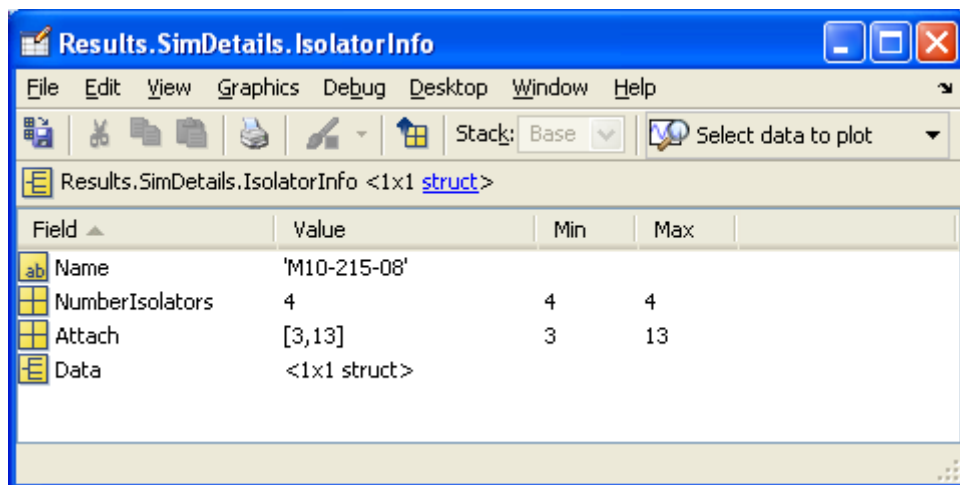


Figure D-17. Contents of *IsolatorInfo*

*BumpStopInfo* contains the bump stop information specified in Section D.3. This information is divided into fields corresponding to each of the bump stop directions. The contents of this structure depend whether “BumpStop\_Silicone” or “BumpStop\_Custom” is used.

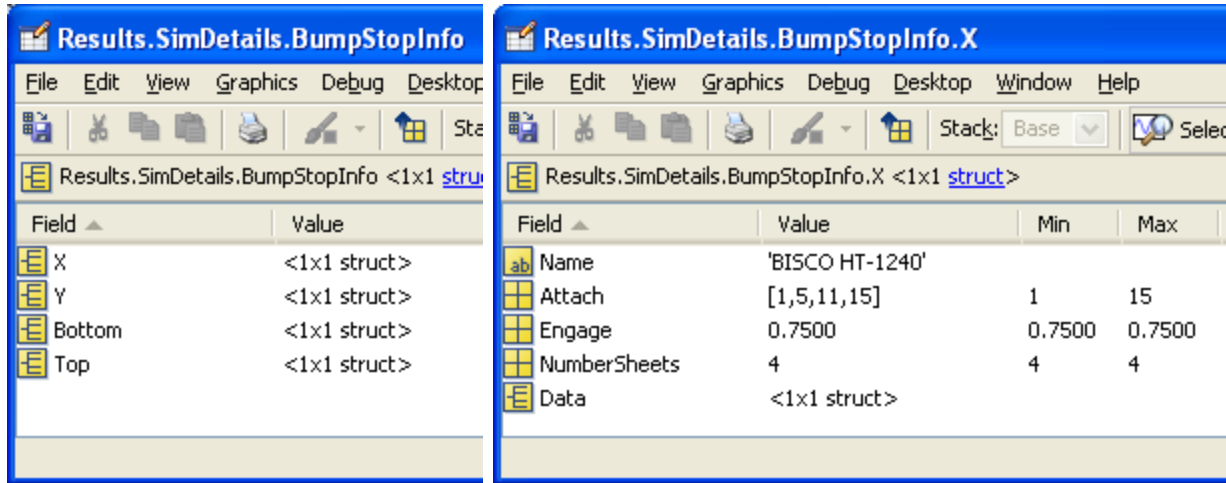


Figure D-18. Contents of *BumpStopInfo*

If the user wants to save the results of the simulation, only the structure *Results* needs to be saved. All of the Analysis Tools can be re-run using *Results* and the structure *Clearances* which can be redefined at any time. To do this, use the following command.

```
save('matFileName', 'Results')
```

This saves *Results* in a .mat file to the current directory.